

X-RAY SCATTER TOMOGRAPHY USING CODED APERTURES

Kenneth P. MacCabe

A dissertation submitted to the faculty at the University of North Carolina at Chapel Hill
in partial fulfillment of the requirements for the degree of Doctor of Philosophy in the
Department of Physics and Astronomy.

Chapel Hill
2014

Approved by:

David Brady

Fabian Heitsch

Amy Oldenburg

Martin Tornai

Otto Zhou

© 2014
Kenneth P. MacCabe
ALL RIGHTS RESERVED

ABSTRACT

Kenneth P. MacCabe: X-ray scatter tomography using coded apertures
(Under the direction of David Brady and Otto Zhou)

This work proposes and studies a new field of x-ray tomography which combines the principles of scatter imaging and coded apertures, termed “coded aperture x-ray scatter imaging” (CAXSI). Conventional x-ray tomography reconstructs an object’s electron density distribution by measuring a set of line integrals known as the x-ray transform, based physically on the attenuation of incident rays. More recently, scatter imaging has emerged as an alternative to attenuation imaging by measuring radiation from coherent and incoherent scattering. The information-rich scatter signal may be used to infer density as well as molecular structure throughout a volume. Some scatter modalities use collimators at the source and detector, resulting in long scan times due to the low efficiency of scattering mechanisms combined with a high degree of spatial filtering. CAXSI comes to the rescue by employing coded apertures. Coded apertures transmit a larger fraction of the scattered rays than collimators while also imposing structure to the scatter signal. In a coded aperture system each detector is sensitive to multiple ray paths, producing multiplexed measurements. The coding problem is then to design an aperture which enables de-multiplexing to reconstruct the desired physical properties and spatial distribution of the target.

In this work, a number of CAXSI systems are proposed, analyzed, and demonstrated. One-dimensional “pencil” beams, two-dimensional “fan” beams, and three-dimensional “cone” beams are considered for the illumination. Pencil beam and fan beam CAXSI systems are demonstrated experimentally. The utility of energy-integrating (scintillation) detectors and energy-sensitive (photon counting) detectors are evaluated theoretically, and new coded aperture designs are presented for each beam geometry. Physical models are developed for each coded aperture system, from which resolution metrics are derived. Systems employing different combinations of beam geometry, coded apertures, and detectors are analyzed by constructing linear measurement operators and comparing their singular value decompositions. Since x-ray measurements are typically dominated by photon “shot” noise, iterative algorithms based on Poisson statistics are used to perform the reconstructions.

This dissertation includes previously published and unpublished co-authored material.

This piece is dedicated to my lovely wife Kat,
who has believed in me from day one.

ACKNOWLEDGEMENTS

The author would like to thank the dissertation committee members for their generous patience and guidance. The previously published results were made possible by the hard work of a number of co-authors, specifically:

Chapter 2: D. J. Brady, D. L. Marks, and J. A. O'Sullivan

Chapter 3: D. J. Brady, D. L. Marks, E. Samei, K. Krishnamurthy, and A. Chawla

Chapter 4: D. J. Brady, D. L. Marks, M. P. Tornai, and A. D. Holmgren

I would also like to thank my friends and colleagues in the Duke Imaging and Spectroscopy Program and elsewhere who have offered their thoughts and experience, my parents Steve and Beth for raising me right and always encouraging me, my talented brothers Greg, Lee, and Ted who always treat me like a hero, and my loving wife Kat for her unwavering support in more ways than I ever thought possible. Also, I owe a great debt to our cats Bear and Foxy for humoring me during countless hours of practice presentations.

This work was supported by the Department of Homeland Security, Science and Technology Directorate through contract HSHQDC-11-C-00083. Co-author M. P. Tornai is also partly supported by NIH R01 CA96821 from which the basis x-ray system of Chapter 4 was developed.

TABLE OF CONTENTS

LIST OF TABLES	ix
LIST OF FIGURES	x
LIST OF ABBREVIATIONS	xii
CHAPTER 1: INTRODUCTION	1
1.1 Background	1
1.2 Scatter imaging principles	8
1.2.1 Scattering from a point	9
1.2.2 Forward models for volume imaging	16
1.3 Coded apertures	17
1.4 Discretization of the forward model	20
1.5 Reconstruction algorithms	21
1.6 Singular value analysis	23
CHAPTER 2: CODED APERTURES FOR X-RAY SCATTER IMAGING	26
2.1 Background	26
2.2 Pencil beam CAXSI	28
2.3 Anisotropic scattering	30
2.4 Fan beam CAXSI	34
2.5 Scalability of imaging techniques	39
2.6 Summary	40
CHAPTER 3: PENCIL BEAM CAXSI	42
3.1 Background	42
3.2 Forward model	44
3.3 Experimental methods	47

3.4	Reconstruction algorithm	52
3.5	Results and discussion	55
CHAPTER 4: FAN BEAM CAXSI		62
4.1	Background	62
4.2	Theory	65
4.2.1	Forward model	65
4.2.2	Reconstruction algorithm	68
4.2.3	System design and resolution	69
4.3	Experimental methods	69
4.3.1	Configuration	69
4.3.2	Acquisition	70
4.3.3	Aperture fabrication	70
4.3.4	Model calibration	71
4.3.5	Test objects	71
4.4	Results	72
4.5	Summary	77
CHAPTER 5: CODED APERTURES FOR VOLUME IMAGING		79
5.1	Background	79
5.2	Forward model	81
5.3	Frequency scale codes (FSC)	84
5.4	Scanning techniques	87
5.5	Compressive sampling	88
CHAPTER 6: ENERGY SENSITIVE CAXSI		90
6.1	Background	90
6.2	Resolution analysis	92
6.3	Simulations	94
6.4	SVD analysis	97

6.5 Reconstructions	103
CHAPTER 7: SUMMARY AND OUTLOOK	108
APPENDICES	112
A. Energy transformation of the coherent scatter differential cross section	112
B. Singular value decomposition for fan beam CAXSI	114
C. Determination of source position	120
REFERENCES	123

LIST OF TABLES

2.1	Scaling of singular values for CAXSI, Radon imaging, and SVT	40
3.1	Table outlining the three sample configurations for this experiment	50

LIST OF FIGURES

1.1	Basic elements of an x-ray tomography system	2
1.2	Pencil and fan beam collimation	4
1.3	Schematics of incoherent and coherent x-ray scattering mechanisms	9
1.4	A simple x-ray scattering experiment	10
1.5	Graphical definition of the momentum transfer $\mathbf{q} = \mathbf{p}_f - \mathbf{p}_i$	12
2.1	System geometry for planar scatter imaging	27
2.2	Coded aperture based on the identity matrix	32
2.3	Coded aperture based on the discrete cosine transform (DCT)	32
2.4	Coded aperture based on a Hadamard matrix	33
2.5	Coded aperture based on a random binary matrix	33
2.6	Singular value spectra of the pencil beam system for each code choice	34
2.7	Coded apertures based on a sinusoid in x and a quadratic residue code in y	36
2.8	Singular value spectra for each of the coded apertures in Fig. 2.7.	37
2.9	Random grayscale coded aperture	38
2.10	Singular value spectra for the proposed code and a random code.	38
3.1	Schematic of a pencil beam coded aperture x-ray scattering experiment	43
3.2	The XSPECT model for the illuminating x-ray spectrum	48
3.3	X-ray image of the coded aperture	49
3.4	Diffraction images for powder samples	52
3.5	Reconstructed scattering density for configuration (A)	55
3.6	Reconstructed scattering density for configuration (B)	56
3.7	Reconstructed scattering density for configuration (C)	56
3.8	Reconstruction results for individual samples	58
3.9	Reconstruction results for a combination of samples	59
3.10	Comparison of modeled and experimental scatter measurements	60
4.1	Diagram of the fan beam experimental system	63

4.2	Coordinate system for a fan beam scattering experiment	65
4.3	Photos of the test objects	72
4.4	Scatter measurements for the plastic DUKE letters	73
4.5	Reconstruction results for the plastic DUKE letters	74
4.6	Reconstruction results for the clock	76
5.1	Relationship between the object, aperture, and measured spatial frequencies.	83
5.2	Coded aperture for volume tomography based on a ring structure in frequency	85
5.3	Measurable surfaces in the object space using a FSC	86
5.4	Coded aperture for volume tomography based on a spiral structure in frequency	87
6.1	Pencil beam system geometry considered for energy sensitive CAXSI.	91
6.2	PSFs for energy sensitive measurements with and without a coded aperture .	93
6.3	Model for the incident x-ray spectrum	95
6.4	Example impulse response for energy sensitive measurements.	96
6.5	PSFs for flat energy spectrum compared with a tungsten spectrum.	97
6.6	Singular values for varying energy resolutions with/without a coded aperture	98
6.7	Singular vectors for $\Delta E = 128$ keV without a coded aperture.	99
6.8	Singular vectors for $\Delta E = 128$ keV without a periodic coded aperture.	100
6.9	Singular vectors for $\Delta E = 8$ keV without a coded aperture.	101
6.10	Singular vectors for $\Delta E = 8$ keV with a periodic coded aperture.	102
6.11	Singular vectors for $\Delta E = 8$ keV with a random binary coded aperture.	103
6.12	The 2D object used to simulate data for the reconstructions	104
6.13	Simulated noiseless measurements for the random grayscale coded aperture. .	105
6.14	Reconstructed images from the simulated measurements	106
6.15	RMSE values for each reconstruction	107

LIST OF ABBREVIATIONS

m, s, eV, c	Unit notation for meters, seconds, electron volts, speed of light in vacuum
CAXSI	Coded aperture x-ray scatter imaging
CSCT	Coherent scatter computed tomography
CT	Computed tomography
DCT	Discrete cosine transform
DE	Dual-energy
DFT	Discrete Fourier transform
FSC	Frequency scale code
FZP	Fresnel zone plate
ME	Multi-energy
MLE	Maximum Likelihood Estimation
(M)URA	(Modified) uniformly redundant array
SNR	Signal-to-noise ratio
SVD	Singular value decomposition
SVT	Selected volume tomography

CHAPTER 1: INTRODUCTION

1.1 Background

The goal of tomography is to estimate physical parameters such as the electron density at each point in a three dimensional object [1]. Since x-rays provide penetration through otherwise opaque targets, x-ray tomography is an established field for non-destructive examination and is widely used in medicine, security, and quality inspection. The primary contributions of this work are new modalities for tomography, enabled by reuniting coded apertures with x-rays through scatter imaging. These techniques are collectively termed “coded aperture x-ray scatter imaging” (CAXSI). An enabling feature of CAXSI is the design of a new family of coded apertures called “frequency scale codes” which provide maximum distinguishability of scatter points at different ranges from a detector. For a review on imaging modalities in x-ray tomography without coded apertures, see Reference [2].

The most popular and mature x-ray techniques operate in attenuation mode, where some fraction of the x-rays illuminating a target object are absorbed or deflected from the direct ray path connecting the x-ray source and detector. By definition, the measured photons in attenuation imaging are those which did not interact with the object and thus provide limited information. In scatter imaging, scattered photons are measured, providing a number of advantages and novel results which will be discussed presently.

For x-ray photons with energies in the range 1 keV to 1 MeV, the dominant interactions with matter are photoelectric absorption, incoherent scattering, coherent scattering, and fluorescence. All of these mechanisms contribute to each attenuation measurement, but scatter imaging systems have the freedom to measure each contribution separately. Photoelectric absorption and incoherent scattering are most useful for estimating bulk electron

density. Density imaging based on fluorescence is also possible using the isotropic scattering models presented in later chapters, and since fluorescence is based on atomic transitions it can reveal concentrations of atomic constituents if the transition energies are detectable. While fluorescence probes atomic structure, coherent scattering exhibits interference effects between neighboring atoms which can tell us about molecular structure. This is the motivator for coherent scatter imaging, where diffraction profiles are estimated for each point in an extended object. In the following, you will see demonstrations and examples of x-ray tomography systems for density imaging based on incoherent scattering and for molecular imaging based on coherent scattering.

The basic model for an x-ray tomography system is shown in Figure 1.1 and consists of an x-ray source, beam-forming optical element(s), the target object, detector-side optical element(s), and detector arrays for attenuation and/or scatter measurements.

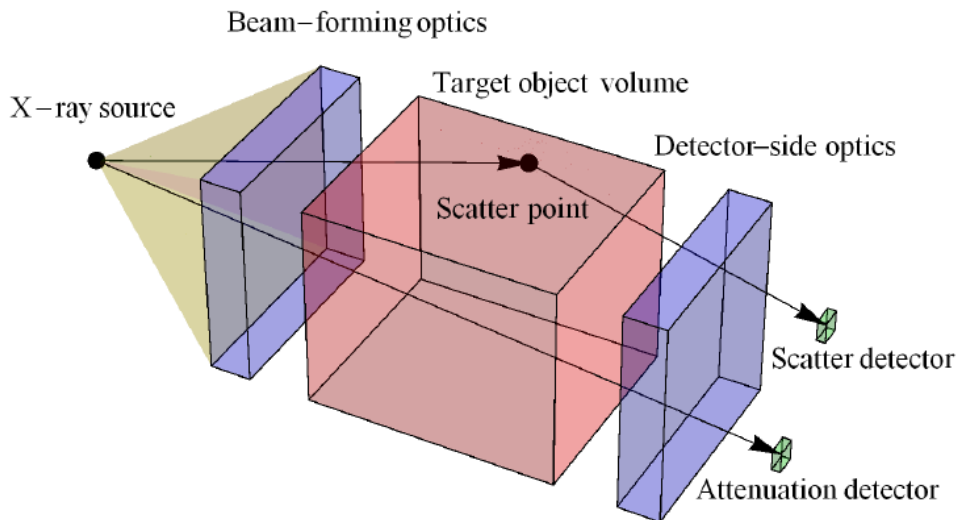


Figure 1.1: Basic elements of an x-ray tomography system, including the x-ray source, beam-forming optics, the target object volume, detector-side optics, and attenuation or scatter detectors.

The x-ray source is considered here to be point-like and may emit a narrow-band or broad-band spectrum. Since focusing is difficult at x-ray energies, assume the optical elements rely on absorption and consist of high-density metals such as lead or tungsten. These form a

class of reference structures, which partition the object into sensitivity regions specific to each detector and enable tomography [3,4]. The source-side reference structures considered here are pinhole and slit collimators, respectively forming pencil beams and fan beams as shown in Figure 1.2. The exception is Chapter 5, which concerns volumetric scatter imaging with full cone beam illumination. In principle, a 3D object may be translated through the pencil or fan beam to scan its full volume. X-rays transmitted or scattered by the object encounter detector-side optics before reaching the detectors. For the attenuation detectors, these usually consist of anti-scatter grids which are angled collimators focused on the source to reject scattered radiation. Until recently, scatter measurements have employed similar collimators focused on individual object points. Unfortunately, most of the scattered signal is thereby wasted through absorption since the collimators only transmit a narrow range of angles.

The novelty of CAXSI is the introduction of coded apertures to scatter imaging. Coded apertures, being planar reference structures, have a spatially varying transmittance. Unlike collimators, they transmit rays with a wide range of incidence angles, producing measurements with multiple sensitivity regions in the object and increased signal levels. Coded apertures enable new imaging modalities, increase signal-to-noise and throughput, and reduce dose compared with other techniques. The focus of this work is to analyze and demonstrate these modalities and design appropriate coded apertures.

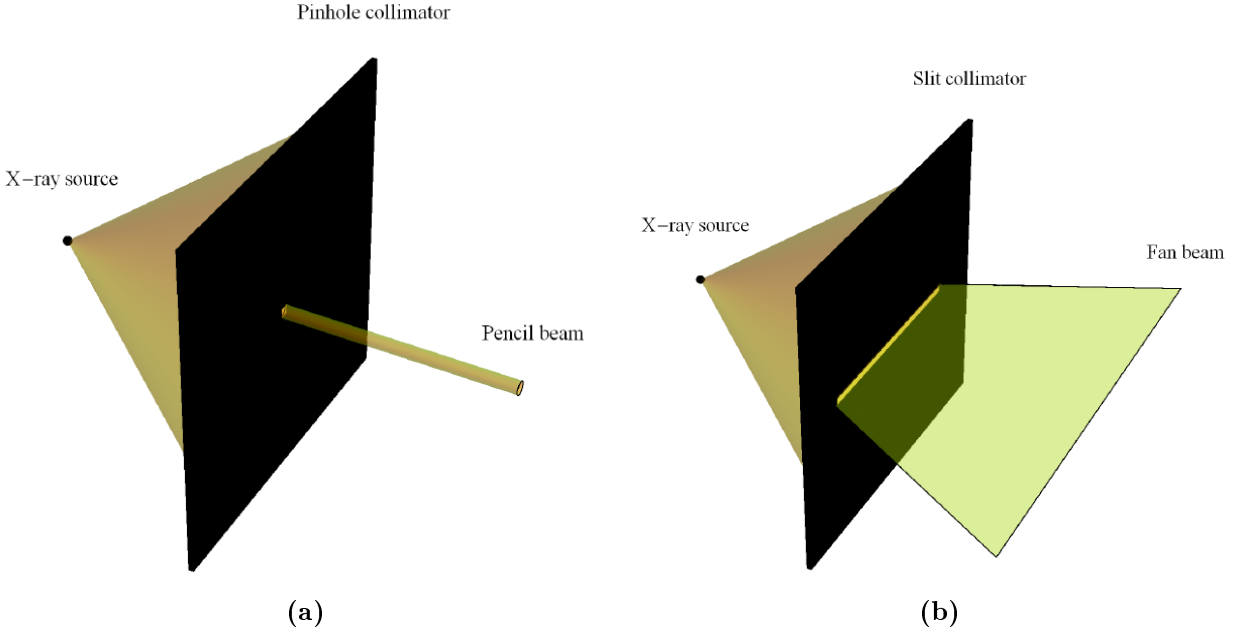


Figure 1.2: (a) Pencil beam and (b) fan beam collimation

Attenuation imaging has two major challenges which scatter imaging can overcome. First, the line integrals in attenuation imaging only exist along lines connecting the source(s) and detector(s), severely constraining the set of measurable rays. A “ray” is a straight line segment connecting two points, along which radiation propagates under the assumptions of geometric optics. Multiple measurements along different line integrals are required to isolate the contribution of individual voxels to the attenuation. Computed tomography (CT) is a technique developed specifically for the purposes of untangling these line integrals [1]. In most CT systems the object is rotated relative to the source/detector apparatus in order to achieve ray diversity via the x-ray transform, with requirements on what constitutes a complete set of measurements [5, 6]. While multi-source CT systems exist [7], the vast majority of CT systems employ a single moving x-ray source and require a stationary target during the course of the measurement. “Radon imaging” is based on the simplest model for attenuation measurements, the Radon transform. The Radon transform is a set of parallel projections in a plane. Fan beam Radon imaging is also possible, where the parallel rays are simply reordered into fans, and similar approaches exist for cone beam tomography [1].

However, none of these methods provide tomography along a single line without irradiating at least a planar section of the object and acquiring a sequence of images.

In contrast with attenuation imaging, scatter imaging benefits from the natural diversity of scattered rays. For each ray incident on a scattering object, multiple scattered rays are produced in different directions. Exploited properly, this means that a linear or planar section of the target may be imaged in a snapshot (a single exposure of a detector array) without the need for moving parts or multiple sources. Careful selection of scattered rays is important for minimizing radiation doses and/or maximizing throughput in tomographic systems. The ability to perform 1D tomography with a pencil beam alleviates the need to irradiate neighboring regions. In Chapter 2, theoretical analysis of 1D and 2D scatter imaging techniques shows that they could provide significant reduction in radiation dose compared with alternative methods.

The second challenge for attenuation systems is material discrimination. Attenuation provides density information and effective atomic number when dual-energy (DE) or multi-energy (ME) measurements are made via photon counting detectors and/or spectral filtering at the source or detector. For DE measurements, density and effective atomic number are the only measurable properties. For ME measurements, relative combinations of atomic numbers can be discerned but only if the absorption features (e.g. K-edges) or fluorescence energies of the constituent atoms falls within the detection energy range. For many applications, these features occur at energies too low to sufficiently penetrate the target. Incoherent scattering has been used instead of attenuation for density imaging [2,8–14], and specialized Radon methods have also been proposed for cone beam incoherent scatter tomography [15]. Incoherent scattering, however, lacks information about chemical structure since each electron contributes independently to the incoherent scattered radiation.

Coherent scattering provides much richer atomic and molecular information than attenuation or incoherent scattering. Coherent scattering exhibits interference in the scatter angle for materials with periodic structure [16]. In the simplest approximation, atoms located

at crystal lattice sites become polarized and emit dipole radiation at the same frequency as an incident field. Interference from neighboring atoms produces a scattered intensity which can be a quickly-varying function of the scatter angle. This intensity is closely related to the spatial Fourier transform of the electron density, providing important information about the spatial arrangement of the atoms or molecules. Similar effects occur in liquids and amorphous solids as in crystals, but with more smoothly-varying scattered fields. The coherently-scattered (diffracted) field depends strongly on both the x-ray energy as well as the molecular structure of the target, and therefore provides a non-destructive chemical probe.

X-ray diffraction for chemical detection is a mature field [17, 18]. A typical diffraction experiment involves a small, point-like target and 1D x-ray illumination. Energy resolution is achieved either by a narrow-band x-ray source or energy-sensitive detectors. Localization in energy and space simplifies the relationship between the measurements and the chemical structure of the target.

Coherent scatter imaging is a relatively new field in which scatter/diffraction measurements are made over an extended volume to measure the spatial and chemical configuration of a target. Coherent scatter imaging systems fall into three basic categories: selected volume tomography (SVT) [13, 19–25], coherent scatter computed tomography (CSCT) [26–30], and coded aperture x-ray scatter imaging (CAXSI) [31–35].

In the SVT category, collimators form 1D or 2D illumination and each detector pixel is collimated for sensitivity to a single localized volume element (voxel) within the beam. With SVT, each voxel may be treated as an independent diffraction experiment which provides the simplest imaging process. In order to minimize cross-talk between neighboring voxels the collimators must consist of strongly absorbing materials and maintain a limited angle of acceptance, causing the vast majority of the scattered photons to be wasted and contributing to low signal-to-noise ratio (SNR). This consideration motivated the second category of scatter imaging systems, CSCT, which was developed as a multiplexed alternative to SVT.

CSCT can be achieved with 2D illumination and detector pixels collimated to individual lines of voxels. The wider acceptance angle of the collimators improves throughput compared with SVT. CSCT cleverly adapts the mathematical framework of CT, providing analytic image reconstruction and error bounds [36]. Like CT, however, CSCT requires rotational scanning and cannot be used for snapshot tomography.

The newest category of scatter imaging techniques is coded aperture x-ray scatter imaging (CAXSI) [31–35]. The novelty of CAXSI is that the detector-side collimator is replaced by a coded aperture with a carefully designed transmittance pattern. The aperture is constructed with enough angular acceptance to measure scatter from any illuminated region of the object, so that each detector pixel is sensitive to a different combination of voxels. With a sufficient number of linearly independent measurements the target may be reconstructed from the measurements. Measurement diversity may be achieved by any combination of adding detector pixels, changing the code pattern, moving the object, and/or moving the source and detectors. Using CAXSI, a 1D or 2D tomographic section of the object may be reconstructed from a snapshot and without unnecessary irradiation of adjacent regions. Additionally, SNR and throughput are improved since viable aperture codes exist with average transmittance of about 50%. The scatter signal acquired in a CAXSI system is one and two orders of magnitude larger than with CSCT and SVT, respectively. CAXSI powerfully combines coded apertures with x-ray scatter imaging to enable new imaging modalities and improvements in image quality, acquisition speed, and chemical specificity.

This document presents theory and analysis for pencil, fan, and cone beam CAXSI. The pencil beam and fan beam systems were demonstrated experimentally and based on the theoretical analysis of Chapter 2. The remainder of this section presents the principles of x-ray scattering along with analytic and computational techniques used for scatter imaging. Chapter 2 presents published theory and coded aperture designs for pencil and fan beam CAXSI, and compares CAXSI, SVT, and CT in terms of the singular values of their associated measurement models. Chapter 3 adapts published experimental results for pencil beam

CAXSI, in which density and chemical structure is recovered from a single snapshot along a 1D pencil beam. This is extended in Chapter 4, demonstrating snapshot 2D tomography and building on the lessons of the pencil beam system. Chapter 5 extends the ideas of its preceding chapters and proposes new coded apertures and reconstruction algorithms for cone beam scatter tomography. Chapter 6 compares models for systems incorporating linear arrays of spectroscopic (energy-sensitive) detectors. Finally, Chapter 7 provides a summary of this work and an outlook on the future of CAXSI.

1.2 Scatter imaging principles

Photoelectric absorption, incoherent scattering, and coherent scattering are the dominant x-ray interactions with matter for photons in the 1 keV to 1 MeV energy range [37]. Figure 1.3 illustrates the two scattering mechanisms considered here. Incoherent scattering arises when a free or weakly bound electron absorbs energy from a photon and recoils. The energy transfer produces a shift in the photon's wavelength, known as the Compton shift. The amount of energy transferred to the electron is a random variable in this quantum process, but it is correlated with the scattering angle through energy and momentum conservation.

Coherent scattering may be understood classically, where an incident field excites dipole radiation in atoms. If the atoms are organized according to some chemical structure, the radiated fields interfere and can produce highly directional radiation.

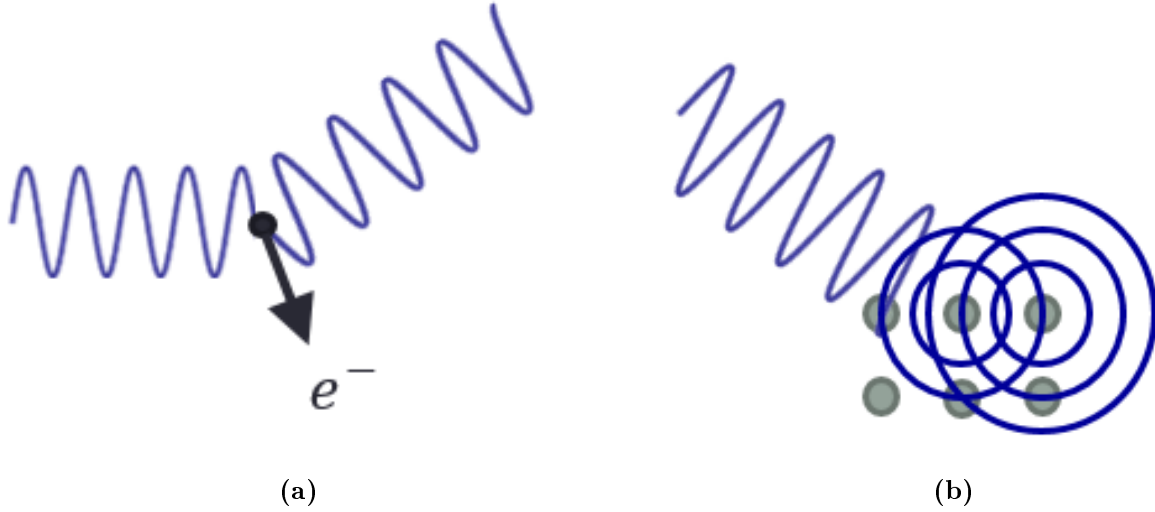


Figure 1.3: Schematic representations of the two dominant x-ray scattering mechanisms considered here: (a) incoherent (Compton) scattering, and (b) coherent (Bragg) scattering. The sinusoids represent incident and scattered plane-waves. The e^- in (a) is a scattered electron. The gray circles in (b) are atoms positioned on a crystal lattice, and the concentric rings are contributions from each atom to the scattered field.

The scattering cross section σ is well approximated by a superposition of the individual cross sections: $\sigma = \sigma_P + \sigma_I + \sigma_C$, where σ_P is for photoelectric absorption, σ_I is for incoherent scattering, and σ_C is for coherent scattering. These cross sections are functions of the photon energy E and have been measured and tabulated for a variety of materials [38]. The angular differential cross section $\frac{d\sigma}{d\Omega}(\theta, \phi)$ is an even more complete description of a material's scattering properties and defined such that $\sigma = \int d\Omega \frac{d\sigma}{d\Omega}(\theta, \phi)$. The solid angle element is $d\Omega = \sin\theta d\theta d\phi$, and the polar angle θ is called hereafter the “scatter angle”, with $\theta = 0$ being the direction of the incident illumination. Like σ , the differential cross section also depends on E . In the following section, scatter measurements will be described in terms of the incoherent differential cross section $\frac{d\sigma_I}{d\Omega}$ and the coherent differential cross section $\frac{d\sigma_C}{d\Omega}$.

1.2.1 Scattering from a point

All imaging begins with points [39]. In this spirit, consider a simple scattering experiment which is depicted in Figure 1.4.

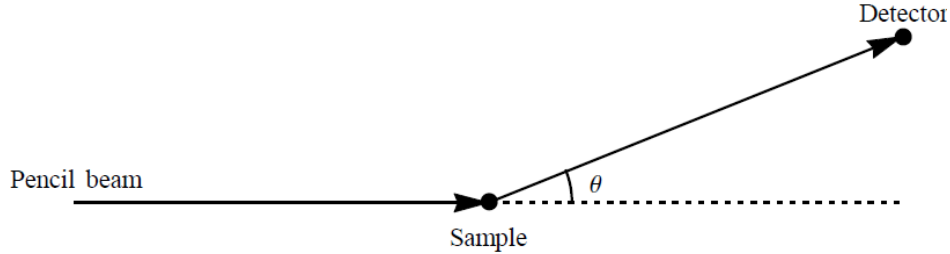


Figure 1.4: A simple x-ray scattering experiment, including a pencil beam, a point-like sample, and a spectroscopic scatter detector.

A pencil beam with spectral number density $N(E)$ illuminates a point-like sample with thickness z and electron density n , which scatters rays into multiple directions. The detector is assumed to cover an infinitesimal solid angle Ω and positioned so that only x-rays with scatter angle θ are measured. The detector operates in photon counting mode, and adds each count to the appropriate energy bin. This is an example of an “energy sensitive” detector (Chapter 6 analyzes the performance of CAXSI systems employing arrays of such detectors). Letting $\eta_i(E)$ be the probability that a detected photon with energy E is added to bin i , the mean number of photons collected in energy bin i may be represented as a contribution from incoherent and coherent scattering:

$$g_i = zn\Omega \int dE N(E) \left[\eta_i(E') \frac{d\sigma_I}{d\Omega}(E, \theta) + \eta_i(E) \frac{d\sigma_C}{d\Omega}(E, \theta) \right]. \quad (1.1)$$

Equation (1.1) is called the “forward model” for the point scattering experiment. The particulars of the energy and angle ranges measured, as well as the target’s material properties, will determine which of these terms is dominant for a given measurement. The short x-ray wavelength compared with the periodicity of atoms in molecules causes coherent scattering to occur primarily in the forward direction at small θ . Incoherent scattering, however, is found at all θ , and is relatively smoothly varying in energy and angle. The differential cross section for incoherent scattering is well approximated by the Klein-Nishina formula [40], which has a peak at $\theta = 0$ and another at $\theta = 180^\circ$. In equation (1.1), $E' = E / [1 + \frac{E}{mc^2} (1 - \cos \theta)]$ is the Compton-shifted energy for a photon at initial energy E and with scatter angle θ ,

where mc^2 is the rest mass energy of the electron. Pencil beam tomography using incoherent scattering is possible with a single pixel and without detector side collimation by using energy sensitive detectors to find θ through E and E' [8]. However, for “energy integrating” detectors (those without energy resolution), $\eta_i(E') \approx \eta_i(E)$ and the Compton shift is not resolved. In this case, tomography is possible only through SVT or CAXSI, with signal strength being the advantage of the latter. Energy integrating detectors, based on scintillation or direct detection, will be assumed for Chapters 2-5.

The coherent scatter differential cross section $\frac{d\sigma_C}{d\Omega}$ carries information about the spatial distribution of the electron charge, which may be used to identify the scattering material. Relaxing the assumption of a point-like target just slightly, let $n(\mathbf{r})$ be the target’s electron density as a function of position \mathbf{r} . For an incident field with wavevector \mathbf{k}_i proportional to $e^{i\mathbf{k}_i \cdot \mathbf{r}}$, the phase at scattering point \mathbf{r} is $\mathbf{k}_i \cdot \mathbf{r}$. The amplitude of the scattered wave from point \mathbf{r} is proportional to the electron density $n(\mathbf{r})$. The scattered wave with wavevector \mathbf{k}_f suffers a phase lag of $-\mathbf{k}_f \cdot \mathbf{r}$ relative to the point \mathbf{r} . The total scattered field at wavevector \mathbf{k}_f is a volume integral over $n(\mathbf{r})$, with the phase factor $e^{i(\mathbf{k}_i - \mathbf{k}_f) \cdot \mathbf{r}}$ [16]:

$$\mathcal{E}(\mathbf{k}_f) = \int d^3\mathbf{r} n(\mathbf{r}) e^{i(\mathbf{k}_i - \mathbf{k}_f) \cdot \mathbf{r}},$$

to within some proportionality. The spectral irradiance of the field is proportional to $|\mathcal{E}(\mathbf{k}_f)|^2$, motivating the following definition for the “scattering density”:

$$F(\mathbf{q}) = \left| \int d^3\mathbf{r} e^{-i\mathbf{q} \cdot \mathbf{r}/\hbar} n(\mathbf{r}) \right|^2,$$

where the vector $\mathbf{q} = \hbar(\mathbf{k}_f - \mathbf{k}_i)$ is called the “momentum transfer”, and \hbar is the reduced Planck constant. Jumping from the wave picture to a particle description, an incident photon has the momentum vector $\mathbf{p}_i = \hbar\mathbf{k}_i$ and after scattering its final momentum is $\mathbf{p}_f = \hbar\mathbf{k}_f$. The momentum transfer $\mathbf{q} = \mathbf{p}_f - \mathbf{p}_i$ is the momentum gained by the photon during the scattering process, as illustrated by Figure 1.5.

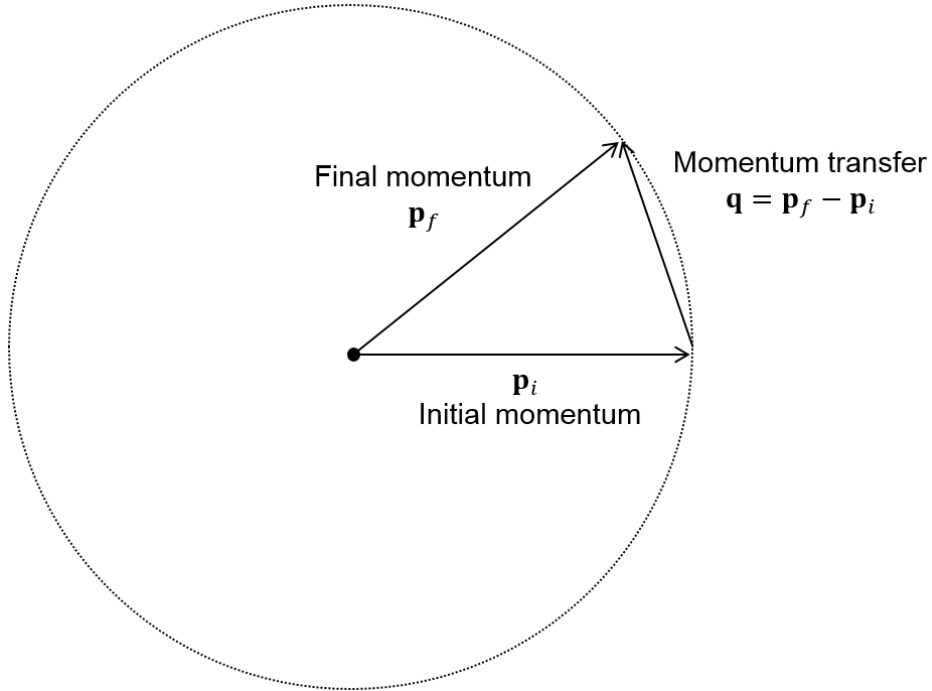


Figure 1.5: Graphical definition of the momentum transfer $\mathbf{q} = \mathbf{p}_f - \mathbf{p}_i$. For coherent scattering, $|\mathbf{p}_f| = |\mathbf{p}_i|$ and both vectors lie on the surface of a sphere (the Ewald sphere).

In component form, the initial and final photon momenta are

$$\mathbf{p}_i = \frac{E}{c} \begin{pmatrix} 0 \\ 0 \\ 1 \end{pmatrix}$$

$$\mathbf{p}_f = \frac{E}{c} \begin{pmatrix} \sin \theta \cos \phi \\ \sin \theta \sin \phi \\ \cos \theta \end{pmatrix}$$

where θ is the polar angle in spherical coordinates and ϕ is the azimuthal angle. The coherent scattering condition means that the photon does not lose energy in the process, so

$|\mathbf{p}_i| = |\mathbf{p}_f| = E/c$. The components of the momentum transfer $\mathbf{q} = \mathbf{p}_f - \mathbf{p}_i$ are

$$\mathbf{q} = \frac{E}{c} \begin{pmatrix} \sin \theta \cos \phi \\ \sin \theta \sin \phi \\ \cos \theta - 1 \end{pmatrix} \quad (1.2)$$

The magnitude q of the momentum transfer vector gives us Bragg's law

$$q = \frac{2E}{c} \sin \frac{\theta}{2}, \quad (1.3)$$

relating the momentum transfer magnitude q , x-ray energy E , and the scatter angle θ . Equation (1.3) describes only the first diffraction order $M = 1$; higher orders are obtained by multiplying the left hand side by the order number M . In what follows, all diffraction orders except the first are ignored.

In crystals, $F(\mathbf{q})$ is nonzero only when \mathbf{q}/\hbar is approximately equal to a reciprocal lattice vector. For a crystalline powder, averaging $F(\mathbf{q})$ over the random distribution of grain orientations produces a scattering density depending only on the magnitude q of the momentum transfer. This approximation breaks down as the grain size increases, but the simplification is even more exact for liquids and amorphous solids. Then, the scattering density is reduced to a function of a single parameter, $F(q)$, and the scattered radiation is said to possess azimuthal symmetry (it is independent of ϕ). Azimuthally symmetric scattering is analyzed in Chapter 2 and assumed in the forward models for coherent scatter imaging in Chapters 3, 4, and 6. The approximation $F(\mathbf{q}) \approx F(q)$ is justified when the spatial imaging resolution is much larger than the length scale at which the material is disordered.

The differential cross section $\frac{d\sigma_C}{d\Omega}(E, \theta)$ and the scattering density $F(q = \frac{2E}{c} \sin \frac{\theta}{2})$ are both proportional to the probability that a photon at energy E scatters into the direction determined by θ . The differential cross section is expressed in terms of the scattering density

as

$$\frac{d\sigma_C}{d\Omega}(E, \theta) = A(E) (1 + \cos^2 \theta) F \left(q = \frac{2E}{c} \sin \frac{\theta}{2} \right) \quad (1.4)$$

where $A(E)$ is a normalization factor for each E so that $\int d\Omega \frac{d\sigma_C}{d\Omega}(E, \theta) = \sigma_C(E)$, and $\sigma_C(E)$ is the total coherent scatter cross section, e.g. as reported by NIST [38]. Appendix A discusses this normalization and how to compute $F(q)$ and $\frac{d\sigma_C}{d\Omega}(E, \theta)$ for arbitrary q , E , and θ from diffractometer measurements and knowledge of $\sigma_C(E)$. The factor $(1 + \cos^2 \theta)$ in equation (1.4) is proportional to the Thompson scattering factor (the low energy limit), which arises since the scattered field has two polarization components and one of them (the “radial” component) follows a $\cos^2 \theta$ dependence for the intensity.

Bragg’s relationship (1.3) between two experimental parameters E and θ and the object-specific parameter q enables multiple modalities for diffraction measurements. Measurement of the scattering density at different q values is achieved by varying θ with fixed E (angle-dispersive), or varying E with fixed θ (energy-dispersive). Because of the limited acceptance angle of the collimators, SVT requires energy dispersive measurements to recover $F(q)$ [22]. Both angle and energy dispersive measurements have been demonstrated in CSCT [26, 28, 30] and CAXSI [31, 32, 34, 35] systems. Angle-dispersive CAXSI is the focus of Chapters 2, 3, and 4. There exists a continuum between angle-dispersive and energy-dispersive measurements in which both E and θ vary, which is analyzed in Chapter 6.

Some comments on simplifying the forward model (1.1) are in order. Small angle scattering is assumed for coherent scattering, so that $\cos^2 \theta \approx 1$. Incoherent scattering is only considered for energy-integrating detectors, so $\eta_i(E') \approx \eta_i(E)$, and it is treated as approximately isotropic. The coherent and incoherent contributions may be grouped into a total scattering cross section according to $\sigma_S = \sigma_I + \sigma_C$:

$$g_i = nz\Omega \int dE \eta_i(E) N(E) \frac{d\sigma_S}{d\Omega}(E, \theta)$$

Some different limits of this forward model enable different measurement strategies. First, assume a narrow-band source so that $N(E) \rightarrow \delta(E - E_0)$ and assume a perfect energy-insensitive detector with $\eta = 1$, where the index i has been dropped since there is only a single energy bin. The forward model in this case is

$$g = nz\Omega \frac{d\sigma_S}{d\Omega}(E_0, \theta),$$

which essentially the forward model for SVT. If n is the unknown density of a given voxel in SVT, it can be recovered with an appropriate model for $z\Omega \frac{d\sigma_S}{d\Omega}(E_0, \theta)$. This was the approach of Lale for incoherent SVT [19]. To recover $F(q)$ when coherent scattering is measured, angle dispersive measurements would scan $g(\theta)$ to recover $F(q) \propto g\left(\theta = 2 \sin^{-1} \left[\frac{qc}{2E_0} \right]\right)$. This approach is used in commercial diffractometers for small, point-like samples at known locations.

For common broadband x-ray tubes, narrow-band spectra most easily achieved through heavy filtration, wasting much of the incident flux. If the source is broadband, recovery of $F(q)$ from $g(\theta)$ results in a deconvolution problem which can be ill-posed. To overcome this problem for coherent scatter SVT, Harding and Kosanetzky took the energy-dispersive approach [22]. Their energy-sensitive detector remained at a fixed angle θ_0 and had a number of energy bins so that, effectively, $g(E)$ was measured. The coherent scatter forward model is then

$$g(E) = nz\Omega N(E)\eta(E)k(E)F\left(q = \frac{2E}{c} \sin \frac{\theta_0}{2}\right) \quad (1.5)$$

and the scattering density was recovered through $F(q) \propto g\left(E = \frac{qc}{2 \sin \frac{\theta_0}{2}}\right)$, with assumed models for the other terms. Despite the low throughput of SVT, this is so far the most popular method for coherent scatter tomography due to its simplicity.

1.2.2 Forward models for volume imaging

The principles of point scattering from the previous section can be assumed at each position in a 3D object, with the total measurements being a superposition of the contributions from each point. This superposition principle applies best to weakly attenuating/scattering objects where the primary scatter is a mere perturbation of the incident beam and the secondary scatter is a small perturbation of the primary scatter. In the remainder of this work, perturbations of the incident and scattered radiation are assumed negligible or otherwise corrected-for. The result is that the forward model becomes a linear transformation of the scattering density F .

The purpose of scatter imaging is to estimate some combination of physical properties, such as electron density and/or $F(q)$, over the volume of the object. The imaging process may be considered as a transformation H from the object's now spatially-dependent scattering density $F(\mathbf{r}, q)$ to the measured field $G(\mathbf{r}', E)$, where $\mathbf{r} = (x, y, z)$ is a position vector in the object, $\mathbf{r}' = (x', y', z')$ is a measurement position, q is the momentum transfer, and E is the measured photon energy. The job is to estimate F (the object) from G (the measurements), given a system model H . In general, H may be a nonlinear transformation of F due to multiple scattering effects and/or attenuation of the x-rays within the object, however for simplicity a linear model is assumed in this work (with the exception of a bi-linear model in Chapter 4). The techniques described here may be extended to iterative update of a nonlinear H during the reconstruction process.

Good system design produces transformation H which is at least approximately invertible. The simplest approach is to reduce the dimensionality of the space embedding the object and replace the remaining coordinates with time t using scanning techniques. The object is constrained to effectively one spatial dimension with pencil beam illumination and two spatial dimensions with fan beam illumination. The forward model for single-pixel incoherent SVT is basically of the form $F(\mathbf{r}) \delta^3(\mathbf{r} - \mathbf{s}(t)) \rightarrow G(t)$ for some voxel path $\mathbf{s}(t)$, and δ^3 is the Dirac delta function in 3D, which may be replaced by a function describing the

shape of the actual voxels. Energy-dispersive SVT measures the coherent scattering density via $F(\mathbf{r}, q) \delta^3(\mathbf{r} - \mathbf{s}(t)) \rightarrow G(E, t)$. SVT may also employ pixel arrays to capture one or two spatial dimensions of F in parallel. CSCT rotates $F(x, z, q)$ and obtains energy-integrated measurements $G(x, y, t)$ or energy-sensitive measurements $G(x, E, t)$. SVT and CSCT both employ detector-side collimation to limit the domain of F which is visible to each detector pixel. CAXSI provides an alternative approach using coded apertures with wide angular acceptance, increasing the fraction of the scattered radiation reaching the detectors.

Chapter 2 presents theory and analysis for incoherent and coherent CAXSI systems, including coded apertures for forward models with $F(z) \rightarrow G(x)$, $F(z, \theta) \rightarrow G(x, y)$, and $F(x, z) \rightarrow G(x, y)$. In Chapter 3, the coherent scattering density $F(z, q)$ was reconstructed from an experimentally-measured $G(x, y)$, which is closely related to the transformation $F(z, \theta) \rightarrow G(x, y)$ discussed theoretically in Chapter 2. In Chapter 4, the object was assumed separable as $F(x, z)R(\theta)$, where the radiance $R(\theta)$ included both coherent and incoherent scattering. The functions $F(x, z)$ and $R(\theta)$ were both estimated from the experimental image $G(x, y)$. In chapter 5, coded apertures are proposed for volumetric tomography following $F(x, y, z) \rightarrow G(x, y, t)$. Chapter 6 compares forward models for energy sensitive measurements according to the transformation $F(z, q) \rightarrow G(x, E)$.

1.3 Coded apertures

At x-ray energies, focusing optics are often impractical due to their low efficiency stemming from the weak interaction of x-rays with matter. Coded apertures offer an alternative to focal elements, consisting of specially designed 2D patterns of opaque material (usually lead, tungsten, or some other heavy element). Rays intersecting a coded aperture are ideally either absorbed or transmitted without changing their direction. Coded apertures should be thin enough to accept a range of incidence angles at the transparent regions, but should also be thick enough to provide sufficient contrast at the opaque regions. This balance has implications for imaging resolution, where the feature size of the aperture pattern is limited by the aspect ratio achievable during the manufacturing process. For simplicity, the forward

models presented in the following chapters assume a planar aperture, with an exception in Chapter 6 which requires modeling of the 3D aperture due to an energy dependent forward model. For each coded apertures system, resolution metrics are presented in terms of the smallest length scale of the aperture pattern, however it may be decided.

In spectroscopy, coded apertures have been used as early as 1949 [41] to overcome resolution versus throughput tradeoffs. By multiplexing signals together, spectra may be reconstructed with signal to noise ratio (SNR) superior to single slit diffraction. From this concept the field of Hadamard transform spectroscopy developed and has become a testament to the power of multiplexing [42]. Recent studies show that novel codes in combination with biased, nonlinear and/or decompressive estimators may provide a powerful tool for compressive sampling [4]. Coded apertures may also be viewed as “light field” encoders that enable radiance measurement using irradiance detectors [43]. Building on studies of “reference structures” for compressive tomographic imaging [3, 44, 45], coded aperture snapshot spectral imaging (CASSI) was developed in 2007 to measure a 3D spatial-spectral scene from 2D measurements at visible and ultraviolet wavelengths [46, 47]. In 2009, an extension of this approach was proposed for compressive x-ray tomography [48]. In each of these examples, coded apertures are used to alleviate space-time-spectral trade-offs and enable snapshot acquisition of data conventionally recorded sequentially. For sparse or compressible objects coded aperture multiplexing can improve system sensitivity and signal to noise ratio even when photon noise is dominant [49].

Coded apertures also found early use in x-ray astronomy, where lenses are impractical and the scene consists of point-like objects (stars) in a “cold” background. A predecessor to the coded aperture system, the pinhole camera exhibits a classic tradeoff between throughput and resolution similar to single slit spectroscopy. Increasing the size of the pinhole accepts more photons but blurs the measured image. In 1962, Mertz and Young used coded apertures based on Fresnel Zone Plates to beat the throughput versus resolution tradeoff of pinhole imaging [50]. Their scheme allowed optical reconstruction via holography or digital reconstruction.

Reference [51] provides a good description of their approach and an application to gamma rays. Inspired by digital reconstruction, in 1968 Ables [52] and Dicke [53] each proposed correlational imaging in which pinholes are positioned randomly in 2D to form a coded aperture. By correlating the measured image with the pinhole pattern, the image can be reconstructed with higher SNR than a single pinhole can provide for the same resolution. Later work improved the design of these coded apertures by considering their correlation properties [54–56].

Most of the coded apertures discussed above are types of “shift codes” and are well-suited for x-ray astronomy and other applications where the goal is transverse 2D imaging. An ideal shift code with transmittance $T(x)$ will possess a correlational inverse $\hat{T}(x)$ such that $\int dx T(x)\hat{T}(x-a) = \delta(a)$, where $\delta(\dots)$ is the Dirac delta function. For incoherent imaging, the transmittance is constrained to $0 \leq T(x) \leq 1$ but $\hat{T}(x)$ can take any value since it is applied digitally. However, object points at different ranges will produce different magnifications of $T(x)$, and the shift codes then lose their nice orthogonality properties. When shift codes are applied to 3D objects, a slice at a certain depth may be put into focus but it will still contain background contributions from the other slices, preventing true tomography.

A central theme of this work is the use of scale codes based on sinusoid functions, which were chosen based on their distinguishability under magnification. For a scale code $T(x)$, there exists an inverse $\hat{T}(x)$ so that $\int dx T(x)\hat{T}(xa) = \delta(a-1)$. Scale codes are used in subsequent chapters to provide resolution in the direction normal to a detector array (“range”), and are combined with the shift code of Reference [56] for snapshot tomography perpendicular to the detector plane. Orthogonality conditions can also be constructed for rotational codes, which are introduced in Chapter 2. Chapter 5 generalizes the scale codes used to a new family of “frequency scale codes” (FSC) for 3D tomography, along with associated reconstruction algorithms based on Fourier analysis.

1.4 Discretization of the forward model

The forward models considered here describe linear transformations between continuous fields. In practice, discretization occurs at the detector during the digital measurement process and at the object during digital reconstruction. In the following, the object-space coordinates are combined into the 4D vector $\mathbf{x} = (\mathbf{r}, q)$ and similarly for the measurement coordinates $\mathbf{x}' = (\mathbf{r}', E)$.

Experimental measurements are modeled as random variables, with mean values given by discrete projections of the spectral irradiance $G(\mathbf{x}')$. The measurements are modeled according to detector response functions $\{\Phi_i(\mathbf{x}')\}_{i=1\dots M}$, where M is the number of measured values. The expected value of the i^{th} measurement is $g_i = \int d\mathbf{x}' \Phi_i(\mathbf{x}') G(\mathbf{x}')$, where the integral extends over the support of $\Phi_i(\mathbf{x}')$. A similar discretization for the object is possible over basis functions $\{\Psi_j(\mathbf{x})\}_{j=1\dots N}$, where N is the number of unknown object coefficients. The j^{th} object coefficient is $f_j = \int d\mathbf{x} \Psi_j(\mathbf{x}) F(\mathbf{x})$. Here, orthonormal but not necessarily complete bases for Φ and Ψ are assumed.

An important consideration is that the measurement response functions are based on physical devices, however the object basis may be chosen to suit a particular problem since it is merely a computational construct. In truncated singular value decomposition [4], the object basis consists of the right singular vectors of H (singular value decomposition is discussed in Section 1.6 below). Choosing another object basis in which F is compressible or sparse is the concept behind compressed sensing [57,58]. For compressible objects, shockingly few measurements are required to recover the function F with high fidelity, even in the presence of extreme noise. This revelation has led to a flurry of activity in the past decade, applying compressive techniques in almost every field of imaging, communications, and signal recovery [4].

The discrete forward model is

$$g_i = \sum_{j=1}^N f_j \int d\mathbf{r}' \Phi_i(\mathbf{r}') \int d\mathbf{r} \Psi_j(\mathbf{r}) H(\mathbf{r}'; \mathbf{r})$$

$$\begin{aligned}
&= \sum_{j=1}^N H_{ij} f_j \\
\mathbf{g} &= \mathbf{H}\mathbf{f}
\end{aligned} \tag{1.6}$$

where the components of the forward matrix \mathbf{H} are defined as H_{ij} in going from the first to second line. The third line puts the model in matrix form, defining vectors \mathbf{g} and \mathbf{f} with components g_i and f_j , respectively. The result is a linear system with M equations and N unknowns. In general, $M \neq N$ and the inverse \mathbf{H}^{-1} does not exist. Even if it does exist, estimating $\hat{\mathbf{f}} = \mathbf{H}^{-1}\tilde{\mathbf{g}}$, where $\tilde{\mathbf{g}}$ is a noisy measurement of \mathbf{g} , may amplify the noise and produce poor recovery of \mathbf{f} . The solution is to develop reconstruction algorithms specific to the noise statistics, as discussed in the next section.

1.5 Reconstruction algorithms

Two basic classes of reconstruction algorithms exist: direct and iterative. For direct reconstruction, an approximate inverse $\tilde{\mathbf{H}}$ is used in place of \mathbf{H}^{-1} . The estimated object is then $\hat{\mathbf{f}} = \tilde{\mathbf{H}}\tilde{\mathbf{g}}$, where $\tilde{\mathbf{g}}$ is the noisy data with mean given by \mathbf{g} . CT, SVT, and CSCT, all enable direct reconstruction with a linear estimator $\tilde{\mathbf{H}}$. The second class of algorithms is iterative, meaning that the estimate $\hat{\mathbf{f}}$ is the limit of a converging sequence updated at each iteration. Iterative reconstruction involves maximizing an objective function. When the objective function is a likelihood function based on the statistics of the measurement noise the algorithm is called a Maximum Likelihood Estimator (MLE). To a good approximation for most imaging systems, photon counting measurements at x-ray energies are shot-noise limited. The result is a Poisson-distributed count rate at each pixel and energy channel. The resulting Poisson MLE algorithms are used for the reconstructions in this work. These estimators are iterative and do not require construction of $\tilde{\mathbf{H}}$ or \mathbf{H}^{-1} . The derivation of the MLE algorithms used here are based on applying Poisson statistics to References [59, 60]. Maximum likelihood algorithms are also used for transmission tomography [61].

For simplicity, assume that the random error in each measurement is independent of the other measurements. The noisy data are drawn from a Poisson distribution,

$$\tilde{\mathbf{g}} \sim \text{Poisson}(\mathbf{g} + \mathbf{g}_0)$$

where $\text{Poisson}(\mathbf{v})$ is a vector of independent Poisson realizations with mean values given by the vector \mathbf{v} . The vector \mathbf{g}_0 is a background term, which is included for the experimental demonstrations in Chapters 3 and 4 since $\mathbf{g}_0 = 0$ is difficult to achieve experimentally. For simplicity, in the following derivation $\mathbf{g}_0 = 0$ but this term is restored later for the appropriate derivations.

One may write the log-likelihood L in terms of a product of Poisson distributions for each measurement:

$$\begin{aligned} L &= \ln \prod_{i=1}^M \frac{g_i^{\tilde{g}_i} e^{-g_i}}{\tilde{g}_i!} \\ &= \sum_{i=1}^M [\tilde{g}_i \ln g_i - g_i - \ln \tilde{g}_i!] \end{aligned} \quad (1.7)$$

The function of any maximum likelihood algorithm is to maximize L with respect to the estimated object \mathbf{f} . This should occur where the gradient vanishes:

$$\begin{aligned} \frac{\partial L}{\partial f_j} &= \sum_{i=1}^M \frac{\partial g_i}{\partial f_j} \left(\frac{\tilde{g}_i}{g_i} - 1 \right) \\ &= 0 \end{aligned} \quad (1.8)$$

The derivatives $\frac{\partial g_i}{\partial f_j}$ are precisely the components of the forward matrix \mathbf{H} . In the case of a nonlinear forward model, \mathbf{H} should be updated along with \mathbf{g} at each iteration. In vector form, equation (1.8) implies that

$$\frac{\mathbf{H}^T (\tilde{\mathbf{g}}./\mathbf{g})}{\mathbf{H}^T \mathbf{1}} = \mathbf{1}$$

where $\tilde{\mathbf{g}}./\mathbf{g}$ is an element-wise division and $\mathbb{1}$ is a vector of ones the same size as \mathbf{g} . Since the expression on the left is the identity, the object \mathbf{f} is a fixed point of the function $\mathcal{F}(\mathbf{f}) = \mathbf{f}.*\frac{\mathbf{H}^T(\tilde{\mathbf{g}}./\mathbf{g})}{\mathbf{H}^T\mathbb{1}}$, where $.*$ is an element-wise multiplication. This suggests the fixed point iteration

$$\mathbf{f}_{k+1} = \mathbf{f}_k.*\frac{\mathbf{H}^T(\tilde{\mathbf{g}}./\mathbf{g}_k)}{\mathbf{H}^T\mathbb{1}}, \quad (1.9)$$

recalling that $\tilde{\mathbf{g}}$ (and \mathbf{H} in the nonlinear case) is a function of \mathbf{f}_k . The estimate \mathbf{f}_{k+1} at the $(k+1)^{\text{st}}$ iteration is obtained by inserting the estimate \mathbf{f}_k at iteration k into the right hand side of (1.9) and computing \mathbf{g}_k from the forward model (1.6). Equation (1.9) is the basic update equation for Poisson MLE, and is used throughout this work with some modifications where appropriate. For the experiments that follow, \mathbf{f} was initialized with a constant value.

1.6 Singular value analysis

The coded aperture transmittance, along with the physics of the scattering and propagation, are embedded in the transformation H for a given measurement system. In general, H is not invertible, or its inverse is not easily obtained. However, depending on the structure of the forward model (and in turn the structure of the coded aperture), one can learn a great deal about the object F even if it cannot be uniquely determined. The properties of H determine which structures of F are measured most accurately.

The singular value decomposition (SVD) may be performed for any linear operator over continuous or discrete domains and provides a powerful tool for comparing measurement systems. Reference [4] discusses SVD analysis for computational imaging and related reconstruction methods, such as truncated SVD and Tikhonov regularization. The basic concept for system analysis is that measurement noise produces an effective singular value cutoff below which the singular vectors, and thus F , are not reliably recovered.

The SVD of the linear operator H is guaranteed to exist and consists of two orthonormal bases in the object and measurements spaces, $\{V_k(\mathbf{x})\}$ and $\{U_k(\mathbf{x}')\}$, and the singular values

$\{S_k\}$, where $k = 1 \dots N_s$ is an index. The continuous form of the SVD is written as

$$G(\mathbf{x}') = \sum_{k=1}^{N_s} U_k(\mathbf{x}') S_k F_k \quad (1.10)$$

where $F_k = \int d\mathbf{x} V_k(\mathbf{x}) F(\mathbf{x})$ is the projection of $F(\mathbf{x})$ onto the basis function $V_k(\mathbf{x})$, a “right singular vector”. The functions U_k are the “left singular vectors”. The singular value S_k is the amplitude for which the singular vector $V_k(\mathbf{x})$ is represented in the measurements. If $S_k = 0$ for some k , then the corresponding $V_k(\mathbf{x})$ is a vector in the null space of H and is never measured. In the presence of noise, $G(\mathbf{x}')$ is the mean of a random field and vectors with small S_k may not be reliably recovered. Singular value analysis is therefore a critical step in design of any linear measurement system.

The discrete version of the SVD is the matrix factorization $\mathbf{H} = \mathbf{U}\mathbf{S}\mathbf{V}^\dagger$, where \mathbf{U} and \mathbf{V} are unitary matrices and \mathbf{S} is diagonal with entries given by the singular values S_k . The operator \dagger is the matrix adjoint, or “conjugate transpose”. The left singular vectors are the columns of \mathbf{U} and the right singular vectors are the columns of \mathbf{V} . Specifically, the components of \mathbf{U} and \mathbf{V} are

$$\begin{aligned} U_{ik} &= \int d\mathbf{x}' \Phi_i(\mathbf{x}') U_k(\mathbf{x}') \\ V_{jk} &= \int d\mathbf{x} \Psi_j(\mathbf{x}) V_k(\mathbf{x}) \end{aligned}$$

where $i = 1 \dots M$ indexes the measurements, $j = 1 \dots N$ indexes the object coefficients, and $k = 1 \dots N_s$ indexes the singular values. Here, the functions $\{\Phi_i\}$ and $\{\Psi_j\}$ are the measurement and object bases of Section 1.4.

In Chapter 2, singular values are computed for pencil and fan beam CAXSI systems and used to compare different choices for coded apertures. Also, singular values for CAXSI are compared with those of SVT and the Radon transform (as used in CT), with the conclusion that CAXSI promises an advantage for situations where the radiation dose to the object is

limited. Chapter 6 presents singular value analysis for energy sensitive measurements using a pencil beam, showing the dependence on the energy resolution and choice of coded aperture.

CHAPTER 2: CODED APERTURES FOR X-RAY SCATTER IMAGING

(Adapted from previously published work [33])

2.1 Background

The focus of this chapter is a theoretical analysis of tomography based on coded aperture x-ray scatter imaging (CAXSI). Pencil and fan beam geometries are studied here, and singular value decomposition (SVD) is used to compare coded aperture designs, and also to compare each CAXSI system with other tomographic strategies such as Radon imaging and selected volume tomography (SVT). Scatter imaging commonly relies on SVT using collimation filters at the source and at the detector [2]. CAXSI is a novel approach to scatter imaging that uses coded masks between the scattering object and the detector array.

In the following, pencil beam CAXSI is shown to enable 1D tomography from a snapshot measurement (a single exposure of a detector array) by detecting a diversity of scattered x-rays. Later in this chapter, these ideas are applied to fan beam CAXSI, suggesting a new coded aperture design for planar snapshot imaging. The first experimental demonstration of pencil beam CAXSI is presented in Chapter 3, and its success inspired the experimental fan beam CAXSI system of Chapter 4.

Singular value analysis is often used to evaluate the noise sensitivity of measurement systems and to quantify the number of components measured above the noise floor. SVD analysis is presented in Section 2.5 which finds that the singular values for CAXSI decay more slowly compared with other techniques as the image resolution is increased. This suggests possible improvements in dose requirements and/or signal to noise ratio for CAXSI systems.

The system geometry for forward scatter CAXSI is illustrated in Figure 2.1.

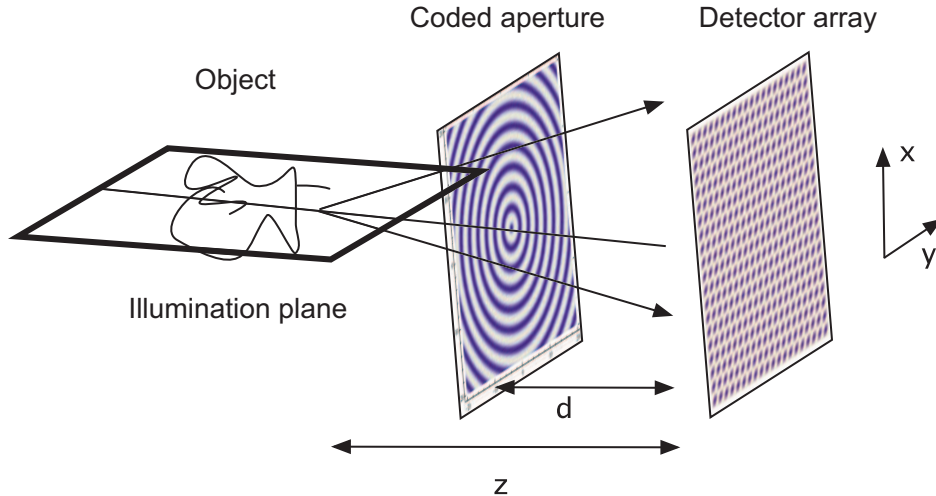


Figure 2.1: System geometry for planar scatter imaging

Scattered radiation from the illuminated object passes through a coded aperture placed a distance d in front of a 2D detector array. In contrast with collimation filters, the coded aperture allows rays from multiple directions to simultaneously illuminate each detector pixel. Increased photon efficiency is the advantage of CAXSI relative to selected volume imaging. CAXSI owes its throughput and snapshot advantages to coded apertures with high average transmittance (50%), a number of which are presented here for pencil and fan beams, and in Chapter 5 for cone beam illumination.

Shift codes are well known in coded aperture imaging and provide resolution parallel to a detector array. The shift codes used here are based on quadratic residues. A novel result of this work is sinusoid functions used as scale codes due to their distinguishability under magnification, providing resolution in range from a detector plane. These sinusoid apertures are precursors to the more general “frequency scale codes” of Chapter 5.

Linear scattering models are analyzed which are applicable when attenuation is negligible or otherwise corrected for. The linear form of these forward models enables evaluation of the SVD. Analytic SVDs are derived for isotropic scattering objects and numerical SVDs are evaluated for the anisotropic cases. The next section analyzes pencil beam CAXSI under the assumption of isotropic scattering. This is extended to anisotropic scattering and applicable

coded aperture designs are presented in Section 2.3. A new coded aperture for fan beam illumination and isotropic scattering is presented in Section 2.4, and the scalability of CAXSI is compared with other tomographic strategies in Section 2.5. Results from this chapter are summarized in Section 2.6.

2.2 Pencil beam CAXSI

As a first example of code design, suppose that a pencil beam illuminates a section of the target object distributed along the z axis. Our goal is to image the object's scattering density $F(x = 0, y = 0, z)$, or simply $F(z)$. The full volume may subsequently be reconstructed by raster scanning.

Assume isotropic scatter to all detector positions, which approximates Compton (incoherent) scattering or x-ray fluorescence when attenuation is weak and the detector array subtends a small solid angle with respect to the object (this last assumption will be relaxed in Section 2.3). The detector elements lie in the $z = 0$ plane and measure the scatter. The scatter visibility is modulated by a coded aperture a distance d from the detector plane. For simplicity, we assume a 1D coded aperture transmittance $T(x)$, where x may be a Cartesian coordinate or a radius from the pencil beam axis. The signal at coordinate x in the detector plane is

$$G(x) = \int_d^{z_{\max}} F(z)T \left[x \left(1 - \frac{d}{z} \right) \right] dz. \quad (2.1)$$

For simplicity, the system geometric response is omitted and the source is monochromatic. Estimation of $F(z)$ from $G(x)$ is enabled by judicious selection of $T(x)$.

The coordinate transformation $\beta = 1 - d/z$ changes (2.1) to

$$M(x) = \int_0^1 \tilde{F}(\beta)t(x\beta)d\beta, \quad (2.2)$$

where $\tilde{F}(\beta) = F(z = d/(1 - \beta))d/(1 - \beta)^2$ and we assume $z_{\max} \gg d$. Equation (2.2) is a “scale transformation”; inversion is straightforward if $T(x)$ is orthogonal in scale.

Sinusoid functions are orthogonal in scale, since sinusoids at different frequencies have

vanishing correlation. The simplest choice for $T(x)$ satisfying the requirements that $0 \leq T \leq 1$ is $T(x) = [1 - \cos(2\pi ux)]/2$, where u is the spatial frequency of the coded aperture. The measurement model is then

$$G(x) = \frac{1}{2} \int_0^1 \tilde{F}(\beta) [1 - \cos(2\pi ux\beta)] d\beta. \quad (2.3)$$

Equation (2.3) is familiar as the forward model for the Fourier transform spectroscopy [4]. The singular vectors for this transformation are derived from the constant singular vector associated with the 1 operator and prolate spheroidal singular vectors associated with the kernel $\cos(2\pi ux\beta)$. Assuming that the support of $G(x)$ is $[0, D]$, the singular value corresponding to the first operator is $N_x = uD$, which is the number of sinusoid periods that are observed for a scatter point at ∞ .

The singular vectors of the operator $-(1/2)\cos 2\pi ux\beta$ supported over $\beta \in [0, 1]$ and $x \in [0, X]$ are the prolate spheroidal wavefunctions $\psi_n(\beta)$ for n even [62]. The corresponding singular values are $\sqrt{\lambda_n N_x}/2$, where $\lambda_n \approx 1$ for $n < N_x/2$ and $\lambda_n \approx 0$ for $n > N_x/2$ [4].

The even prolate spheroidal functions are not orthogonal to the constant vector over $[0, 1]$ but the much larger singular value associated with the constant vector means that the spaces spanned by the two operators approximate the space spanned by their sum. The singular decomposition space thus consists of a single vector with singular value $N_x/2$ and $N_x/2 - 1$ secondary vectors corresponding to singular values $\sqrt{N_x}/2$.

The prolate spheroidal basis yields resolution elements of length $1/N_x$ distributed uniformly distributed over $\beta = [0, 1]$. Converting back to the z coordinate, one derives resolution

$$\Delta z = \frac{z^2}{N_x d}. \quad (2.4)$$

This expression may be understood by noting that the location z of a single point scatterer is localized by observing \bar{u} , the frequency of the sinusoid projected onto the detector. The aperture code is magnified by a factor $z/(z - d)$ and so $\bar{u} = u(z - d)/z$. The signals from

two point scatters separated by a distance Δz lose orthogonality when $\Delta \bar{u} \leq 1/X$ due to the finite detector size X . Propagating this uncertainty to z through $\Delta \bar{u} = \frac{\partial \bar{u}}{\partial z} \Delta z$ produces equation (2.4).

2.3 Anisotropic scattering

In the previous section, sinusoidal codes were shown to provide range discrimination under isotropic scattering. If a 2D detector is used, there is a redundancy of scattered rays which may be exploited to estimate features other than density along the 1D object. In this section we present such an example where a more general scattering model relaxes the assumption of isotropic scattering to allow dependence on θ , the polar scattering angle. This applies, for instance, to coherent scattering from liquids, powders, and amorphous compounds. In this case one may vary the code $T(\varphi, \rho)$ as a function of angle φ and radius ρ in order to image θ and z simultaneously. The forward model in this case is

$$T(\varphi, \rho) = \int_d^{z_{\max}} F(z, \theta) T \left[\varphi, \rho \left(1 - \frac{d}{z} \right) \right] dz \quad (2.5)$$

with polar angle φ and radius ρ in the detector plane. Let $r = \rho \left(1 - \frac{d}{z} \right)$ be the radius at which the ray connecting beam position z with detector radius ρ intersects the aperture plane. Transforming the integral in equation (2.5) from z to r , and defining $\tilde{F}(r, \rho) = \frac{\rho d}{(\rho - r)^2} F \left(z = \rho d / (\rho - r), \theta = \tan^{-1} \frac{\rho - r}{d} \right)$, the forward model takes the simple form

$$G(\varphi, \rho) = \int T(\varphi, r) \tilde{F}(r, \rho) dr. \quad (2.6)$$

Each radius therefore defines a subspace for the operator $\int T(\varphi, r)(\dots)dr$ and its matrix representation \mathbf{T} . The elements of the discrete forward operator \mathbf{T} are $H_{ij} = T(i\Delta\varphi, j\Delta r)$, given by samples of the transmittance at regular intervals in φ and r . Because \mathbf{T} operates on subspaces, the singular values of (2.6) are equal to those of \mathbf{T} . However, the transformation from $F(z, \theta) \rightarrow \tilde{F}(r, \rho)$ is not unitary and therefore the SVD of (2.5) is more complicated,

motivating numerical evaluation.

We seek invertible codes for \mathbf{T} with entries in $[0, 1]$. The simplest coded aperture is based on the identity matrix, shown in polar and Cartesian coordinates in Figure 2.2. This aperture is a type of collimator since each detector receives a single ray, and therefore provides minimal throughput. Multiplexing with 50% average transmittance can be achieved by a coded aperture based on a discrete cosine transform (DCT), shown in Figure 2.3. This mask contains grayscale values, but some applications require binary codes due to fabrication limitations. This motivates codes based on a Hadamard matrix (Figure 2.4) or randomized features (Figure 2.5). A high resolution Cartesian image of the DCT code is included which shows its continuous form, and the columns of the Hadamard matrix have been sorted so the angular frequency increases with radius. This sorting operation is unitary and therefore preserves the singular value spectrum.

For each of the apertures in Figures 2.2-2.5, the forward model (2.5) was numerically evaluated as a matrix in order to find its singular value spectrum. The object was sampled with 48×48 pixels from $z = d$ to $2d$ and $\theta = 0$ to 27° . Each coded aperture was simulated at $d = 100$ mm with 31 polar sections and 31 radial sections from $r = 0$ to 25 mm. The detector was sampled with 96 polar and 96 radial sections from $\rho = 0$ to 50 mm. The singular value spectra for these code choices are plotted together in Figure 2.6, and this plot includes the sinusoid code $T(x)$ which was previously derived for isotropic scattering, labeled “Harmonic in x ”. The identity code shows the poorest performance, due to its low overall transmission. The sinusoid and DCT codes show significantly larger values and follow each other closely. The Hadamard and random binary codes have the largest singular values and choosing between these two depends on the noise floor and which singular vectors should be emphasized.

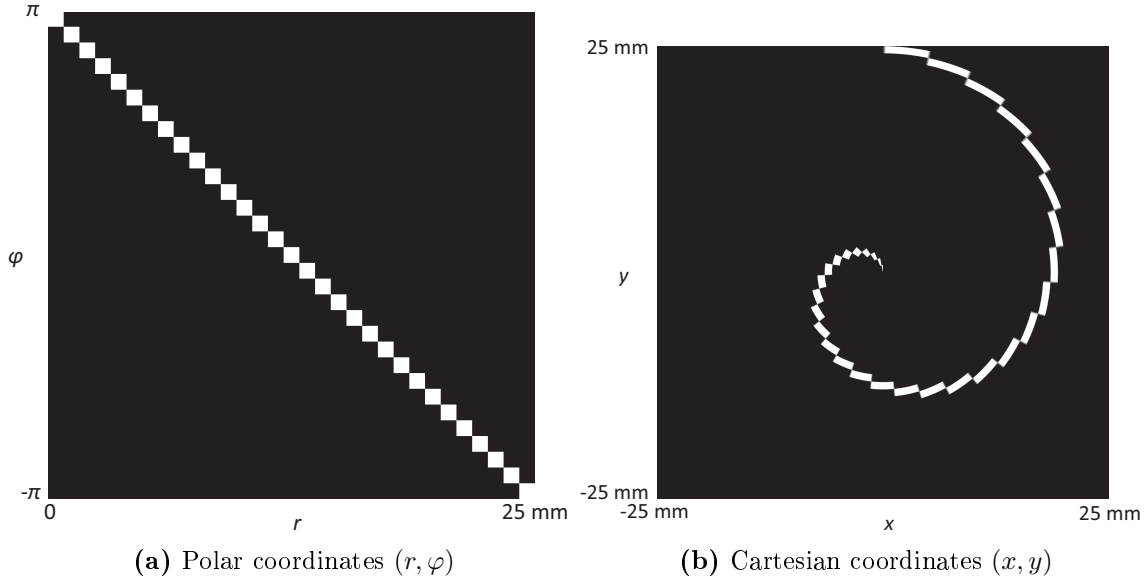


Figure 2.2: Coded aperture based on the identity matrix

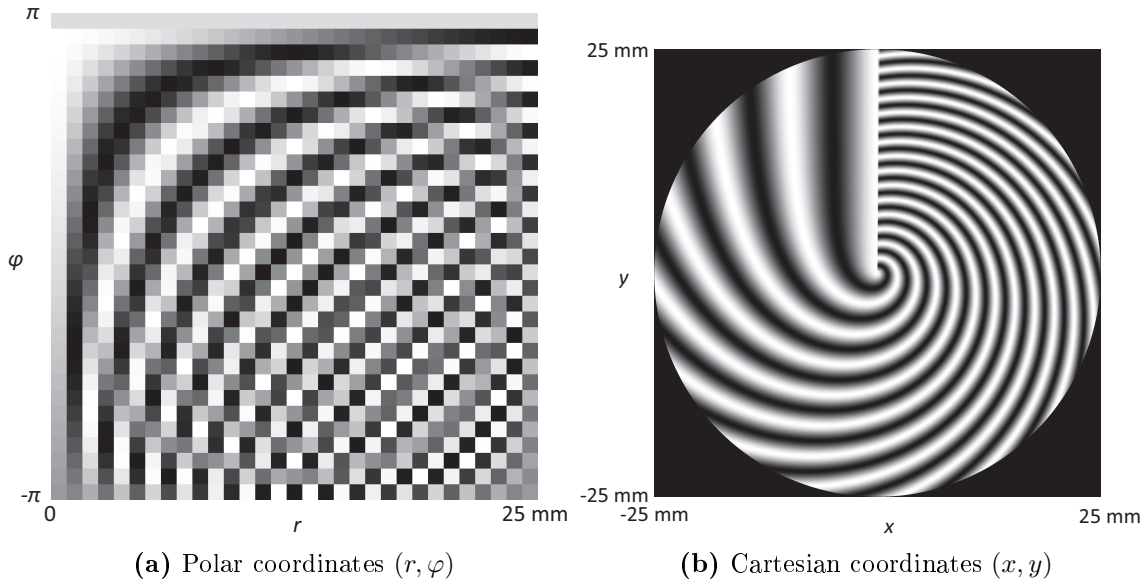


Figure 2.3: Coded aperture based on the discrete cosine transform (DCT)

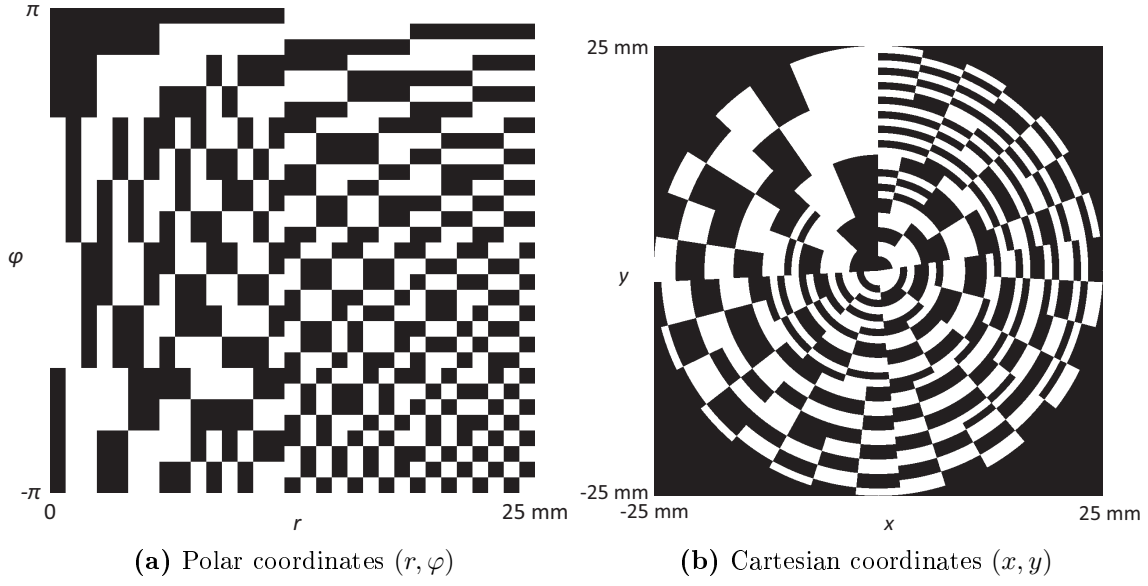


Figure 2.4: Coded aperture based on a Hadamard matrix

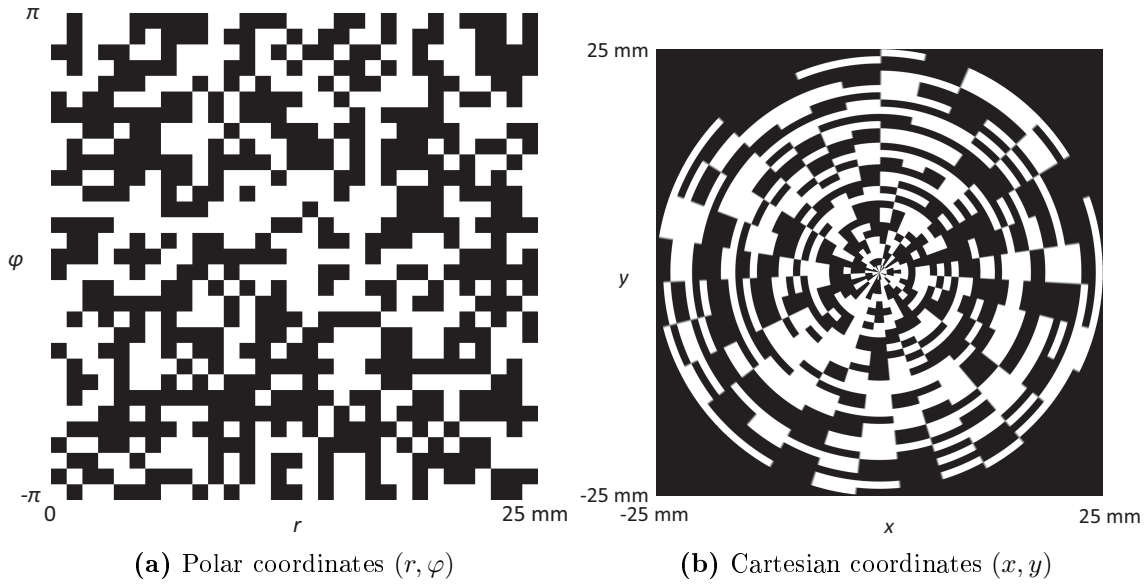


Figure 2.5: Coded aperture based on a random binary matrix

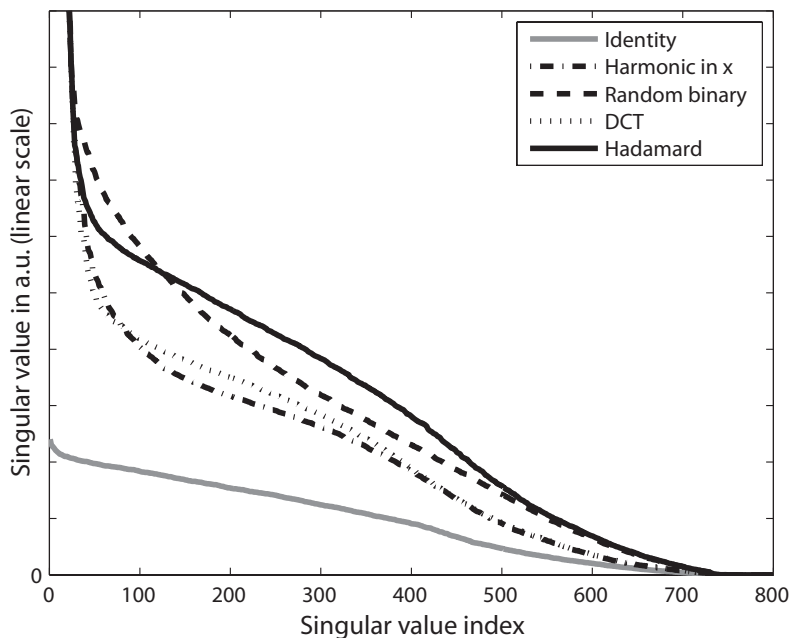


Figure 2.6: Singular value spectra of the pencil beam system for each code choice

2.4 Fan beam CAXSI

CAXSI may also be applied to planar imaging. Once again, consider isotropic scattering for simplicity. When the entire yz plane is illuminated as in Figure 2.1, the forward model becomes

$$G(x, y) = \int_{-Y/2}^{Y/2} \int_d^{z_{max}} F(x' = 0, y', z') \times T \left[x \left(1 - \frac{d}{z'} \right), y \left(1 - \frac{d}{z'} \right) + y' \frac{d}{z'} \right] dy' dz'. \quad (2.7)$$

Choosing

$$T(x, y) = \frac{1 + \sin(2\pi ux)p(\nu y)}{2}, \quad (2.8)$$

where $p(\nu y)$ is described below, provides sensitivity to shifts in y and z . The quantity ν is the spatial frequency of the code in the y direction. Specifically,

$$p(y) = \sum_n p_n [2 \text{rect}(y - n) - 1],$$

where $\text{rect}(y)$ is a unit square pulse of width 1 and $\{p_n\}$ is a binary sequence with two-level auto-correlation. Such sequences may be found for various code lengths [63]. Quadratic residue derived codes of length $P = 4m + 1$, with P prime, are particularly straightforward, and yield transverse imaging resolution $\Delta y = z/(\nu d)$ [56]. Two scatter points separated by Δy produce signals shifted by one code period in the y direction, which sufficient for distinguishability.

Figure 2.7 shows new aperture designs that have sinusoidal dependence on the horizontal (x) axis and a shift code in the vertical (y) axis using a quadratic residue code. The aperture resolution (number of code features) was varied separately in each direction to illustrate the scaling of the singular value spectrum, shown in Figure 2.8. Measurements were numerically simulated over a 100 mm \times 100 mm area and 96 \times 96 samples. The object was represented by 48 \times 48 pixels over a square region of dimension 100 mm in the yz plane, centered 150 mm from the detector. The coded aperture was simulated at distance 100 mm from the detector and tiled to provide full coverage on the detector from all scatter points.

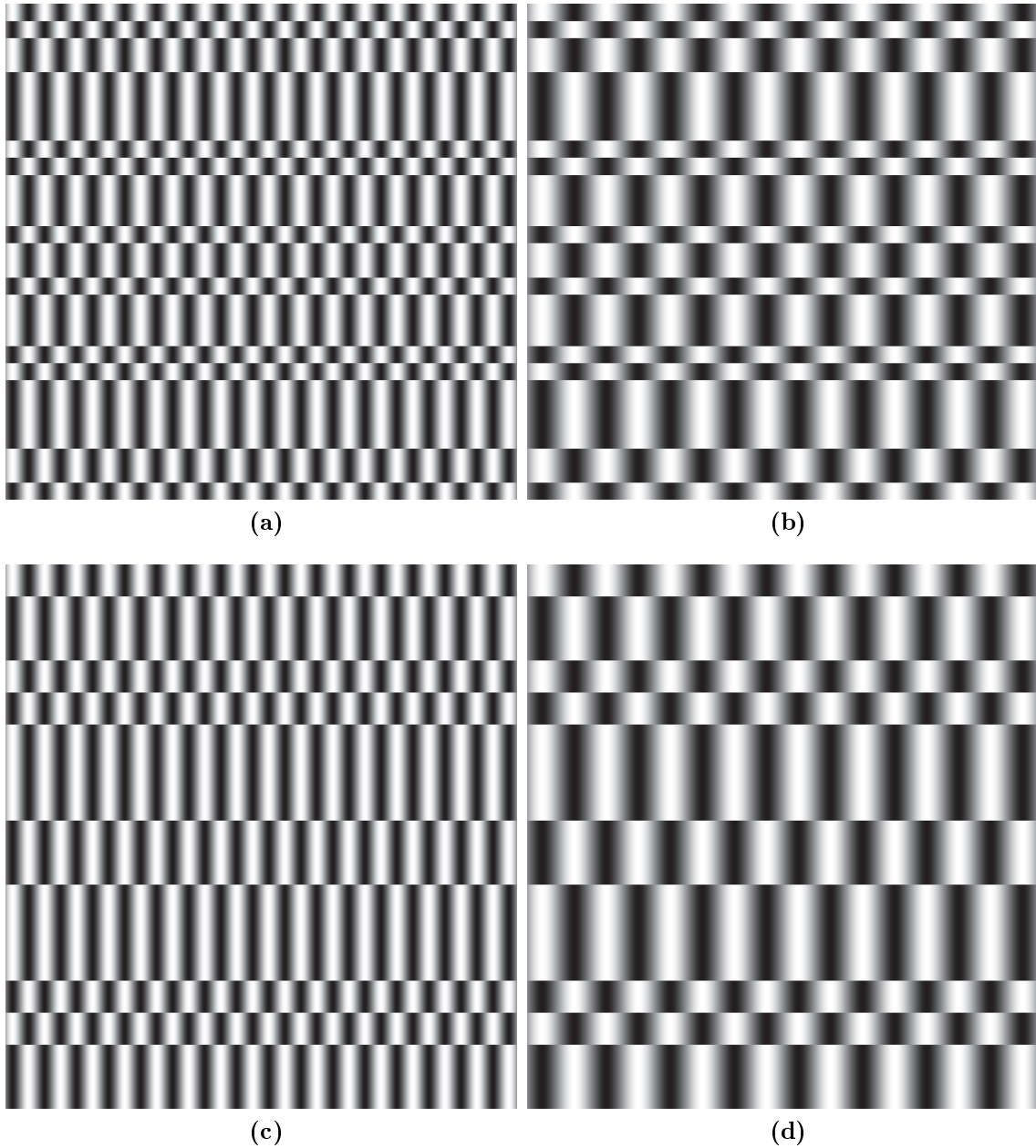


Figure 2.7: Coded apertures based on a sinusoid in x (horizontal) and a quadratic residue in y (vertical). The number of code features in each direction (x, y) are (a) 32×29 , (b) 16×29 , (c) 32×17 , and (d) 16×17 features.

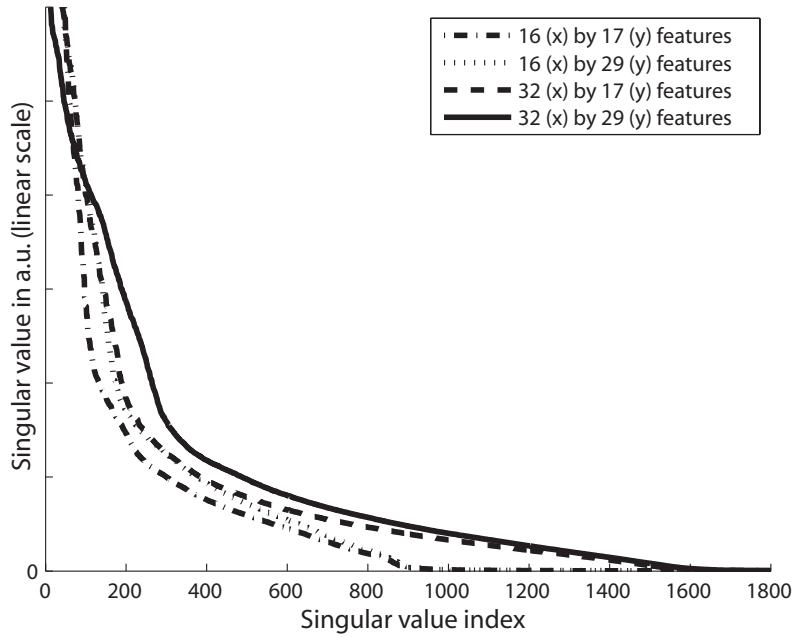


Figure 2.8: Singular value spectra for each of the coded apertures in Fig. 2.7.

A look at the singular value spectra in Figure 2.8 reveals the effect of code resolution. The codes with 16 features (8 sinusoid periods) in the x direction both cutoff at about 900 singular values, and the codes with 32 features in x retain about 1600 singular values. Increasing the shift code resolution from 17 to 29 features amplifies the singular values but does not appear to add more. Increasing the frequency of the harmonic code has the strongest effect of adding singular values and amplifying the spectrum.

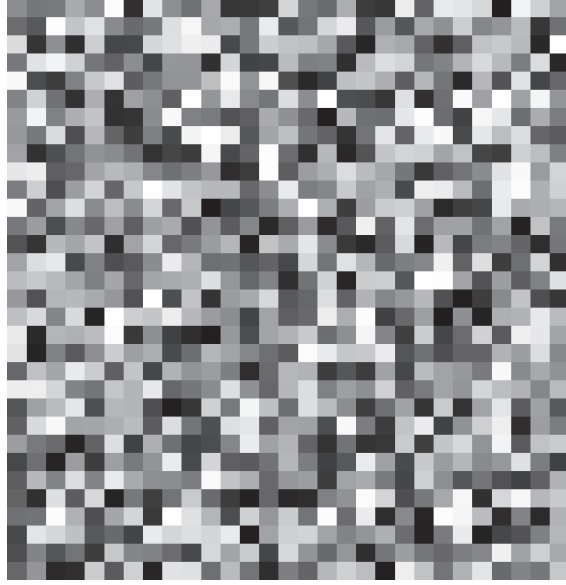


Figure 2.9: Coded aperture with resolution 32×29 based on uniform random values in $[0, 1]$.

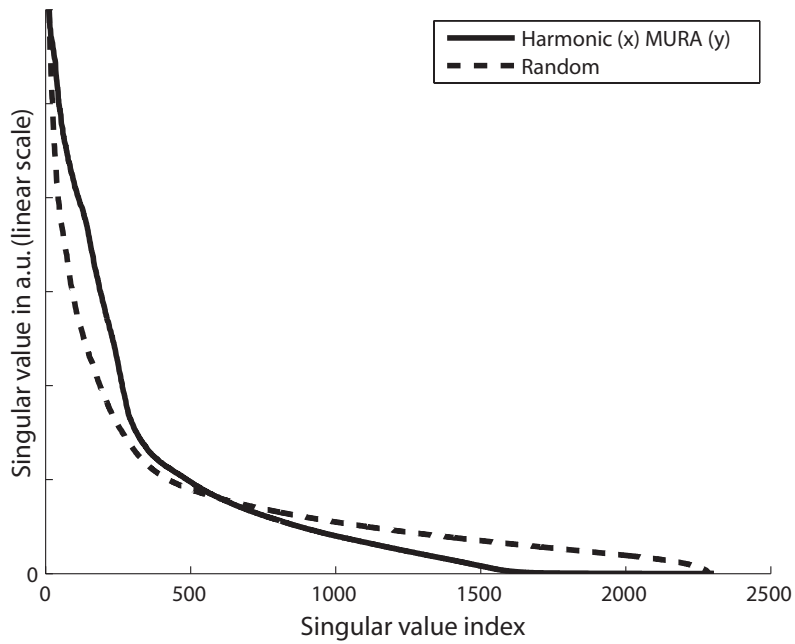


Figure 2.10: Singular value spectra for the proposed code and a random code.

The coded aperture with 32×29 features was compared with a similar random code drawn from a uniform distribution on $[0, 1]$ shown in Figure 2.9. The singular value spectra for the

CAXSI systems using the two codes are shown in Figure 2.10. For the first 620 singular values the new “Harmonic-MURA” code outperforms the random code but then a crossover occurs and the random code produces a more slowly decaying spectrum. One can expect that the random aperture will perform worse in a noisy environment where a limited number of singular vectors are measurable.

2.5 Scalability of imaging techniques

This section compares CAXSI with Radon imaging and selected volume tomography (SVT) for 2D tomography under the constraint of fixed radiation dose delivered to the object. The singular values for each technique scale with the resolution of the desired image, where it is assumed the number of measurements M equals the number of object coefficients. Radon imaging is a method of transmission tomography where the measurements are line integrals of the target’s density. Radon imaging requires multiple exposures for each tomographic image. The singular values of the 2D Radon transform are $\lambda_m = \sqrt{4\pi/(m+1)}$ [64], with each value having a degeneracy of $m+1$. The Radon transform therefore yields typical singular values proportional to $1/M^{1/4}$. Letting N be the number of reconstructed pixels in each object dimension, $M = N^2$ so the singular values are of magnitude $1/\sqrt{N}$. A pencil beam scanned over a plane produces N subspaces each with N singular values proportional to $1/\sqrt{N}$. For the Radon system to deliver the same dose as the scanned pencil beam, the source must be N times dimmer during Radon’s N exposures. The effective scaling is then $1/N^{3/2}$ for Radon and $1/\sqrt{N}$ for pencil beam CAXSI. Appendix B shows that the singular values scale like $1/N$ for fan beam CAXSI, and since this is a snapshot technique the dose is comparable to the scanned pencil beam.

Selected volume tomography (SVT) is a scatter imaging technique which uses collimation at the source and detector so that each measurement is sensitive to a single object voxel [2]. Using an array of detectors collimated appropriately, snapshot measurement is possible using SVT. The measurement matrix for SVT is diagonal and the elements are the singular values. For a fixed dose, the singular values are proportional to $1/N$ for a pencil beam and $1/N^2$ for

a fan beam since these are the fractions of the total number of voxels contributing to each measurement.

Table 2.1 summarizes the scaling laws for 1D and 2D imaging using pencil and fan beam CAXSI, Radon imaging, and SVT. In each case the singular values are scaled so the maximum singular value corresponding to the constant singular vector is 1. Both pencil and fan beam CAXSI show improvement over other methods for 1D and 2D imaging. In addition, pencil beam CAXSI enables independent reconstruction of each ray, whereas planar Radon imaging multiplexes points over a plane. Independent reconstruction of each 1D subspace using pencil beam CAXSI enables spot tomography, where a single pencil beam illuminates a region of interest, eliminating unnecessary doses to neighboring regions.

Image dimension	Pencil	Fan	Radon	SVT
1D	$\frac{1}{\sqrt{N}}$	-	-	$\frac{1}{N}$
2D	$\frac{1}{\sqrt{N}}$	$\frac{1}{N}$	$\frac{1}{N^{3/2}}$	$\frac{1}{N^2}$

Table 2.1: Scaling of dose-constrained singular values for pencil beam CAXSI, fan beam CAXSI, Radon imaging, and selected volume tomography (SVT). In each case the singular values are scaled so that the maximum is 1.

These results assume equal photon efficiency for scatter and transmission imaging. In practice, the scatter systems will include an additional factor for the fraction of the total scatter signal detected, and the ratio of scattered to transmitted photons for the object of interest. These effects should be studied carefully for particular imaging applications.

2.6 Summary

This chapter analyzed CAXSI techniques employing pencil and fan beam illumination. By using specially-designed coded apertures, 1D and 2D density distributions can be reconstructed from a single exposure of an appropriate imaging detector. Sinusoid codes are shown to provide range resolution under the assumption of isotropic scattering, an approximation for x-ray fluorescence and Compton (incoherent) scattering. These will be examined again in the context of cone beam scatter tomography in Chapter 5. Two dimensional codes were

developed for anisotropic scattering along a pencil beam, applicable to Bragg scattering from liquids, powders, and amorphous compounds. For each system, singular value analysis of the first-order scattering model was presented, which was compared with Radon imaging and SVT under a fixed dose constraint. CAXSI shows several advantages, including improved scalability, snapshot capability, and the prospect of "spot tomography" where isolated regions of interest are irradiated. Further refinement of the scattering models could involve energy-dependent absorption and multiple scattering effects. Based on the lesson learned here, the next two chapters present experimental demonstrations of pencil and fan beam CAXSI.

CHAPTER 3: PENCIL BEAM CAXSI

(Adapted from previously published work [31])

3.1 Background

This chapter describes a pencil beam x-ray system demonstrating coded aperture x-ray scatter imaging (CAXSI). In the previous chapter, sinusoid codes were shown to provide range resolution for pencil beam tomography. These ideas inspired the following experiment which demonstrates snapshot 1D tomography using a periodic coded aperture, while also measuring the coherent scattering density of the object at each point in the beam. In the language of Chapter 1, this corresponds to the transformation $F(z, q) \rightarrow G(x, y)$, where F is the unknown scattering density and $G(x, y)$ is the measured irradiance image. This is closely related to the anisotropic system $F(z, \theta) \rightarrow G(x, y)$ from the last chapter, and would be identical to it for the case of a purely monochromatic beam. In the following, coherent scatter imaging is achieved with angle dispersive measurements and a poly-energetic x-ray source.

X-ray scatter imaging has shown promise for a wide variety of applications, including detection of abnormal structures in biological tissue [27–29], measurements of surface structure [65], and detection of explosives and other controlled substances [23, 66, 67]. Reference [10] gives an overview of x-ray scatter imaging for explosives detection and shows reconstructions of buried landmines using Compton back-scatter imaging, as well as reconstructions of various plastics (nylon, PMMA, PE, PTFE, PVC) using coherent scatter computed tomography (CSCT). CSCT [26] has been applied to bone mineral density measurements [27] and detection of urinary stones [29]. In addition, reference [30] demonstrates a fan beam energy-dispersive CSCT system which can detect various plastics in an aluminum case.

CSCT uses a series of images recorded at multiple angles to estimate an object’s coherent scatter properties. Another approach to scatter tomography is energy-dispersive x-ray diffraction tomography (EXDT) [68], which scans an object voxel-by-voxel using collimators and provides an effectively isomorphic mapping between the object voxels and the measurements. EXDT was originally demonstrated with an x-ray tube and then with a synchrotron source [69]. It has been used to probe polymer and bone surfaces [65], to reduce the false alarm rate of luggage scanners in airline security [23], and to probe mineral content in thick cement samples [24].

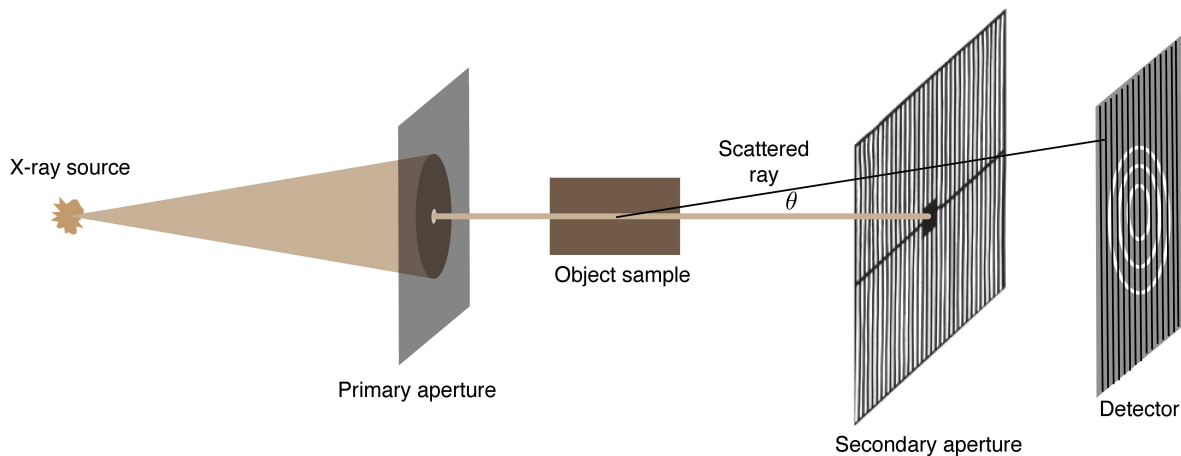


Figure 3.1: Basic pencil beam coded aperture x-ray tomography system.

The goal of this chapter is to experimentally demonstrate pencil beam CAXSI by recovering the momentum transfer profile of a scattering object at each point along the beam using a single irradiance image. The experimental system is depicted in Figure 3.1, including a 2D irradiance detector array perpendicular to the beam and a coded aperture between the object and detector to modulate the scattered radiation. To obtain a volumetric scatter image, the pencil beam could be scanned over a 3D object with estimation performed for each transverse position.

The following section develops a measurement model for the pencil beam CAXSI system. Section 3.3 describes the experimental setup, followed by reconstruction techniques in Section 3.4, and a discussion of the experimental results in Section 3.5.

3.2 Forward model

In the pencil beam system depicted in Figure 3.1 the x-ray source is filtered by a pinhole to produce a pencil beam propagating along the z axis, which for simplicity is assumed infinitely narrow. The scattering object is placed between the primary and secondary apertures so that it is penetrated by the beam. The primary beam is stopped by the secondary mask to prevent it from flooding the detector image. Scattered x-rays diverge from the main beam to strike the aperture, where they are either absorbed or transmitted to the detector plane. Each pixel in the detector array receives scattered power from multiple points along the beam, and the structure of this multiplexing is controlled by the aperture code.

As discussed in Section 1.2.1 of Chapter 1, upon coherent scattering an x-ray photon changes its momentum by $\mathbf{q} = \mathbf{p}_f - \mathbf{p}_i$, where \mathbf{p}_i is the incident momentum and \mathbf{p}_f is the final momentum. The coherent scattering condition is $|\mathbf{p}_f| = |\mathbf{p}_i|$, from which follows Bragg's law $q = \frac{2E}{c} \sin\left(\frac{\theta}{2}\right)$, where $q = |\mathbf{q}|$, E is the x-ray energy, and θ is the scattering angle as shown in Figure 3.1.

The scattering density $F(z, q)$ is the probability that an incident photon scatters at beam location z with momentum transfer q . This model only depends on the magnitude of the momentum transfer and not its direction, so it applies to liquids, fine powders (as in this experiment), and amorphous compounds. In the absence of a coded aperture, scattering at angle θ from position z produces an irradiance at radius ρ on the detector proportional to $1/(z^2 + \rho^2)$. The coded aperture is modeled by the transmission function $T(\rho, \phi)$ in the plane $z = d$, where (ρ, ϕ) are the polar radius and angle relative to the beam. To within some proportionality constant, the total irradiance at the detector point (ρ, ϕ) is

$$G(\rho, \phi) = \int dz \left(\frac{1}{z^2 + \rho^2} \right) T\left(\rho \left[1 - \frac{d}{z}\right], \phi\right) \int dq F(z, q) P\left(E = \frac{zqc}{\rho}\right), \quad (3.1)$$

where c is the speed of light and we assume small scattering angles so $\sin(\theta/2) \approx \rho/(2z)$.

$P(E)$ is the power spectral density of the beam, assumed independent of z so that the linear model applies. Equation (3.1) is the “forward model” for this pencil beam system, and consists of integrals of the scattering density over z and q . The argument $\rho(1 - d/z)$ to the aperture transmittance T is the intersecting radius for the scattered ray connecting scatter point z and measurement radius ρ in the detector plane

In contrast with previous studies of coded aperture imaging that emphasize “shift codes” based on their properties under translation [56], range imaging requires “scale codes” that are maximally distinguishable under magnification. As discussed in Chapter 2, equation (3.1) is a scale transformation of the aperture code $T(\rho, \phi)$ which depends on the scatter position z . The projected image of the aperture code is magnified by $z/(z - d)$. One can disambiguate scatter points at different values of z by applying aperture codes which are orthogonal under changes in scale (i. e. magnification). Sinusoid codes (e.g. $T(\rho) = \cos(\rho)$) have this property. To also disambiguate q the code must also vary as a function of ϕ . As binary codes are easily manufactured, we chose the square grid

$$T(\rho, \phi) = \frac{1 + \text{sign}(\sin(ux))}{2}, \quad (3.2)$$

where u is the spatial frequency and x is a Cartesian coordinate in the ρ, ϕ plane. Equation (3.2) describes a binary version of the sinusoid, where the transmittance values lie between zero and one in accordance with incoherent imaging. An x-ray projection of the corresponding physical aperture is shown in Figure 3.3, which consisted of periodic slits drilled in to a lead plate. This x-ray projection image was used for T instead of (3.2) for better model accuracy.

The continuous forward model (3.1) is discretized by expanding the scattering density over compact voxel functions in the coordinates z and q . For this purpose we use the function $\text{rect}(x)$ which is equal to unity for $|x| < 1/2$ and zero everywhere else. The voxels are chosen with sampling rates Δz in z and Δq in q and have centers (z_j, q_j) .

With reference to Section 1.4 of Chapter 1, this corresponds to choosing the object basis

$\Psi_j(z, q) = \text{rect}\left(\frac{z-z_j}{\Delta z}\right) \text{rect}\left(\frac{q-q_j}{\Delta q}\right)$. The discrete model for the scattering density is

$$F(z, q) = \sum_j f_j \text{rect}\left(\frac{z-z_j}{\Delta z}\right) \text{rect}\left(\frac{q-q_j}{\Delta q}\right), \quad (3.3)$$

where f_j is a set of coefficients characterizing the object. The detector is artificially partitioned into polar sections indexed by i , corresponding to the measurement basis $\Phi_i(\rho, \phi) = \text{rect}\left(\frac{\rho-\rho_i}{\Delta\rho}\right) \text{rect}\left(\frac{\phi-\phi_i}{\Delta\phi}\right)$. The power measured in the section at polar coordinates (ρ_i, ϕ_i) and width $(\Delta\rho, \Delta\phi)$ in these coordinates is

$$g_i = \int \rho d\rho \text{rect}\left(\frac{\rho-\rho_i}{\Delta\rho}\right) \int d\phi \text{rect}\left(\frac{\phi-\phi_i}{\Delta\phi}\right) G(\rho, \phi), \quad (3.4)$$

taking care to consider the periodicity of ϕ . When equations (3.3) and (3.4) are used in equation (3.1), the discrete model is expressed as the linear system

$$\mathbf{g} = \mathbf{H}\mathbf{f}, \quad (3.5)$$

where \mathbf{g} and \mathbf{f} are vectors with components g_i and f_j , and \mathbf{H} is the ‘‘forward matrix’’. Noting that $\int dx \text{rect}(x)f(x) = \int_{-1/2}^{1/2} dx f(x)$, \mathbf{H} has components

$$H_{ij} = \int_{\rho_i-\frac{\Delta\rho}{2}}^{\rho_i+\frac{\Delta\rho}{2}} \rho d\rho \int_{\phi_i-\frac{\Delta\phi}{2}}^{\phi_i+\frac{\Delta\phi}{2}} d\phi \int_{z_j-\frac{\Delta z}{2}}^{z_j+\frac{\Delta z}{2}} dz \left(\frac{1}{z^2 + \rho^2}\right) \times T\left(\rho \left[1 - \frac{d}{z}\right], \phi\right) \int_{q_j-\frac{\Delta q}{2}}^{q_j+\frac{\Delta q}{2}} dq P\left(\frac{zqc}{\rho}\right).$$

The discrete forward model (3.5) can be used with numerical methods to estimate the object vector \mathbf{f} , given measurements \mathbf{g} and functional models for $P(E)$ and $T(\rho, \phi)$. The forward matrix \mathbf{H} for the experimental system was computed and used with a maximum likelihood algorithm derived from Reference [59] to reconstruct the underlying object vector \mathbf{f} for each object configuration (the procedure is described in detail in Section 3.4). The reconstructed objects are presented in Section 3.5, but first the experimental setup is described in the next

section.

3.3 Experimental methods

In order to build the pencil beam CAXSI experiment shown in Figure 3.1, a standard diagnostic x-ray system, which has been described in detail previously [70, 71], was modified to include an optical bench, a collimator, a coded aperture, and a sample stage at adjustable positions in the beam. The x-ray source used was a General Electric (GE) model MX100 that has a tungsten target with a 12° anode angle. The focal spot for this source was specified to be 0.6 mm full-width at half-max (FWHM). The acquisition mode was set at 116 kVp, 500 mAs. The source produced Bremsstrahlung radiation in the energy range 20-116 keV and also characteristic lines from tungsten's K_α transition doublet at 58.0-59.3 keV and from the K_β transitions at 66.7-67.7 keV. The x-ray beam had an inherent filtration equivalent to 1.1 mm thick aluminum (as measured at 80 kVp).

Since broadband illumination is expected to degrade chemical specificity in coherent scatter systems [72], spectral shaping is critical to angle dispersive measurements. Toward that end, the beam was shaped by a 0.1 mm thick tungsten filter which served as a band-pass between approximately 30 keV and tungsten's K-edge at 69.5 keV. The expected source spectrum was modeled using the semi-empirical x-ray spectrum modeling program XSPECT [73]. XSPECT produced a model for the mean spectral number density $N(E)$ of photons illuminating the object. This model is plotted with a normalized maximum value in Fig. 3.2, and was used to calculate the power spectral density $P(E) \propto EN(E)$.

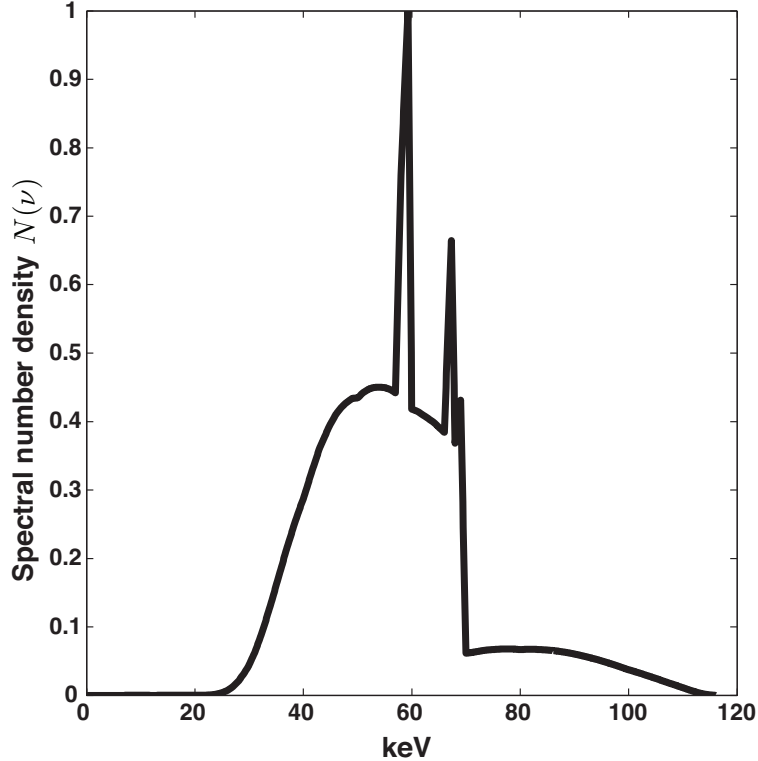


Figure 3.2: XSPEC model for the source spectral number density $N(E)$ at the object.

Scattered x-rays were collected with a stationary amorphous silicon indirect cesium iodide (CsI) flat panel detector (Paxscan, 4030 CB series, Varian Medical Systems, Palo Alto, CA) designed to perform with extended dynamic range. The detector had a pixel size of $194 \mu\text{m}$ and a matrix size of 2048×1536 . The source-to-image distance was 201 cm. The detector was gain-calibrated at the expected photon flux. Furthermore, it was offset calibrated before each acquisition with 16 dark frames to correct for structured noise. Post-calibrated images were acquired using the image acquisition and processing software ViVA (Varian Medical Systems).

The pencil beam was achieved using a primary aperture at a distance of 130 cm from the source. The primary aperture consisted of a hole 2 mm in diameter drilled into a 6 mm thick lead sheet. Taking into account the focal spot size of 0.6 mm, the beam divergence half-angle is estimated to have been about 0.06° , which approximately satisfies the parallel ray condition for an ideal pencil beam. The secondary aperture was placed 180 cm from the

source and consisted of another 6 mm thick lead sheet oriented parallel to the detector. The aperture, with its x-ray projection shown in Fig. 3.3, had a square center piece designed to block the primary beam and the horizontal bar structures served as supports. The aperture code was designed to implement equation (3.2) with $u = 9.9 \text{ cm}^{-1}$ so that the period was 0.64 cm.

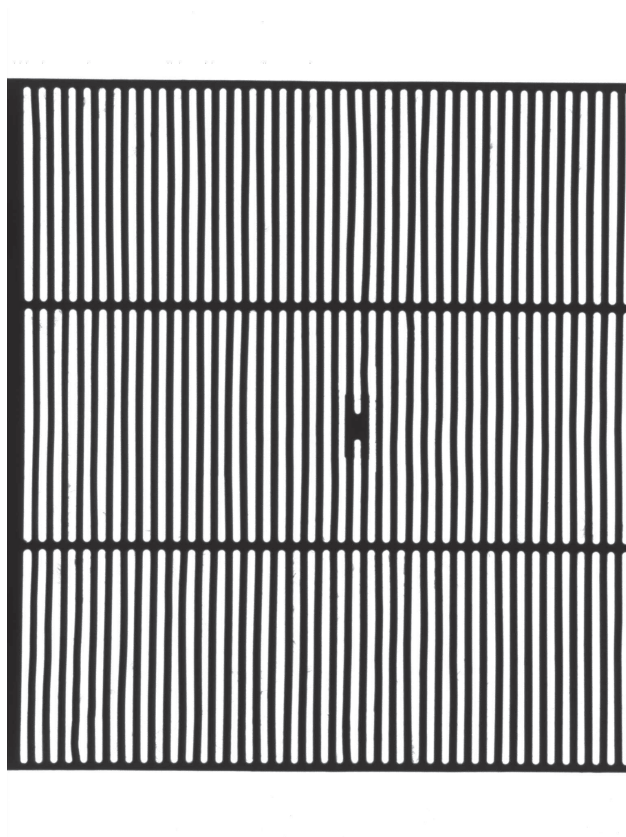


Figure 3.3: X-ray projection of the $29.7 \text{ cm} \times 29.4 \text{ cm}$ secondary aperture (full detector image). The aperture is cropped slightly in the horizontal direction, and the features are slightly irregular due to sagging of the lead.

Two crystalline powders, sodium chloride (NaCl) and aluminum (Al), were chosen as scattering targets for their strong coherent-scatter cross sections and applicability to powder detection. These samples were placed in separate Nalgene vials of 1 cm outer diameter. The Nalgene vials themselves were identical, and had negligible contributions to the scatter signal. This was found by measuring the scatter image from an empty vial, which was

indistinguishable from the background noise. Throughout the experiments, the vials were consistently placed so that the beam penetrated their full diameters.

The results presented in Section 3.5 are based on three different object configurations, with the simple goal of demonstrating the system’s ability to simultaneously resolve both z and q . These configurations are summarized in Table 3.1.

Configuration:	A	B	C
NaCl sample	$z = -60.2$ cm	-	$z = -60.2$ cm
Al sample	-	$z = -60.2$ cm	$z = -52.6$ cm

Table 3.1: Table outlining the three sample configurations for this experiment, with the z coordinate given for the center location of each vial. In configuration A, the NaCl was placed alone in the beam. In configuration B, the Al was alone in the beam. For configuration C, both samples were placed in the beam at different locations.

The first configuration (A) included only a vial of NaCl centered at 60.2 cm from the detector, at coordinate $z = -60.2$ cm (in the computational model the range was expressed in negative values). This configuration produced the diffraction image shown in Figure 3.4a, where the Debye rings from NaCl are visible, with modulation imposed by the coded aperture. Each ring is centered on the detector location which would be the location of the pencil beam, if it were not blocked by a beam stop.

The second configuration (B) repeated the first, but with Al instead of NaCl in the vial. This produced the diffraction image in Figure 3.4b, which is similar to the image obtained with NaCl but with different sized rings. The shadow of the aperture is basically identical in Figures 3.4a and 3.4b since the samples were placed at the same location.

The third configuration (C) was meant to test the system’s ability to measure the diffraction spectra of two samples at different ranges. The vial of NaCl was placed at $z = -60.2$ cm, as before, and the vial with Al was placed closer to the detector at $z = -52.6$ cm. This produced the image in Figure 3.4c, which is essentially a superposition of the diffraction patterns from the separate samples. Note that this is not, however, a superposition of Figures 3.4a and 3.4b, since the Al sample was placed at a different location to acquire Figure 3.4c.

The Al sample was deliberately placed closer to the detector to decrease the radius of the rings and cause potential confusion with the NaCl rings. Since the NaCl was kept in the same location, the contribution from NaCl to Figure 3.4c is essentially that shown in Figure 3.4a, ignoring noise effects. The more uniform parts of the scatter image, away from the diffraction rings, are best to examine the modulation from the aperture. The visibility of this modulation varies with x (horizontal) since it is a superposition of two different frequencies, each corresponding to a specific sample range and thereby enabling reconstruction along z . All three images in Figure 3.4 were normalized for viewing to keep the peak brightness constant.

In addition to the diffraction images, a background frame was acquired with no samples in the beam in order to measure any additional radiation from secondary sources in the system. The diffraction images along with the background images were used to reconstruct the scattering profiles of each test object as a function of position and momentum transfer, and these were compared with individual reference profiles measured by an X'Pert PRO commercial x-ray powder diffractometer (PANalytical B.V., Almelo, The Netherlands) with prepared samples in known positions. The next section describes the algorithm used to reconstruct the test objects, and Section 3.5 discusses the reconstruction results.

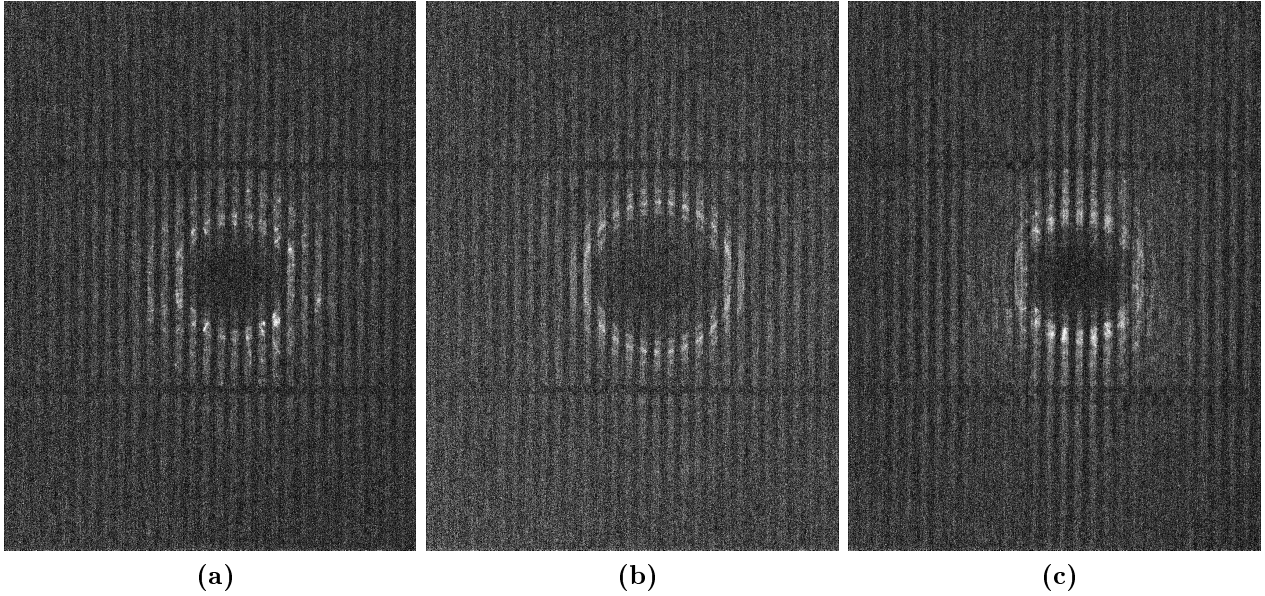


Figure 3.4: Diffraction images acquired with (a) NaCl, (b) Al, and (c) a combination of NaCl and Al placed in the beam.

3.4 Reconstruction algorithm

The data collected by the system discussed above consisted of superpositions of the scattered radiation from different test objects in the beam. This section describes how the scattering density for each configuration was estimated from the corresponding scatter image.

Given the discrete measurement model (3.5), each diffraction image is represented by a vector \mathbf{g} . The images also contained a noisy background with mean \mathbf{g}_0 so that the expected value at each pixel is given by $\mathbf{g} = \mathbf{H}\mathbf{f} + \mathbf{g}_0$. Treating the x-ray detection as a statistical process, the actual measurements $\tilde{\mathbf{g}}$ are approximated by the Poisson process

$$\tilde{\mathbf{g}} \sim \text{Poisson}(\mathbf{H}\mathbf{f} + \mathbf{g}_0),$$

where $\text{Poisson}(\mathbf{v})$ is a vector of independent Poisson observations with mean values given by the components of some mean vector \mathbf{v} . Given $\tilde{\mathbf{g}}$, \mathbf{H} , and a noisy measurement of the background $\tilde{\mathbf{g}}_0 \sim \text{Poisson}(\mathbf{g}_0)$, we are interested in estimating \mathbf{f} as accurately as possible.

The process begins by estimating \mathbf{g}_0 from $\tilde{\mathbf{g}}_0$ using a Poisson image de-noising algorithm,

and using the resulting estimate $\hat{\mathbf{g}}_0$ of \mathbf{g}_0 to reconstruct \mathbf{f} . In particular, \mathbf{g}_0 was estimated using a maximum penalized likelihood estimation method discussed in [74], according to which:

$$\hat{\mathbf{g}}_0 \equiv \arg \min_{\mathbf{g}_0 \in \Gamma} (-\log \mathbb{P}(\tilde{\mathbf{g}}_0 | \mathbf{g}_0) + \tau \text{pen}(\mathbf{g}_0))$$

where the Poisson likelihood $\mathbb{P}(\mathbf{a} | \mathbf{b})$ for the noisy vector \mathbf{a} with mean \mathbf{b} is given by a product of independent Poisson distributions:

$$\mathbb{P}(\mathbf{a} | \mathbf{b}) = \prod_i \frac{\exp(-b_i) b_i^{a_i}}{a_i!},$$

and $i = 1 \dots N$ indexes the detector pixels. Γ is a collection of possible estimates to search from, $\text{pen}(\mathbf{g}_0)$ is the penalization or the regularization function corresponding to estimate \mathbf{g} , and τ is the term that balances the log-likelihood term and the penalization term. The class of estimates Γ was obtained by partitioning the image space in a recursive-dyadic (powers of two) fashion from coarser to finer cells, and fitting a constant to each partition cell. The algorithm chose the multi-scale, partition-based estimate that was the best fit to the data and was also piecewise smooth. The penalization term is proportional to the number of cells in the partition and is used to enforce prior knowledge that \mathbf{g}_0 is piecewise smooth. Given $\hat{\mathbf{g}}_0$, \mathbf{f} was estimated according to a generalized maximum likelihood (GML) estimator given by

$$\hat{\mathbf{f}} \equiv \arg \min_{\mathbf{f}} (-\log \mathbb{P}(\tilde{\mathbf{g}} | \mathbf{H}\mathbf{f} + \hat{\mathbf{g}}_0)).$$

The GML estimate of \mathbf{f} can be obtained using an iterative deconvolution method such as that described in References [59,60]. A pseudo-code of this iterative reconstruction method is provided below:

1. Initialize $\hat{\mathbf{f}}_0 = \mathbf{H}^T \tilde{\mathbf{g}}$.
2. For iteration $k = 0, 1, \dots$

- (a) $\hat{\mathbf{f}}_{k+1} = \hat{\mathbf{f}}_k \cdot * \mathbf{H}^T \left(\tilde{\mathbf{g}} ./ \left[\mathbf{H}\hat{\mathbf{f}}_k + \hat{\mathbf{g}}_0 \right] \right) ./ (\mathbf{H}^T \mathbf{1}_{N \times 1})$ where $\cdot *$ and $./$ are element-wise operations and $\mathbf{1}_{N \times 1}$ is a vector of ones of size $N \times 1$.
- (b) Stop iterating if $\mathbb{P}(\tilde{\mathbf{g}} | \mathbf{H}\hat{\mathbf{f}}_{k+1} + \hat{\mathbf{g}}_0) \leq \mathbb{P}(\tilde{\mathbf{g}} | \mathbf{H}\hat{\mathbf{f}}_k + \hat{\mathbf{g}}_0)$ (the likelihood begins to decrease)

3. The final estimate is given by $\hat{\mathbf{f}} = \hat{\mathbf{f}}_k$.

The stopping criterion (step 2b) assumes convergence, and was used for the reconstructions. In general, the solution $\hat{\mathbf{f}}$ may be a local instead of global maximum of the likelihood. To avoid stopping if the likelihood oscillates, one could require that the stopping criterion is satisfied for a certain number of consecutive iterations. To avoid unproductive computations, the stopping criterion could also be made to quit when the improvement in the likelihood or change in $\hat{\mathbf{f}}$ falls below a set threshold.

In the experimental setup, the detector array consisted of 2048×1536 square pixels. In order to reduce computational complexity, “polar down-sampling” was applied to the measured diffraction images. Aside from modulation by the aperture, the diffraction patterns consisted of concentric rings which can be effectively represented over bins in the polar coordinates (ρ, ϕ) relative to the beam position. In practice, relatively few polar bins are sufficient to reliably capture the information content in the diffraction images. The images were partitioned into 233 uniform radius bins between $\rho = 2.5$ cm and $\rho = 11.5$ cm. The polar angle was similarly segmented over its entire range into 120 bins. As a result of this strategy, the image was reduced from 2048×1536 to 233×120 pixels, which afforded significant savings in the computation of \mathbf{H} . Examples of these “polar down-sampled” images are shown in Figure 3.10.

The GML algorithm described above was applied to the diffraction data (Figure 3.4) in order to estimate \mathbf{f} for each test configuration. These results are discussed in the next section.

3.5 Results and discussion

The forward matrix \mathbf{H} for the pencil beam system was calculated by sampling the object space with voxels of width 0.33 cm in z and 0.027 nm^{-1} in q . Here, numerical values of q are expressed in nm^{-1} , where $(q \text{ in } \text{nm}^{-1}) = (q \text{ in } \text{keV}/c) / (2h)$, where h is the Planck constant. This is done to match the definition of momentum transfer “ x ” used in Reference [66].

From the single-frame diffraction images shown in Figure 3.4 for each configuration A, B, and C (Table 3.1), the vector \mathbf{f} representing the scattering density $F(z, q)$ was estimated using the methods described in the previous section. Plots of the recovered scattering density $F(z, q)$ are shown for each configuration in Figures 3.5, 3.6, and 3.7, where the color scale indicates the value of $F(z, q)$. In these figures, the dotted white lines correspond to the constant z values used to plot the momentum transfer spectra in Figures 3.8 and 3.9 below.

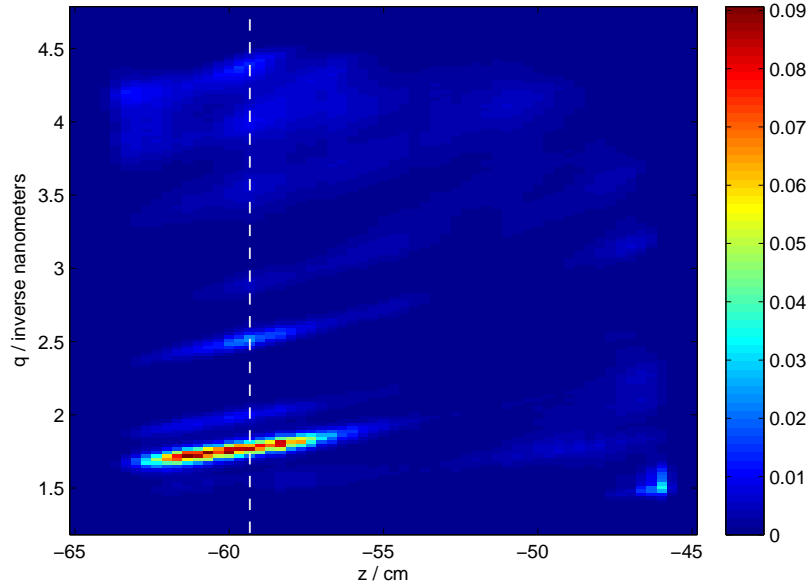


Figure 3.5: Reconstructed scattering density $F(z, q)$ for configuration A with NaCl at $z = -60.2 \text{ cm}$. The dotted white line indicates the spatial location used for plotting the momentum transfer profile in Figure 3.8c.

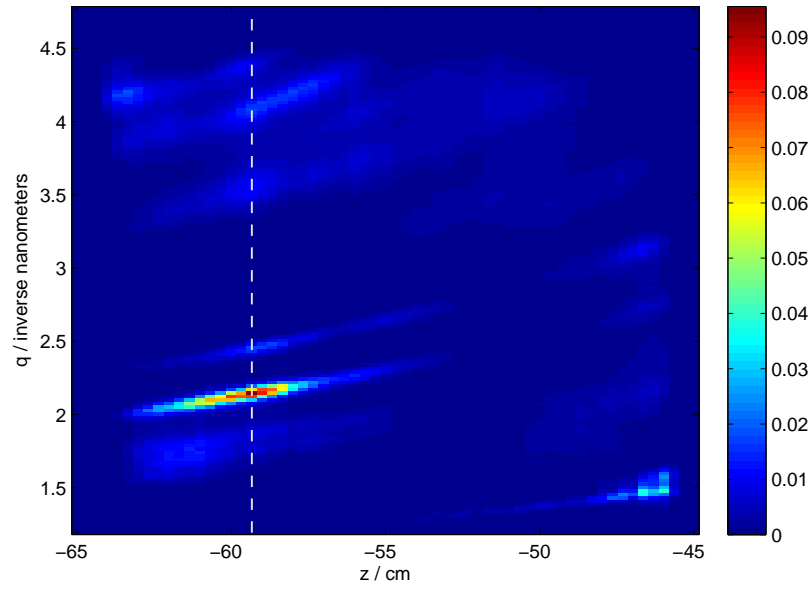


Figure 3.6: Reconstructed scattering density $F(z, q)$ for configuration B with Al at $z = -60.2$ cm. The dotted white line indicates the spatial location used for plotting the momentum transfer profile in Figure 3.8d.

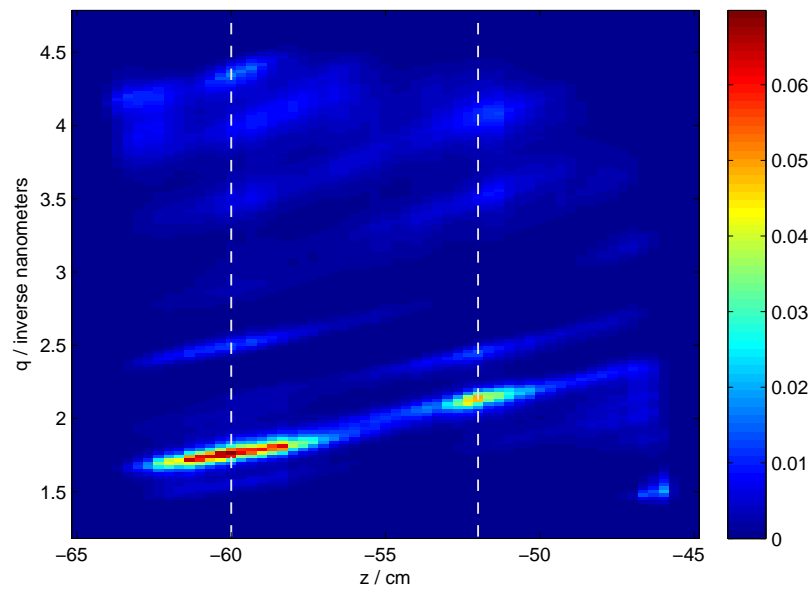


Figure 3.7: Reconstructed scattering density $F(z, q)$ for configuration C with NaCl at $z = -60.2$ cm and Al at $z = -52.6$ cm. The dotted white lines indicate the spatial locations used for plotting the momentum transfer profiles in Figures 3.9b and 3.9c.

Figures 3.8a and 3.8b show the estimated spatial distributions $f(z) = \int dq F(z, q)$ of the scattering densities recovered for NaCl and Al placed separately in the beam at $z = -60.2$ cm (configurations A and B in Table 3.1). Although the beam penetrated only 1 cm of each sample, the spatial reconstructions show full-width-half-max (FWHM) in z equal to 5 cm (8.5%) for the NaCl sample and 5.7 cm (9.6%) for the Al sample. The peak of the spatial profile occurs at $z_0 = -59.3$ cm for both samples, marked by the dotted white lines in Figures 3.5 and 3.6. This value of z_0 lies 0.9 cm from the true location of the center of the vial. But scattering originates all along the 1 cm vial, corresponding to an uncertainty in the true peak of 1 cm. The position error for the independent experiments (A) and (B) are therefore bounded between 0.4 cm and 1.4 cm (between 0.7% and 2.3%), showing a slight bias but making a quite reasonable measurement of z for the two samples. This demonstrates the along-beam ranging capability of the coded aperture system.

Figures 3.8c and 3.8d show the estimated momentum transfer profiles $f(q) = F(z_0, q)$ at the spatial peak $z_0 = -59.3$ cm for NaCl and Al from their separate configurations A and B, respectively. These followed the dotted white lines in Figures 3.5 and 3.6. The dotted red lines in Figures 3.8c and 3.8d are the known diffraction profiles for each powder, acquired with carefully prepared samples in a PANalytical X'Pert Pro diffractometer. The dominant peaks in both profiles were accurately reconstructed, and there is evidence of some of the smaller peaks. The dominant peak for NaCl was reconstructed at $q = 1.767 \text{ nm}^{-1}$ (0.2% error) with a FWHM of 0.06 nm^{-1} (3.6%). The dominant peak for Al was reconstructed at $q = 2.149 \text{ nm}^{-1}$ (0.4% error) and a FWHM of 0.07 nm^{-1} (3.3%). These results show that the pencil beam coded aperture system can be used to estimate the diffraction spectra of target samples without *a priori* position information.

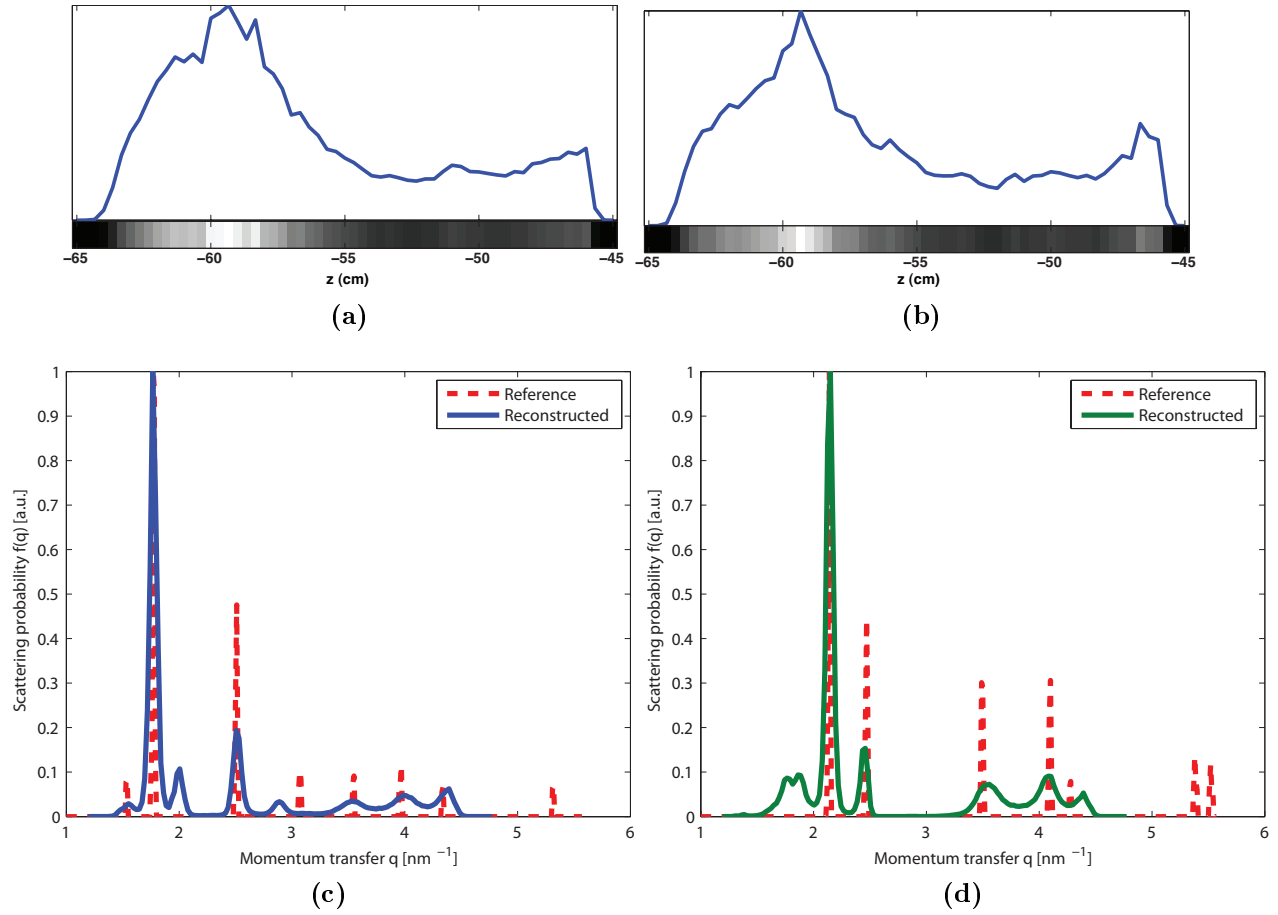


Figure 3.8: Reconstruction results when a single sample (NaCl or Al) is placed along the beam (configurations A and B). The along-beam distance z is measured in negative values from the detector. (a) Spatial scattering profile $f(z)$ for NaCl in configuration A. (b) Spatial scattering profile $f(z)$ for Al in configuration B. (c) Momentum transfer profile $f(q)$ for NaCl in configuration A. (d) Momentum transfer profile $f(q)$ for Al in configuration B. The red “reference” profiles are the known x-ray diffraction profiles for each sample.

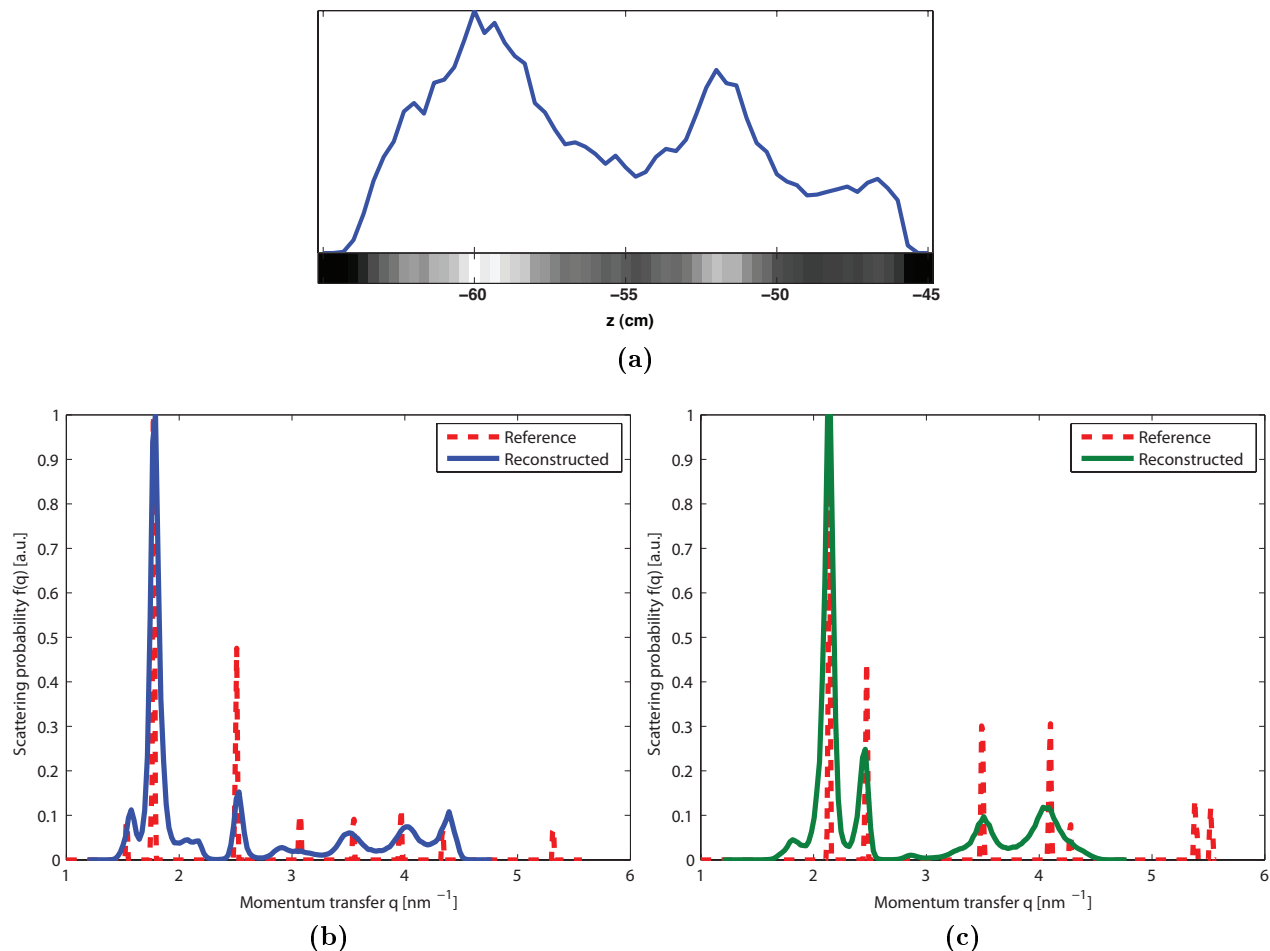


Figure 3.9: Reconstruction results with both samples in the beam (configuration C). (a) Spatial scattering profile $f(z)$ with both samples in the beam. (b) Momentum transfer profile $f(q)$ for NaCl at $z = -59.3$ cm. (c) Momentum transfer profile $f(q)$ for Al at $z = -52$ cm. The red “reference” profiles are the known x-ray diffraction profiles for each sample.

To test the system’s ability to distinguish different objects in the beam within a single snapshot, one vial of NaCl and one vial of Al were placed along the beam at $z = -60.2$ cm and $z = -52.6$ cm, respectively, according to configuration (C). In this configuration the pencil beam passed first through the NaCl sample and then through the Al sample, producing the diffraction image shown in Figure 3.4c. As before, the coefficients \mathbf{f} were reconstructed and produced the scattering density $F(z, q)$ shown in Figure 3.7. The spatial scattering profile $f(z) = \int dq F(z, q)$ was computed and is shown in Figure 3.9a. The spatial distribution shows a peak for NaCl at $z = -59.3$ cm, and as before the position error is bounded by 0.4 cm and 1.4 cm (0.7% and 2.3%). The peak for Al occurs at $z = -52.0$ cm, with the

position error bounded by 0.1 cm and 1.1 cm (0.2% and 2.1%). The FWHM of each peak are 5 cm for NaCl (8.9%) and 4 cm for Al (7.7%). Momentum transfer profiles for these two locations are shown in Figs. 3.9b and 3.9c. The dominant peak for NaCl was reconstructed at $q = 1.79 \text{ nm}^{-1}$ with FWHM equal to 4.7%. The dominant peak for Al was estimated to lie at $q = 2.137 \text{ nm}^{-1}$ (0.3% error) with FWHM equal to 4.7%. The reconstructed momentum transfer profiles are consistent, whether the objects are measured separately or placed together in the beam. The four dominant Al diffraction peaks were reconstructed successfully for both locations at which the sampled was placed.

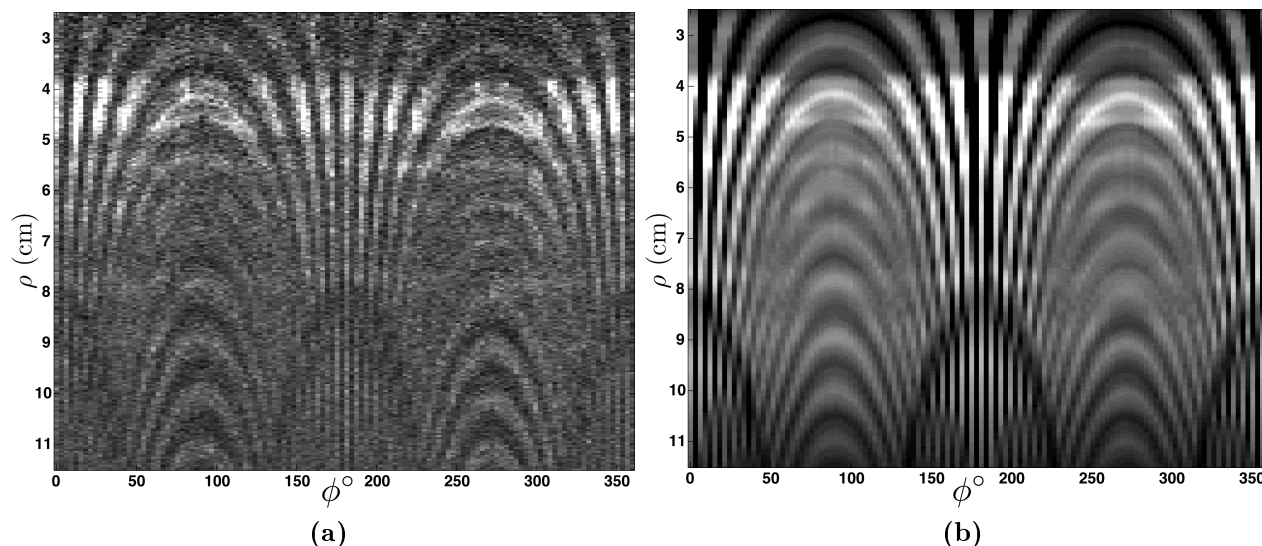


Figure 3.10: Polar plots of (a) the combined NaCl and Al diffraction pattern and (b) the modeled diffraction pattern $\mathbf{H}\hat{\mathbf{f}}$ based on the corresponding object estimate $\hat{\mathbf{f}}$ and the forward model \mathbf{H} described in Section 3.2.

The combined NaCl and Al diffraction pattern (Figure 3.4c) is plotted in Figure 3.10a over the polar coordinates (ρ, ϕ) . Figure 3.10b shows the modeled diffraction pattern $\mathbf{H}\hat{\mathbf{f}}$ based on the corresponding object estimate $\hat{\mathbf{f}}$ and the forward model \mathbf{H} described in Section 3.2. The root-mean-squared error between these diffraction patterns is approximately 10% of the peak signal value in $\mathbf{H}\hat{\mathbf{f}}$, indicating agreement between the two images and providing combined validity to the measurement model, the experimental process, and the

reconstruction algorithm. We suspect that shot noise and dark current noise are the primary contributors to the differences between the two images.

There are several key limitations to the system demonstrated here. Because an irradiance detector was used, the spectral characteristics of the source play a role in achieving good momentum transfer resolution. The interplay between spectral filtering and scatter signal strength could be evaluated. Varying the exposure to produce different signal-to-noise ratios, or varying geometric parameters will also affect the results. The coded aperture could be built with finer features, which could improve the achievable resolution in space and momentum transfer. For strongly attenuating or scattering objects, the attenuation of the primary and scattered radiation should be accounted for using a nonlinear forward model.

These results demonstrate the use of coded apertures for pencil beam tomography with a single snapshot, while recovering the coherent scatter diffraction profile of the target at each point along the beam. The momentum transfer resolution should be sufficient for performing spatially resolved material identification when the scattering materials are unknown. Effects of noise, the system geometry, and acquisition parameters should be studied in detail for specific applications of these techniques. The pencil beam system is a solid foundation for understanding more sophisticated CAXSI experiments, and the following chapter demonstrates an extension of this work to fan beam tomography.

CHAPTER 4: FAN BEAM CAXSI

(Adapted from previously published work [32])

4.1 Background

This chapter describes a fan beam x-ray system demonstrating coded aperture x-ray scatter imaging (CAXSI). In the previous chapter, pencil beam CAXSI was demonstrated which reconstructed coherent scattering densities along the beam from a single snapshot. The success of the pencil beam system inspired the following experiment which demonstrates snapshot 2D tomography using the coded aperture proposed in Section 2.4 of Chapter 2, while also measuring an angular scattering function based on the the object's differential scattering cross section. In the language of Chapter 1, this corresponds to the transformation $F(x, z) R(\theta) \rightarrow G(x, y)$, where $F(x, z)$ is the unknown scattering density in 2D, $R(\theta)$ is the “radiance” (power per solid angle) as a function of the scatter angle θ , and $G(x, y)$ is the measured irradiance image. This is closely related to the isotropic system $F(x, z) \rightarrow G(x, y)$ from Chapter 2, but with $R(\theta)$ allowing for anisotropic scattering with azimuthal symmetry.

Fan beam CAXSI is a snapshot technique for 2D tomography, and can be used to acquire tomographic x-ray video of dynamic objects, suggesting possibilities for medical imaging. To achieve 3D tomography of static objects, the object may be linearly scanned through the plane of the fan beam. This idea will be revisited in Chapter 5 where coded apertures are proposed for cone beam scatter imaging.

Snapshot 2D tomography has been demonstrated with a pinhole aperture and an irradiance detector placed parallel to a fan beam, with a proposal to replace the pinhole with a coded aperture for increased signal strength [14]. The fan beam system used here is illustrated in Figure 4.1, showing the fan beam collimator, alignment rail, coded aperture,

and detector. This drawing also shows an object stage made from foam and a clock we used to demonstrate scatter video. Chapters 2 and 3 gave a lot of attention to coded apertures based on the transmission $T(y) = (1 + \cos(y))/2$, which project a specific spatial frequency distribution on the detector depending on the range distribution of the scattering density. The orthogonality of the signals from each range via their unique frequencies enables one to determine the scattering contribution from each range.

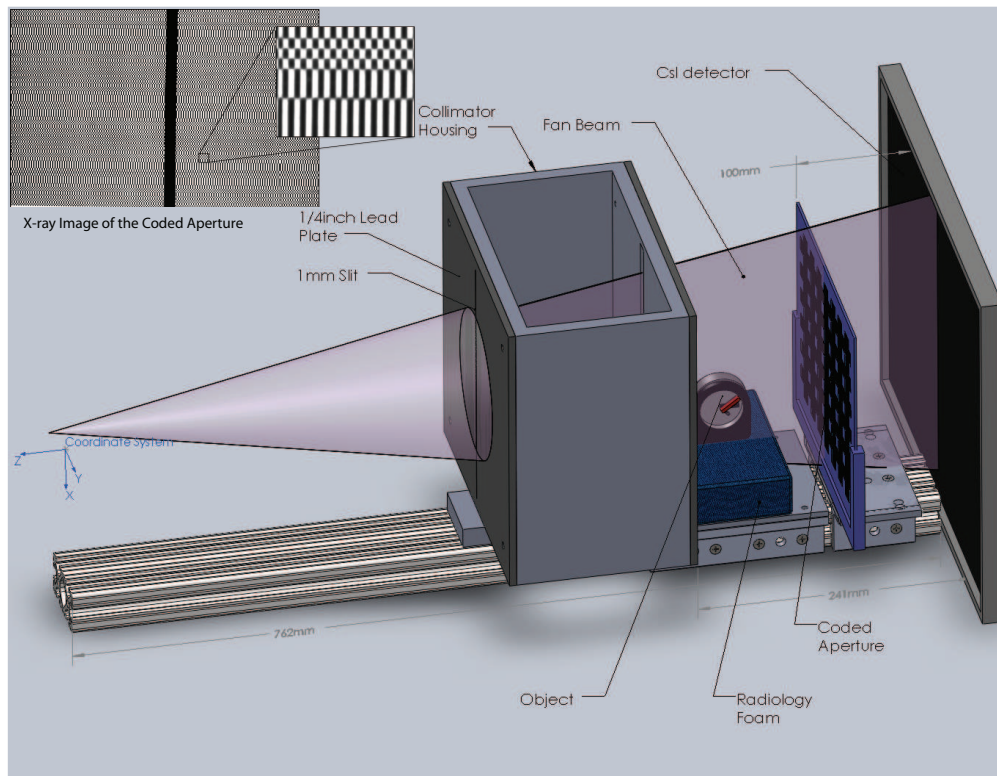


Figure 4.1: Diagram of the experimental system

The coded aperture used in the following is based on the one proposed in Section 2.4 of Chapter 2. The code includes a sinusoid code (the “scale” code) in the y coordinate for range sensitivity while introducing phase reversals along the x direction based on a quadratic residue code (the “shift” code). The shift code was based on the length-41 MURA code of Reference [56].

The transmission of the coded aperture follows

$$T(x, y) = \left(\frac{1 + \sum_i A_i \text{rect}(ux - i) \sum_j (-1)^j \text{rect}(2\nu y - j)}{2} \right), \quad (4.1)$$

where the direction x is parallel to the fan beam and y is perpendicular. The function $\text{rect}(\dots)$ is a unit square pulse, and the summation over j produces a periodic dependence on y . The spatial frequencies u and ν define the size of the code features in each direction, and the value $A_i = \pm 1$ is the i^{th} element of the shift code. The code transmittance (4.1) differs from the theoretical one (equation (2.8) of Chapter 2) in the fact that it is binary, which simplifies the manufacturing process. Also, the roles of the Cartesian coordinates x and y are swapped relative to Chapter 2.

With the coded aperture defined by (4.1), each point in the $x-z$ plane produces a unique scatter signal. For instance, a single point scatterer projects a shadow of the aperture onto the detector. One uses the magnification of the y -axis harmonic code to determine z and the shift of the x -axis code to determine x . When an extended object is placed in the beam, the superposition of signals can be decomposed to reconstruct a tomographic image of the scattering distribution. In the following section, the underlying theory of the forward model and reconstruction algorithm for this fan beam system is presented. Section 4.3 describes the experimental setup and methods, followed by reconstruction results in Section 4.4 and a chapter summary in Section 4.5

4.2 Theory

4.2.1 Forward model

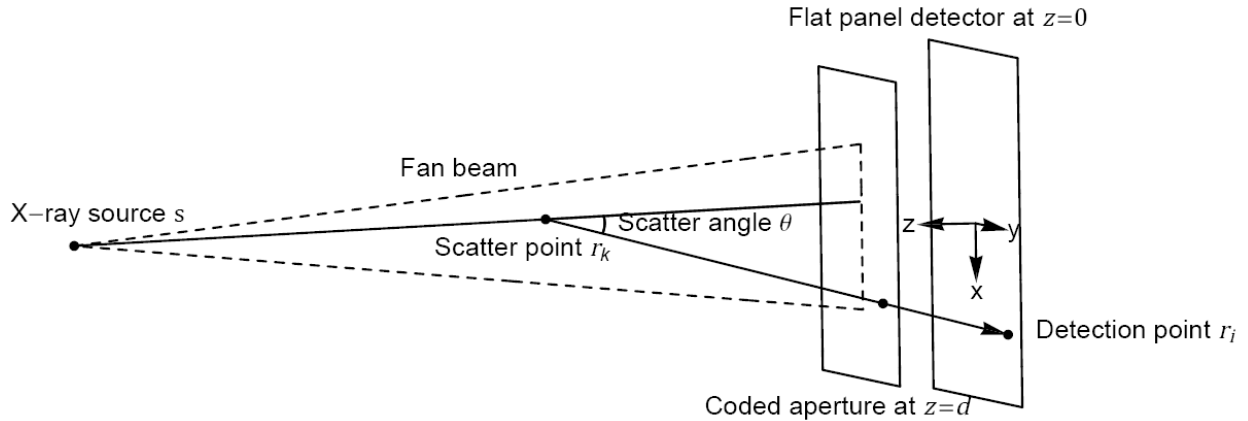


Figure 4.2: Coordinate system diagram showing a single scattering event.

Figure 4.2 shows the coordinate system used to describe each scattering event. The detector defines the plane $z = 0$ while the fan beam propagates in the plane $y = 0$. The coded aperture defines the plane $z = d$ and implements the transmission function $T(x, y)$ defined by equation (4.1). The object is positioned between the source and the coded aperture, producing scattered radiation due to the incident fan beam. The scatter signal is encoded by the aperture before reaching the detector plane.

The fan beam model in Section 2.4 of Chapter 2 assumed isotropic scattering. The model proposed here relaxes this assumption, allowing for anisotropic scattering with azimuthal symmetry, applicable to liquids, powders, or amorphous solids. The object is represented by density $F(\mathbf{r})$ and scattered radiance $R(\theta)$, where θ is the scatter angle. Here, the radiance $R(\theta)$ is discovered through the reconstruction process, and is theoretically proportional to $\int dE P(E) \frac{d\sigma}{d\Omega}(E, \theta)$, where E is the x-ray energy, P is the power spectral density of the detected x-rays, and $\frac{d\sigma}{d\Omega}$ is the differential scattering cross section of the material under investigation.

For an inhomogeneous object, $R(\theta)$ would vary from point to point, posing the imaging problem which reconstructs the 3D $F(x, z, \theta)$ from 2D measurements $G(x, y)$. This may be

possible, for example using compressive inference to impose statistical structure on $F(x, z, \theta)$. Here, homogeneity of the scattering material is assumed instead. This allows the factorization $F(x, z, \theta) = F(x, z)R(\theta)$, which is largely responsible for the success of this demonstration.

Denoting 3D vectors by bold \mathbf{r} , and ignoring proportionality constants, the linear forward model is

$$G_j(\mathbf{r}) = \int_{\mathbf{r}' \in \mathcal{V}} d^3\mathbf{r}' \frac{T\left(\mathbf{r} + (\mathbf{r}' - \mathbf{r}) \frac{d}{z'}\right)}{|\mathbf{r}' - \mathbf{r}|^2} F_j(\mathbf{r}') R(\theta) \quad (4.2)$$

where $G_j(\mathbf{r})$ is the measured irradiance image for exposure j , \mathcal{V} is the volume of the beam and $F_j(\mathbf{r})$ is the object's exposed scattering density for frame j . The scatter angle θ is implicitly a function of the source location \mathbf{s} , the scatter point \mathbf{r}' , and the measurement position \mathbf{r} . The factor $|\mathbf{r}' - \mathbf{r}|^{-2}$ is the geometric propagation factor for the scattered field. The forward model (4.2) may apply to imaging a 3D static density $F_j(\mathbf{r}) = F(x, y - y_j, z)$ by selecting a sequence of object planes y_j for each exposure (e.g. by linear translation), or imaging a dynamic density $F(x, z, t_j)$ by choosing the observation times t_j . This latter technique is demonstrated below.

The continuous forward model (4.2) represents the linear transformation between the scattering density $F_j(\mathbf{r})R(\theta)$ and the irradiance $G_j(\mathbf{r})$ at frame j . The detector discretized the measurements by representing each image as a matrix of pixel values. The detector pixels are centered at the coordinates \mathbf{r}_i located on a rectangular grid in the plane $z = 0$. With reference to Section 1.4 of Chapter 1, the measurement basis $\Phi_i(x, y) = \delta(x - x_i) \delta(y - y_i)$ was assumed. This point-like sampling was chosen for computational speed. The discrete measurements form the matrix \mathbf{g} with components

$$g_{ij} = G_j(\mathbf{r}_i) \quad (4.3)$$

The function $F_j(\mathbf{r})$ is represented as a superposition of point scatterers via the basis functions $\Psi_k(x, z) = \delta(x - x_k) \delta(z - z_k)$:

$$F_j(\mathbf{r}) = \sum_k \delta(x - x_k) \delta(z - z_k) f_{kj} \quad (4.4)$$

where $\delta(\dots)$ is the Dirac delta function, $\mathbf{r}_k = (x_k, z_k)$ is a set of 2D vectors defining the sampling of the object in the plane of the beam (a rectangular grid was used), k is an index over basis elements, and f_{kj} are the density samples to be estimated. The point-like sampling for the object and detector simplifies the computation compared to other representations (e.g. Fourier, Haar, wavelets, etc.). Using (4.3) and (4.4) with (4.2),

$$g_{ij} = \sum_k \frac{T\left(\mathbf{r}_i + (\mathbf{r}_k - \mathbf{r}_i) \frac{d}{z_k}\right)}{|\mathbf{r}_i - \mathbf{r}_k|^2} R(\theta_{ik}) f_{kj}, \quad (4.5)$$

where $\theta_{ik} = \cos^{-1} \frac{(\mathbf{r}_i - \mathbf{r}_k) \cdot (\mathbf{r}_k - \mathbf{s})}{|\mathbf{r}_i - \mathbf{r}_k| |\mathbf{r}_k - \mathbf{s}|}$ is the scatter angle for the ray connecting object point \mathbf{r}_k and detector point \mathbf{r}_i , given the source position \mathbf{s} . Define the radiance matrix \mathbf{R} with components $R_{ik} = R(\theta_{ik})$ and the geometry matrix \mathbf{G} with components $G_{ik} = T\left(\mathbf{r}_i + (\mathbf{r}_k - \mathbf{r}_i) \frac{d}{z_k}\right) / |\mathbf{r}_i - \mathbf{r}_k|^2$. Equation (4.5) is written in matrix form as

$$\mathbf{g} = (\mathbf{G} * \mathbf{R}) \mathbf{f}, \quad (4.6)$$

where $*$ represents element-wise multiplication and \mathbf{f} is the scattering density with components f_{kj} .

The angle dependence $R(\theta)$ was sampled using the $\text{rect}(\dots)$ function ($\text{rect}(x) = 1$ if $|x| < 1/2$ and $\text{rect}(x) = 0$ otherwise), producing scatter angle bins indexed by l and centered at θ_l with widths $\Delta\theta_l$:

$$R(\theta) = \sum_l b_l \text{rect}\left(\frac{\theta - \theta_l}{\Delta\theta_l}\right)$$

The coefficients b_l form the vector \mathbf{b} and were determined by the reconstruction along with \mathbf{f} by inverting (4.6).

4.2.2 Reconstruction algorithm

The discrete forward model (4.6) was used with Maximum Likelihood Estimation (MLE) [75] to obtain our results. The following derivation is based on the MLE algorithm from Section 1.5 in Chapter 1, but with the added ability to estimate \mathbf{f} and \mathbf{b} in an alternating fashion. Assume independent Poisson noise at each detector pixel. The components of the measurement vector $\tilde{\mathbf{g}}$ are distributed with mean values given by the corresponding components of \mathbf{g} , plus a measured background \mathbf{g}_0 :

$$\tilde{\mathbf{g}} \sim \text{Poisson}(\mathbf{g} + \mathbf{g}_0).$$

Define the vector containing all unknown parameters as $\mathbf{x} = (\mathbf{f}, \mathbf{b})$, and let $P(\tilde{\mathbf{g}}|\mathbf{x})$ be the probability of observing $\tilde{\mathbf{g}}$ given object coefficients \mathbf{x} . By enforcing $\partial P(\tilde{\mathbf{g}}|\mathbf{x})/\partial \mathbf{x}$ to vanish in order to achieve a maximum likelihood, we obtain the condition

$$\frac{\sum_{ij} \frac{\partial g_{ij}}{\partial \mathbf{x}} \frac{\tilde{g}_{ij}}{g_{ij} + g_{0ij}}}{\sum_{ij} \frac{\partial g_{ij}}{\partial \mathbf{x}}} = \mathbf{1}_{\mathbf{x}} \quad (4.7)$$

where $\mathbf{1}_{\mathbf{x}}$ is a vector of ones with the same size as \mathbf{x} . This suggests the iterative update

$$\mathbf{x}^{n+1} = \mathbf{x}^n \cdot * \frac{\sum_{ij} \frac{\partial g_{ij}}{\partial \mathbf{x}} \frac{\tilde{g}_{ij}}{g_{ij} + g_{0ij}}}{\sum_{ij} \frac{\partial g_{ij}}{\partial \mathbf{x}}}$$

since this will stabilize when condition (4.7) is met. Define the vectors $\mathbf{\Pi}_{ik}$ with components $\text{rect}\left(\frac{\theta_{ik} - \theta_l}{\Delta \theta_l}\right)$ indexed by l . For the vectors \mathbf{f} and \mathbf{b} , the iterative update steps are

$$\mathbf{f}^{n+1} = \mathbf{f}^n \cdot * (\mathbf{G} \cdot * \mathbf{R})^T (\mathbf{y} \cdot / (\mathbf{g} + \mathbf{g}_0)) \cdot / (\mathbf{G} \cdot * \mathbf{R})^T \mathbf{1}_{\mathbf{g}} \quad (4.8)$$

$$\mathbf{b}^{n+1} = \mathbf{b}^n \cdot * \left(\sum_{ijk} \mathbf{\Pi}_{ik} G_{ik} f_{kj} \frac{y_{ij}}{g_{ij} + g_{0ij}} \right) \cdot / \left(\sum_{ijk} \mathbf{\Pi}_{ik} G_{ik} f_{kj} \right) \quad (4.9)$$

The forward model and reconstruction algorithm were coded in Matlab and updates were alternated between \mathbf{f} and \mathbf{b} using equations (4.8) and (4.9) to produce our results.

4.2.3 System design and resolution

Imaging in the range direction z is achieved by the harmonic code in the y direction. Based on the arguments of Section 2.2 in Chapter 2, the range resolution is

$$\Delta z = \frac{z^2}{Yvd} \quad (4.10)$$

Transverse imaging relies on distinguishability of the shift code when translated in the x direction. Translation of a scatter point from $(x, z) \rightarrow (x + \Delta x, z)$ shifts the shadow by one code period when

$$\Delta x = \frac{z}{ud}, \quad (4.11)$$

which is the equation for transverse resolution, assuming the complete code sequence is observed in the x direction.

The imaging resolution is limited by the feature size of the coded aperture and the sampling rate of the scatter signal at the detector. The resolution of any x-ray detector is limited by the interaction length of the x-rays and the detector material. Thicker materials provide increased stopping power with the side effect of pixel cross-talk, particularly for large incidence angles. A similar argument relates the resolution of the coded aperture with its thickness, which we found to be the limiting factor for our setup.

4.3 Experimental methods

4.3.1 Configuration

The fan beam assembly for this demonstration utilized an x-ray system previously developed for breast CT [76]. Figure 4.1 shows a diagram of the modified system including the fan beam collimator, alignment rail, coded aperture, and detector. This drawing also shows an object stage made from foam and a clock we used to demonstrate scatter video. The

collimated fan beam illuminated the object and x-rays scattered due to atomic interactions. The scattered x-rays were transferred by the coded aperture, under ray optics, to the detector plane where the scatter images were acquired.

4.3.2 Acquisition

The Rad-94 x-ray tube (Varian Medical Systems, Palo Alto, CA) was operated at generator settings of 120 kV, 25 mA, and a 400 ms pulse duration. The focal spot had a width of 0.4 mm and was stationed 775 mm from the detector plane. The source was spatially filtered by a series of lead collimators to produce a fan beam with 1 mm width and a full-angle divergence of 0.3° at the object stage. A flat panel scintillation detector (model 4030E, Varian Medical Systems) detected scattered x-rays with a 406 mm by 293 mm active area and 0.127 mm pixel pitch. The coded aperture was placed parallel to the detector at a distance $d = 100$ mm. At the intersection of the fan beam and the detector, a strip of lead ($100 \times 10 \times 3$ mm) blocked the primary beam. This beam stop prevented the primary beam from saturating the detector, and allowed for full sensitivity to the relatively weak scatter signal. All devices in the apparatus other than the source and detector were oriented along an 80/20 rail. Devices on the rail included the coded aperture, stage for the object, and a two-stage collimator that formed the fan beam. Each of these devices could be moved linearly along the z -direction but remained fixed for the experiments.

4.3.3 Aperture fabrication

The coded aperture was modeled in Matlab and a mold was printed on an Objet Eden 333 printer (Stratasys, Eden Prairie, MN). The mold was filled with tungsten powder (grain size $> 50 \mu\text{m}$) and sealed with epoxy. The mold was 1.35 mm deep with 0.3 mm plastic backing for support, and the filling process produced tungsten features about 1 mm thick (z) with minimum feature size 1.25 mm in x and 0.75 mm in y . The code area was 160 mm (x) by 200 mm (y). The plastic caused negligible attenuation of the x-rays compared with the tungsten features.

4.3.4 Model calibration

To ensure model accuracy, we experimentally determined the position of the x-ray anode. We placed the coded aperture parallel and at several known ranges from the detector. Next, we used ray tracing from paired aperture and image points to triangulate the position of the source and found an offset of $\mathbf{s} = (2.1, 12.8, 774.8)$ mm relative to the center of the detector. The source position information was then used to orient the fan beam perpendicular to the detector. The mathematical procedure for determining the source position is presented in Appendix C.

To avoid systematic errors in aperture placement, an empirical measurement of $T(x, y)$ was used in the forward model. Several x-ray projections of the coded aperture were acquired and averaged into a single image to reduce the effect of noise. The averaged image represented the transmission function $T(x, y)$ by using known information: the image's magnification, the source position, and the aperture-detector distance d . This image is shown as an inset in Figure 4.1.

4.3.5 Test objects

We chose to image plastic objects because they have strong scattering cross sections and the lack of long-range order produces cylindrically symmetric scattering profiles, as was assumed in Section 4.2. To demonstrate snapshot 2D imaging we formed the letters "DUKE" with our Objet printer. To demonstrate tomographic video, we used a clock with plastic hands. Figures 4.3a and 4.3b show the plastic DUKE letters and the clock in position for the experiments. Both were aligned parallel to the fan beam. The DUKE letters covered an area of 100 mm by 40 mm and were 5 mm thick in the y direction, though the beam only illuminated a 1 mm slice. Only the second hand of the clock was exposed to x-rays for that part of the experiment.

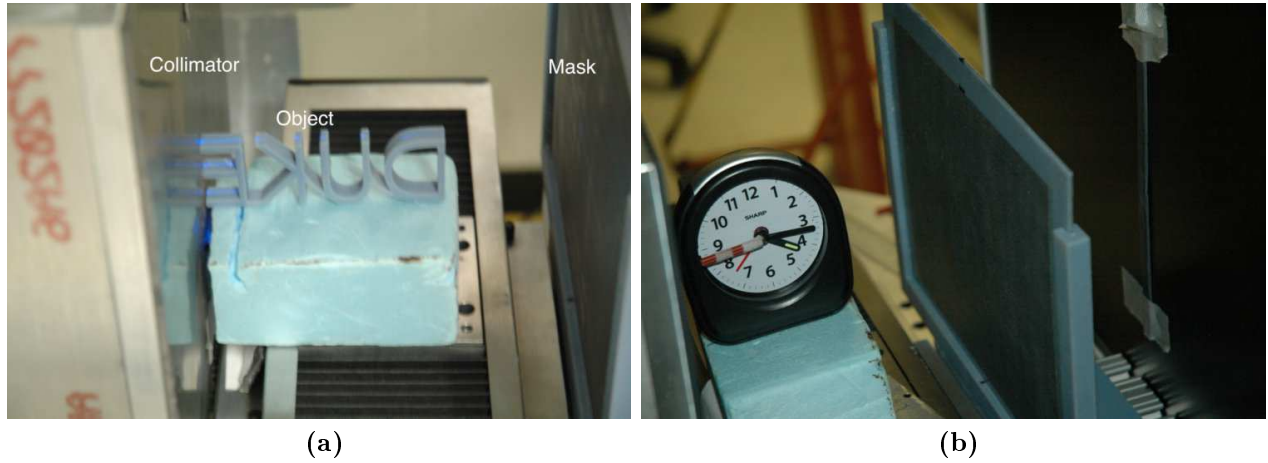


Figure 4.3: Photos of (a) plastic DUKE letters and (b) the clock in position for the experiments.

4.4 Results

Figure 4.3a shows the DUKE letters in place for the experiment, and Figure 4.4 shows the scatter image acquired for the DUKE object.

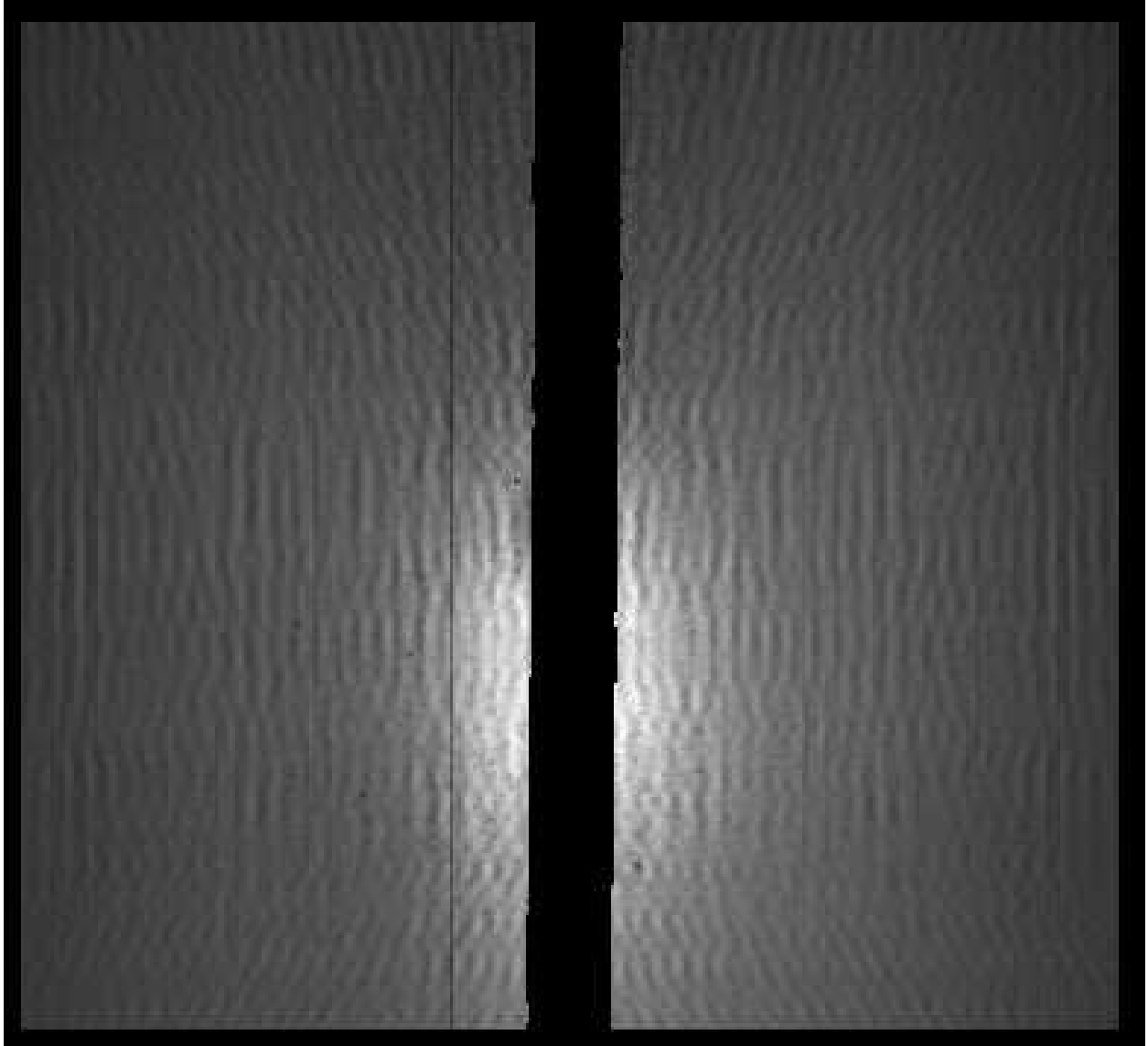


Figure 4.4: Cropped and binned scatter image for the plastic DUKE letters, corresponding to a $4.9 \text{ cm} \times 4.5 \text{ cm}$ detection area

The primary beam was blocked by a lead strip positioned on the detector, and this region has been blacked out in the image. The scatter image was binned by 3×3 pixels in software to reduce memory requirements and cropped to prevent the beam stop and pixel defects from affecting the reconstructions. Figure 4.5 shows reconstructions of the scattering density $F(x, z)$ and the scattered radiance $R(\theta)$ for this object.

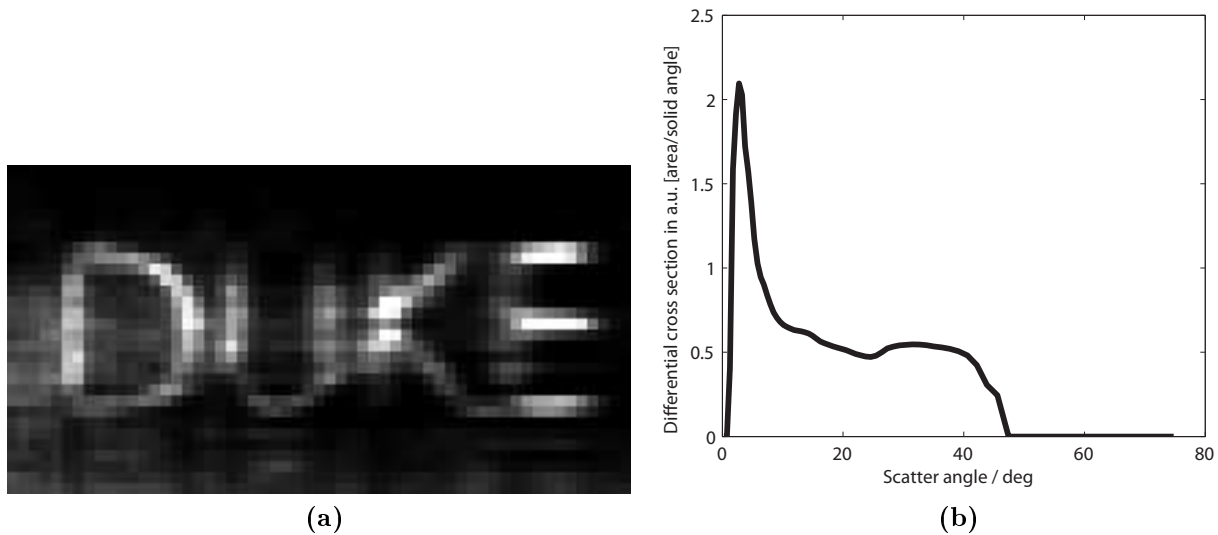


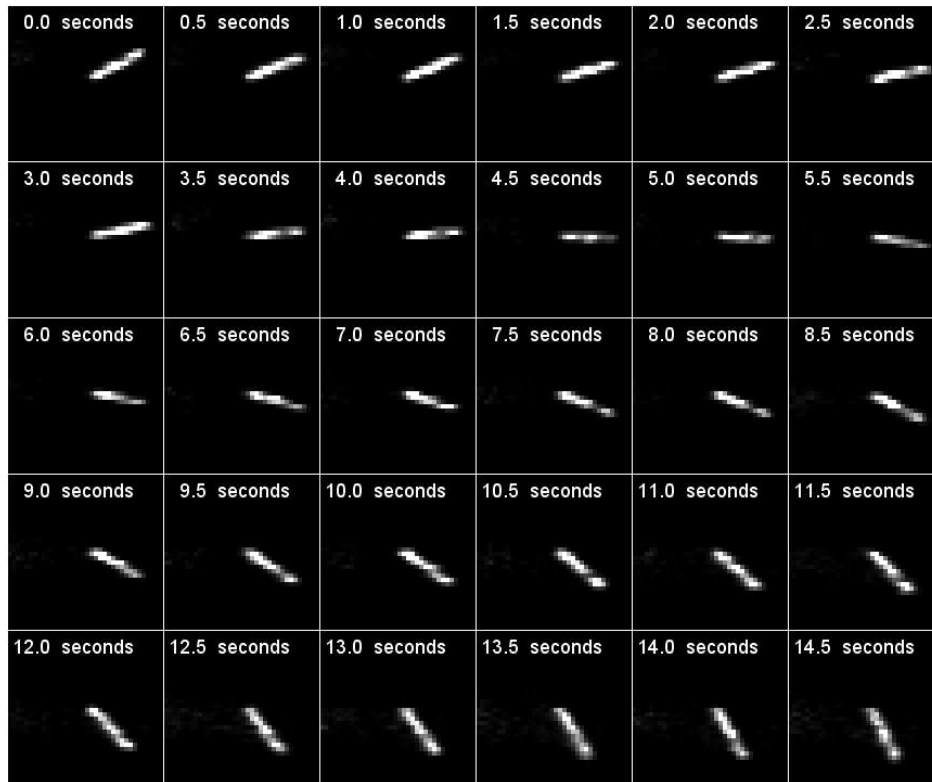
Figure 4.5: Reconstructed images for DUKE letters. (a) Density image $F(x, z)$, with $x =$ vertical and $z =$ horizontal. (b) Reconstructed scatter radiance $R(\theta)$.

Twenty iterations were run with 200 updates for $F(x, z)$ and 5 updates for $R(\theta)$ at each iteration. The density image was reconstructed with 2 mm sampling in x and z and the radiance was sampled non-uniformly with 0.5° resolution at $\theta = 0.5^\circ$ and up to 4° resolution at $\theta = 75^\circ$. The image shows recognizable letters. Blurring occurred mainly in the range direction (z) since the high-angle scatter, which carries the most range information, was relatively weak and affected by noise. The radiance consists of a low-angle coherent scatter component with a broad tail resulting from high-angle Compton scattering.

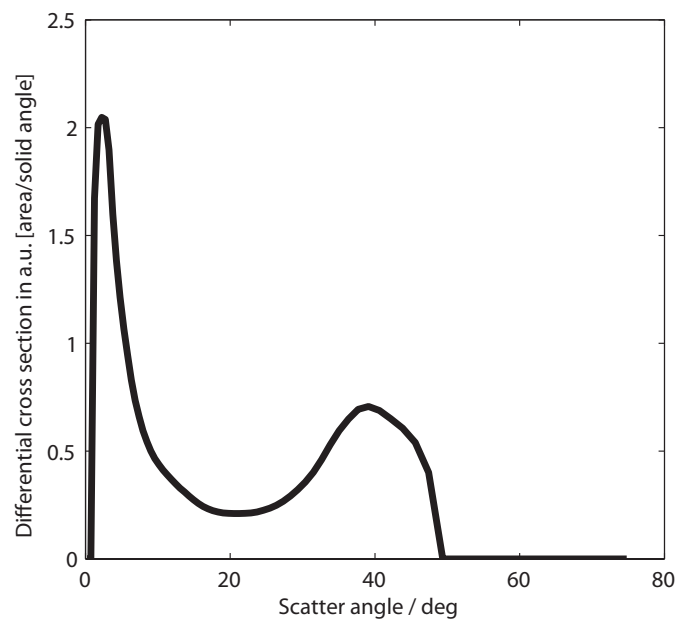
Since every snapshot produces a 2D slice of an object at one moment in time, we used the clock to demonstrate tomographic video. We positioned the clock shown in Figure 4.3b so that its second hand ticked in the plane of the beam. A strip of plastic 2 mm thick in the y direction was attached to the second hand so that it was the only object in the beam. As the hand ticked at 1 Hz, scatter images were acquired at 2 Hz. A total of 30 scatter images (not shown) were acquired over a span of 15 seconds. Each frame was used to estimate an instantaneous density image $f(x, z)$. The reconstructed frames are shown with timestamps in Figure 4.6a, and as a downloadable video file¹. The complete set of scatter images was

¹Hyperlink: <http://www.opticsinfobase.org/ao/viewmedia.cfm?uri=ao-52-19-4582&seq=1>

used to jointly estimate $R(\theta)$ for this object, shown in Figure 4.6b. We expected this curve to vary from Figure 4.5b since each object was made from a different plastic, however model error may also contribute, especially at large scatter angles due to the non-planar nature of the physical aperture.



(a)



(b)

Figure 4.6: Reconstructions of the clock's second hand. (a) Reconstructed density images $F(x, z, t)$, with $x =$ horizontal and $z =$ vertical. Each frame is labeled with the time stamp. (b) Reconstructed scatter radiance $R(\theta)$.

The resolution equations (4.10) and (4.11) show the importance of a high-resolution coded aperture. Our aperture was built with $1/u = 1.25$ mm and $1/v = 0.75$ mm with an expected resolution of $(\Delta x, \Delta z) = (2.5 \text{ mm}, 2.5 \text{ mm})$ at $z = 200$ mm. This assumes that the observable scatter image has length $Y = 120$ mm. During reconstruction, we found our 2D aperture transmission function to introduce modeling errors at high incidence angles and so we cropped the detector to $X \approx 49$ mm and $Y \approx 45$ mm. Cropping in x only narrows the transverse field of view, however cropping in y theoretically degrades the range resolution to $\Delta z = 6.7$ mm, a slight overestimate based on the reconstruction results.

4.5 Summary

These results demonstrate snapshot tomography using fan beam CAXSI. A more detailed analysis is required to explore the resolution limits and signal to noise ratio of the fan beam CAXSI system.

The range sensitivity of our aperture-detector arrangement allows us to capture forward and/or back-scatter signals, as long as the aperture and detector are placed perpendicular to the beam. This flexibility is useful when one side of the object is not accessible, or when only the forward scatter component is strong enough to measure.

The bi-linear forward model in equation (4.2) captures only the basic physics of the system. Multiple scattering effects were omitted, which include attenuation of the primary beam and scattered rays within the object. Also, a perfect irradiance detector with uniform energy response was assumed. Further, the planar coded aperture model might be replaced by more careful modeling of its 3D structure, especially for large incidence angles. The discretization via point-like sampling in space and time for each detector pixel may have introduced modeling error, and a more sophisticated scheme would include their response functions. Similar point-like sampling in the object may be replaced by other basis functions. More detailed modeling of these effects should improve the quality of the reconstructed images.

Only the coherent and incoherent scatter signals were measured to produce our results.

The reconstructions could be improved by measuring the transmitted signal in the plane of the fan beam. By measuring contributions from each type of x-ray interaction and comparing with a reference library of cross sections, fan beam CAXSI is promising for determining distributions of constituent materials within extended or dynamic objects. The effects of noise, system geometry, and acquisition settings should be studied in detail when applying these techniques to a specific application.

While a static 3D object may be translated through the fan beam to build up slices, collimation into a fan beam wastes photons. The next chapter generalizes the scale codes used here to a new family of coded apertures for cone beam scatter tomography.

CHAPTER 5: CODED APERTURES FOR VOLUME IMAGING

5.1 Background

Coded aperture imaging found early use in x-ray astronomy, where transverse 2D imaging is the goal. The Fresnel zone plates (FZP) proposed by Mertz and Young in 1961 [50], and analyzed further by Barrett and Horrigan [51], provided a way to beat the resolution-versus-throughput tradeoff of pinhole imaging. The idea was that each star projects a shadow of the FZP onto the detector plane, and these shadows are superimposed in the measured image. Each shadow exhibits a different shift determined by the position of the original star. When the measured image is developed into a transparent medium and illuminated with coherent light, each shadow acts like a lens and focuses the coherent light back to the source point, with some magnification. The result is a holographic image of the original scene. The hologram may be reconstructed optically or digitally, depending on the equipment available. The ability to perform this reconstruction is due to the orthogonality of the FZP shadows centered at different locations.

Inspired by digital processing, the URA [55] apertures developed by Fenimore and Cannon in 1978 and related MURA [56] apertures developed by Gottesman and Fenimore in 1989 are based on similar ideas about orthogonality, and possess correlational decoding arrays which produce perfect 2D point spread functions. The FZP and (M)URA codes are examples of “shift codes”, but the orthogonality relationships of these shift codes break down under magnification, which occurs when image points are located at different ranges from the detector. When applied to 3D scenes, shift codes provide some ability to “focus” the reconstruction to different depths, however the chosen slice will always be corrupted by out-of-focus planes. This effect points to a fundamental limitation of 3D tomography from

2D measurements.

The FZP method is a type of holography, where incoherent light is used to measure the image and coherent light (or a digital representation of it) is used to perform the reconstruction. By shining coherent light through the measured image, a boundary condition is created which produces the holographic image, which is often a sufficient representation of the object. A coherent optical field is bound by Maxwell's equations and is completely specified on a 2D surface, but no such constraint exists for the original object. The distinction between holography and tomography is that tomography reconstructs the radiating object, not the field. Reconstruction based on the (M)URA codes encounter the same limitation; the 2D measurement is just one realization of the optical field, while 3D tomography requires multiple measurements of the field under varying conditions.

In this chapter, a new family of coded apertures for 3D scatter or emission tomography is proposed which incorporates built-in scale orthogonality. These are termed “frequency scale codes” (FSC) and are generalizations of the sinusoid apertures of previous chapters. FSCs impose a certain relationship between spatial frequency and range, which is exploited during tomographic reconstruction. The main feature of a FSC is that it contains a unique spatial frequency in each direction. A FSC may be used in a traditional coded aperture system, where the 2D aperture is placed a distance d in front of a 2D detector array. The FSC enables direct tomographic reconstruction via Fourier analysis when the aperture-detector distance d or object-detector distance z is scanned while acquiring a sequence of images. The linear scanning motion of d or z may be more attractive for certain applications than the combination of translational and rotational scanning required for cone beam transmission tomography. Furthermore, broadband FSCs may be constructed which sparsely sample the Fourier space when the number of available exposures is limited. These codes are aligned with the ideas of compressive sampling, and will be discussed along with possibilities for adaptive sensing.

In Chapter 4, snapshot tomography was demonstrated for fan beam illumination perpendicular to a detector plane. This may be applied to volume imaging by scanning the object through the fan beam to build up the 3D image from individual slices. However, common x-ray sources do not naturally produce fan beam illumination, and therefore much of the available power is absorbed at the source-side collimators. The proposed FSC methods may employ the full cone beam, providing a significant increase in signal power as long as the primary beam can be separated from the scatter measurements. Furthermore, FSCs are applicable to emission tomography, where one cannot directly constrain the spatial domain of the emitted radiation.

5.2 Forward model

To develop the forward model for 3D scatter tomography, the object is represented by the isotropic scattering density $F(\mathbf{r}, z)$, where $\mathbf{r} = (x, y)$ and z is the distance from the detector plane. The function $F(\mathbf{r}, z)$ may also represent the emission rate of a self-radiating object at point (x, y, z) . The derivation of Reference [51] is followed, but with some changes in notation and with the z dependence retained. Here, the measured irradiance is $G(\mathbf{r})$, $H(\mathbf{r})$ is the transmittance of the aperture, and the Fourier transformed versions are indicated by a tilde ($\tilde{}$). As in Reference [51], only first-order scattering effects are considered to develop a linear forward model, approximating weakly attenuating or scattering objects. For strongly attenuating or scattering objects, the linear model may be applied iteratively as differential corrections to the estimated $F(\mathbf{r}, z)$ until convergence is achieved.

Define the magnification $m(z) = z/(z - d)$ of the aperture shadow as projected from distance z . In the paraxial case, the propagation distance is approximately z . The forward model relates the scattering density $F(\mathbf{r}, z)$ to the measured irradiance $G(\mathbf{r}')$:

$$G(\mathbf{r}') = \int \frac{dz}{z^2} \int d\mathbf{r} F(\mathbf{r}, z) H(\mathbf{r} + [\mathbf{r}' - \mathbf{r}]/m) \quad (5.1)$$

Taking the 2D spatial Fourier transform of G with respect to \mathbf{r}' ,

$$\begin{aligned}
\tilde{G}(\mathbf{k}) &= \int \frac{dz}{z^2} \int d\mathbf{r} F(\mathbf{r}, z) \int d\mathbf{r}' e^{-2\pi i \mathbf{k} \cdot \mathbf{r}'} H(\mathbf{r} + [\mathbf{r}' - \mathbf{r}]/m) \\
&= \int \frac{dz}{z^2} \int d\mathbf{r} F(\mathbf{r}, z) m e^{2\pi i \mathbf{k} \cdot \mathbf{r}(m-1)} \tilde{H}(\mathbf{k}m) \\
&= \int \frac{mdz}{z^2} \tilde{F}(\mathbf{k}[1-m], z) \tilde{H}(\mathbf{k}m)
\end{aligned} \tag{5.2}$$

The aperture acts as a scaled transfer function for each z slice of the object, but with the complication of the z integral which superimposes the different planes. The goal of tomography is to completely separate these slices.

A careful look at (5.2) reveals that the measured frequency \mathbf{k} contains information about object frequency $\mathbf{k}(1-m) = \mathbf{k}d/(d-z)$ in each slice z . The aperture must contain frequency $\mathbf{k}m = \mathbf{k}z/(z-d)$ in order for the object frequency $\mathbf{k}d/(d-z)$ at range z to be transmitted. If the aperture has a single frequency, then each measured frequency will be mapped to a different spatial frequency at each range. Consider a single frequency aperture with the Fourier transform:

$$\tilde{H}(\mathbf{k}) = \delta^2(\mathbf{k} - \mathbf{u}) \tag{5.3}$$

with δ^2 being the 2D Dirac delta function. Incoherent imaging requires H to be real-valued between zero and one, so (5.3) should contain a component at $-\mathbf{u}$ and a zero frequency component. But upon inverse Fourier transformation, the expression (5.3) would produce a complex valued H . A complex H may be synthesized using balanced detection, meaning measuring once with an aperture containing a cosine dependence and another containing a sine dependence. Assuming balanced detection, the single frequency in (5.3) is justified. Plugging (5.3) into (5.2),

$$\begin{aligned}
\tilde{G}(\mathbf{k}') &= \int \frac{mdz}{z^2} \tilde{F}(\mathbf{k}'[1-m], z) \delta^2(m\mathbf{k}' - \mathbf{u}) \\
&= \int \frac{mdz}{z^2} \tilde{F}(\mathbf{k}'[1-m], z) \frac{1}{k'u} \delta\left(m - \frac{u}{k'}\right) \delta(k'_\phi - u_\phi)
\end{aligned} \tag{5.4}$$

with the delta function expanded intermediately as $\delta^2(m\mathbf{k}' - \mathbf{u}) = \frac{1}{u} \delta(mk' - u) \delta(k_\phi - u_\phi)$. The variables k and k_ϕ are the magnitude and polar angle for \mathbf{k} , and similarly for \mathbf{u} . The function $\delta(k'_\phi - u_\phi)$ constrains the polar angles so \mathbf{k}' is in the same direction as \mathbf{u} and we also have $\mathbf{k}' \parallel \mathbf{k}$. Transforming the integral in (5.4) from z to $m = z/(z - d)$,

$$\begin{aligned} \tilde{G}(\mathbf{k}') &= -\frac{1}{k'ud} \delta(k'_\phi - u_\phi) \int \frac{dm}{m} \tilde{F}(\mathbf{k}'[1 - m], z) \delta\left(m - \frac{u}{k'}\right) \\ &= -\frac{1}{u^2d} \delta(k'_\phi - u_\phi) \tilde{F}\left(\mathbf{k} = \mathbf{k}' - \mathbf{u}, z = \frac{ud}{u - k'}\right) \end{aligned} \quad (5.5)$$

To invert (5.5), note that $\mathbf{k}' = \mathbf{k} + \mathbf{u}$ and \mathbf{k}' is in the same direction as \mathbf{u} with a smaller magnitude. This means that the object frequency has magnitude $k = u - k'$. Figure 5.1 shows how the object frequency \mathbf{k} at range z transforms to the measured frequency \mathbf{k}' .

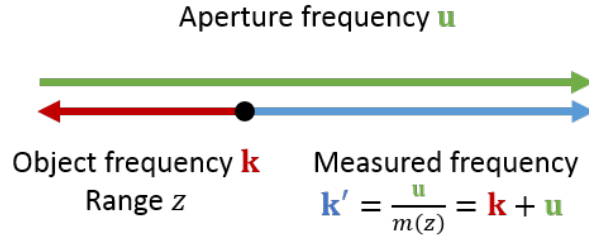


Figure 5.1: Relationship between the object frequency \mathbf{k} at range z , the aperture frequency \mathbf{u} , and the measured frequency $\mathbf{k}' = \mathbf{u}/m(z) = \mathbf{k} + \mathbf{u}$.

Equating $\mathbf{k}' = \mathbf{u}/m(z) = \mathbf{k} + \mathbf{u}$, it becomes evident that to measure the object point (\mathbf{k}, z) the aperture frequency u and distance d must satisfy $d = \frac{kz}{u}$. Inverting (5.5) for \tilde{F} , the reconstruction is

$$\tilde{F}\left(\mathbf{k} = -\frac{\mathbf{u}d}{z}, z\right) = -u^2d \tilde{G}\left(\mathbf{k}' = \mathbf{u} \left[1 - \frac{d}{z}\right]\right) \quad (5.6)$$

The reconstruction is only defined along the 1D curve $\mathbf{k}(z) = -\mathbf{u}d/z$ in the object space. Object points at different ranges are measured as different frequency components on the detector. This was the concept behind the sinusoidal scale codes of Chapters 2-4. The entire object space may be reconstructed by scanning the aperture frequency \mathbf{u} , however dynamic

apertures are difficult to implement. Instead, one may vary d or z to achieve the same effect as scaling the magnitude of \mathbf{u} . Rotational scanning is also necessary to reconstruct frequency components in all directions, unless a code with multiple frequencies is used, as described in the next section.

The reconstructed spatial frequency at range z is $k = \frac{ud}{z}$, giving transverse spatial resolution $\Delta x \approx \frac{z}{ud}$. When scanning these parameters, the combination of u , d , and z which minimizes Δx should be used to estimate the resolution. The range resolution was previously derived in Chapter 2 for a code with frequency u to be $\Delta z \approx \frac{z^2}{Dud} = \Delta x \frac{z}{D}$, where D is the diameter of the detector. The range uncertainty is based on the ability to resolve the frequency of the magnified aperture over a finite area. In practice, measurement quantization will also contribute to the achievable resolution.

5.3 Frequency scale codes (FSC)

As shown in the previous section, a single frequency aperture allows reconstruction of a 1D curve in the object's space (\mathbf{k}, z) . Codes with multiple frequencies could be envisioned if ambiguities in frequency and range could be prevented. Note that in Figure 5.1 all three vectors are parallel or anti-parallel, so that the aperture may include frequencies in multiple directions without introducing ambiguity since they occupy separate subspaces. This motivates the definition of a frequency scale code (FSC) as a pattern which contains a unique spatial frequency in each direction. A good FSC should not only include the proper frequency structure, but should also allow high throughput.

The simplest FSC is proposed here as producing a ring in Fourier space. The aperture is parameterized by the radius u of the ring and only 1D scanning of u , d , or z is required to reconstruct the 3D object. Such an aperture was mentioned in Chapter 2 and is based on the transmittance

$$H(\rho, \phi) = \frac{1 + \cos(2\pi u\rho + n\phi)}{2} \quad (5.7)$$

where ρ is the polar radius in the aperture plane and ϕ is the polar angle. The “ring” aperture is plotted for $u, n = 1$ along with its discrete Fourier transform (DFT) in Figure 5.2.

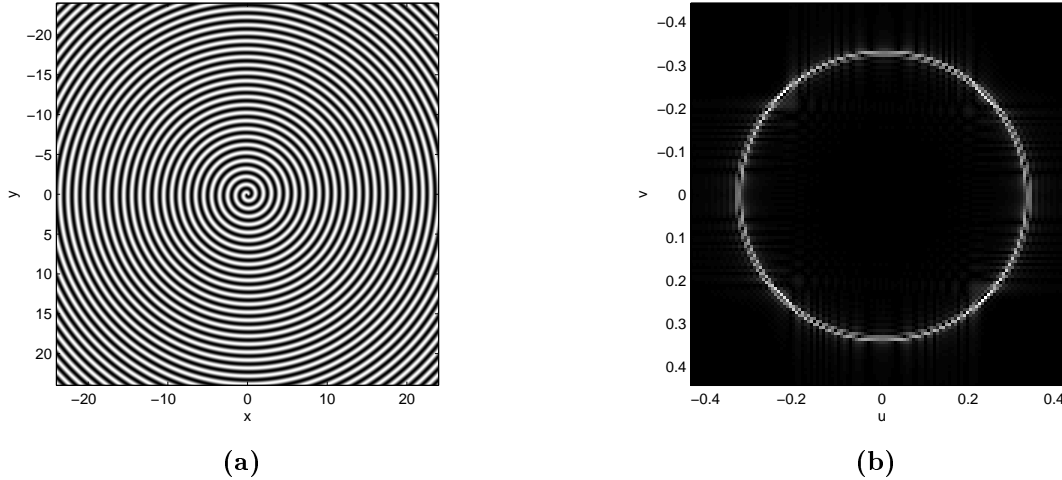


Figure 5.2: Coded aperture for volume tomography based on a ring structure in frequency (Equation (5.7)): (a) the aperture in physical space and (b) the magnitude of its DFT showing a unique frequency in each direction. The DC component was removed for clarity, and the modulations around the ring are a result of using a real-valued H .

With the “ring” aperture, a surface of revolution in the (\mathbf{k}, z) space is measured by each exposure of the 2D detector array. These surfaces are illustrated in Figure 5.3 and follow from $k = ud/z$. They show how the object space may be filled out by varying ud . If the object is translated in z , the surface of revolution will accordingly shift in z .

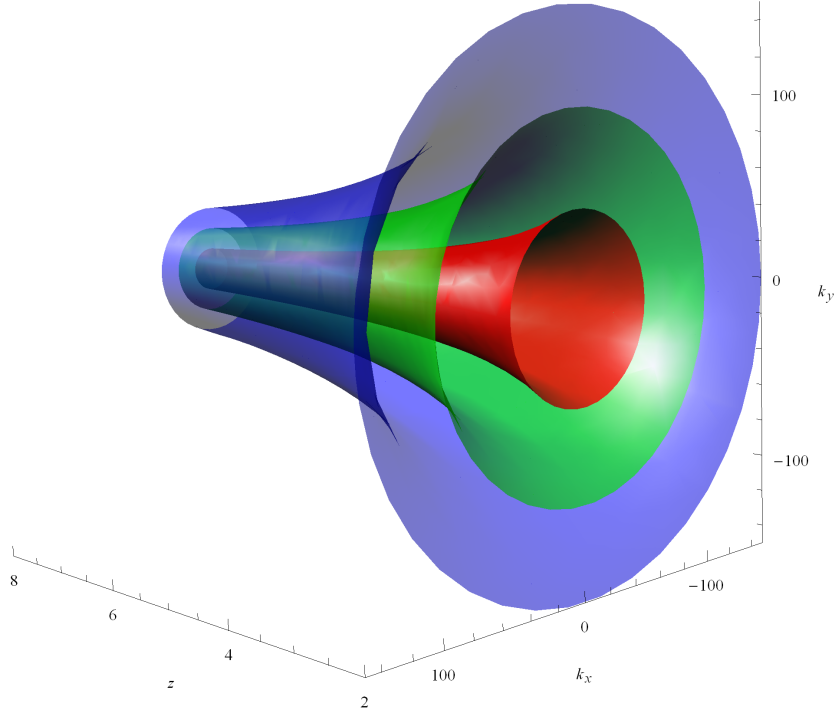


Figure 5.3: Three surfaces in the object space, each measurable by a 2D snapshot with the “ring” FSC. The surfaces are defined by $|\mathbf{k}| = ud/z$. The coordinates k_x and k_y are the components of the transverse spatial frequency \mathbf{k} , and the units assume $d = 1$. Three values of ud are shown: $ud = 100$ (red), 200 (green) and 300 (blue).

To qualify as a FSC, \tilde{H} may contain any curve with a unique frequency in each direction. A choice which produces a spiral in the frequency domain is closely related to the DCT aperture of Chapter 2 but with reflection symmetry:

$$H(\rho, \phi) = \frac{1 + \cos(2\pi u \rho \bmod(\phi, \pi))}{2} \quad (5.8)$$

where $\bmod(\phi, \pi) = \phi - n\pi$ and n is the largest integer such that $\phi \geq n\pi$. This code is plotted for $u = 1$ in Figure 5.4 along with its DFT. These FSCs, and others, enable direct tomographic reconstruction by removing the ambiguity between spatial frequency and range.

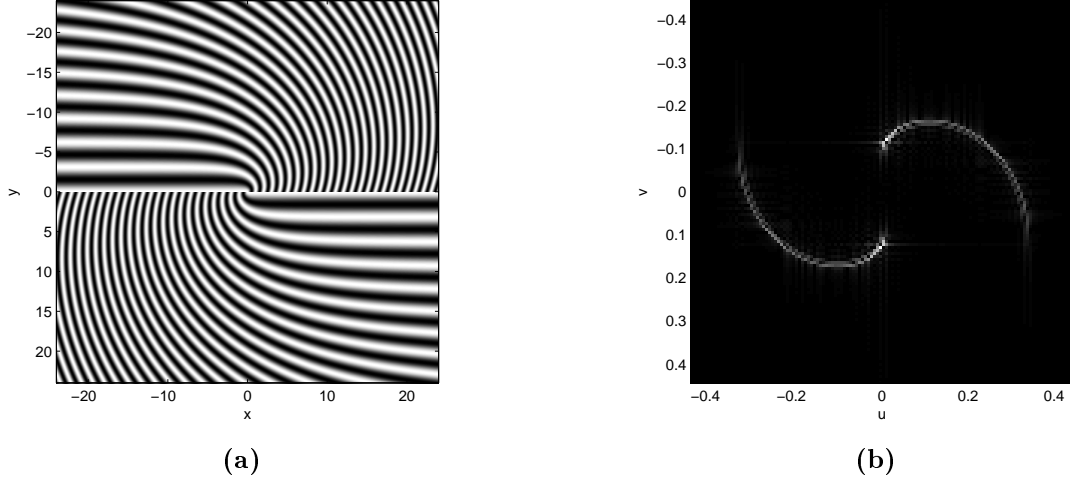


Figure 5.4: Coded aperture for volume tomography based on a spiral structure in frequency (Equation (5.8)): (a) the aperture in physical space and (b) the magnitude of its DFT showing a unique frequency in each direction. The DC component was removed for clarity, and the modulations along the curve are a result of using a real-valued H .

5.4 Scanning techniques

The distances d and/or z may be scanned to fill out the object space, instead of changing the aperture pattern which is difficult in practice. A simple approach uses a static FSC code where the distance d is varied. In this case, let $\tilde{G}(\mathbf{k}, d)$ be the 2D spatially Fourier transformed measurements for aperture position d . Assume the “ring” frequency structure $\tilde{H}(\mathbf{k}) = \frac{1}{2\pi u} \delta(k - u)$. With this in (5.2), equation (5.6) becomes

$$\tilde{G}(\mathbf{k}', d) = -\frac{1}{2\pi u^2 d} \tilde{F}\left(\mathbf{k} = \mathbf{k}' \left(1 - \frac{u}{k'}\right), z = \frac{ud}{u - k'}\right) \quad (5.9)$$

For the measurement containing information about $\tilde{F}(\mathbf{k}, z)$, the aperture must have been at position $d = kz/u$. Manipulating $\mathbf{k} = \mathbf{k}' \left(1 - \frac{u}{k'}\right)$ in (5.9), object frequency \mathbf{k} at slice z is found at measurement frequency $\mathbf{k}' = \mathbf{k} \left(1 - \frac{z}{d}\right)$. Using the known d ,

$$\tilde{F}(\mathbf{k}, z) = -2\pi u k z \tilde{G}\left(\mathbf{k}' = \mathbf{k} \left(1 - \frac{u}{k}\right), d = \frac{kz}{u}\right) \quad (5.10)$$

which provides the reconstruction method for a moving aperture.

If the object is translated relative to the aperture-detector apparatus, the sequence $\tilde{G}(\mathbf{k}, z_{off})$ is acquired, where z_{off} is the offset of the object relative to its initial position. Information about $\tilde{F}(\mathbf{k}, z)$ is found from the measurement at $z_{off} = \frac{ud}{k} - z$. The inversion resembles (5.10):

$$\tilde{F}(\mathbf{k}, z) = -2\pi u^2 d \tilde{G}\left(\mathbf{k}' = \mathbf{k}\left(1 - \frac{u}{k}\right), z_{off} = \frac{ud}{k} - z\right) \quad (5.11)$$

Equation (5.11) is the inversion formula when moving the object relative to the aperture/detector apparatus. This approach is very promising for a variety of applications, where the object is linearly translated and the scanner itself requires no moving parts.

5.5 Compressive sampling

Compressive tomography is a process by which an object embedded in N dimensional space is reconstructed from measurements embedded in less than N dimensions. Conventional transmission tomography as well as the scatter techniques discussed above trade time for the missing dimension(s). In Reference [77], compressive sampling and reconstruction strategies are shown to maintain image quality as the measurements are sub-sampled in various ways for transmission tomography. It is expected that similarly encouraging results will be found when scatter tomography is analyzed in the context of compressed sensing. If enough prior information is known about the object, then 3D tomography may be possible in the extreme case of acquiring a single 2D snapshot. For this purpose one might design a FSC with a quickly varying frequency as a function of direction in order to sparsely sample the object's entire Fourier space, keeping in mind that the frequency should be a unique function of direction. This ensures that no range ambiguity ensues since each frequency component in the code then samples a unique curve in the object space. The object basis used above consists of 2D transverse Fourier components and 1D range. In the context of compressed sensing, the Fourier basis is a great choice for imaging points while acquiring very few measurements [57]. The FSC also enables measurement of individual frequency

components in the object, and as a result the sensing process may be tailored for specific object classes.

CHAPTER 6: ENERGY SENSITIVE CAXSI

6.1 Background

The previous chapters focused on energy-integrating detectors, where the total irradiance is measured by each pixel, with some quantum efficiency determined by the x-ray wavelength. Energy sensitive detectors, in contrast, measure the spectral composition of the x-rays which provides additional information about coherent scatter events via Bragg's law. This is achieved in solid state devices by measuring the height of the current pulse produced from each absorbed photon in a semiconductor. In Chapter 2, coded apertures were presented for pencil beam scattering experiments and the resulting singular values were compared. In the following, this analysis is extended to linear arrays of energy sensitive detectors, such as those used in the experimental demonstration of energy sensitive CAXSI in Reference [35].

The anisotropic scattering model of Chapter 2 reconstructs an object's scattering density $f(z, \theta)$, where z is the distance along the pencil beam and θ is the scattering angle. This model is applicable to coherently scattering objects if one considers a mono-energetic beam at energy E . Then, the scattering density as a function of momentum transfer is $F(z, q) = f(z, \theta = 2 \sin^{-1} \frac{qc}{2E})$. If the beam is broadband, recovering $F(z, q)$ from $f(z, \theta)$ is limited by the fact that photons at multiple energies (and therefore multiple q values) contribute to each θ . Thus, energy sensitive detectors are desirable since they effectively remove this ambiguity by sorting the detected photons according to distinct energy channels.

In the following, the pencil beam CAXSI system of Chapters 2 and 3 is analyzed for the case of energy sensitive detectors. Figure 6.1 shows the basic geometry.

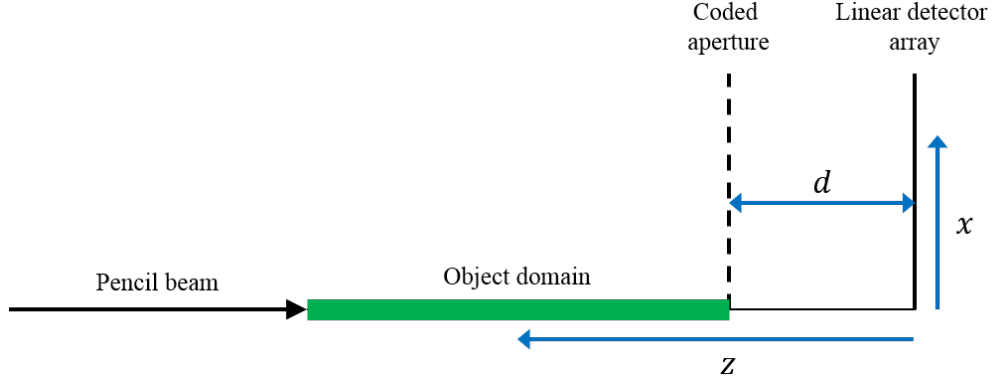


Figure 6.1: Pencil beam system geometry considered for energy sensitive CAXSI.

The aperture plane is parallel to the detector array and separated by distance d . The forward model relates the object's scattering density $F(z, q)$ to the measured field $G(x, E)$:

$$G(x, E) = \int_d^{z_{max}} \frac{A \cos \theta dz}{x^2 + z^2} T\left(\frac{x}{m(z)}\right) F\left(z, q = \frac{2E}{c} \sin \frac{\theta}{2}\right) \quad (6.1)$$

where z is measured from the detector plane, x is the measurement position within the detector plane, and E is the measured photon energy. The energy spectrum is assumed to be perfectly flat, or otherwise corrected for in the measurements. The factor $\frac{A \cos \theta}{x^2 + z^2}$ is the solid angle subtended by the area element A facing the z direction at detector position x , as viewed from the position z along the pencil beam. In the following, A will be ignored, rendering (6.1) valid up to a proportionality. The function $T(x)$ is the transmittance of the aperture, assumed to be independent of energy, and $m(z) = z/(z - d)$ is the magnification of the aperture relative to the point z . For simplicity, only quantization in E is considered so that the measurements can be represented as $G_i(x)$, for energy bin $i = 1 \dots N$. This is a useful model since many x-ray detectors have high spatial resolution and little or no energy resolution. Letting $\eta_i(E)$ be the quantum efficiency of bin i , the forward model is

$$G_i(x) = \int dE \eta_i(E) G(x, E) \quad (6.2)$$

For simplicity, only small angle scattering is considered, which generally applies to high

energy coherent scatter experiments. In this limit, $\cos \theta \approx 1$, $x^2 + z^2 \approx z^2$, and $\theta \approx x/z$. Bragg's law becomes simply $zq = Ex/c$. This is worth examining; each photon lands at a specific (E, x) pair. One would like to find its origin in (z, q) , but Bragg's law only provides us the product zq . The coded aperture is necessary to determine z , which in turn resolves q [35].

6.2 Resolution analysis

The impulse response is found by inserting the impulse $F(z, q) = \delta(z - z_0) \delta(q - q_0)$ into (6.1) and using (6.2):

$$\begin{aligned} H_i(x; z_0, q_0) &= \int dE \eta_i(E) \int \frac{dz}{z^2} T\left(\frac{x}{m(z)}\right) \delta(z - z_0) \delta\left(q_0 - \frac{Ex}{zc}\right) \\ &= \left(\frac{c}{z_0 x}\right) T\left(\frac{x}{m(z_0)}\right) \eta_i\left(\frac{z_0 q_0 c}{x}\right) \end{aligned}$$

The point spread function (PSF) is the correlation of the impulse responses from two neighboring points in the object space:

$$\begin{aligned} PSF(z_1, q_1; z_0, q_0) &= \sum_i \int dx H_i(x; z_1, q_1) H_i(x; z_0, q_0) \\ &= \frac{c^2}{z_0 z_1} \int \frac{dx}{x^2} T\left(\frac{x}{m(z_1)}\right) T\left(\frac{x}{m(z_0)}\right) \sum_i \eta_i\left(\frac{z_1 q_1 c}{x}\right) \eta_i\left(\frac{z_0 q_0 c}{x}\right) \end{aligned} \quad (6.3)$$

The simplest model for an energy sensitive detector partitions the photon energy E into equally spaced, non-overlapping bins of width and separation ΔE . The quantum efficiency of bin i is $\eta_i(E) = \text{rect}\left(\frac{E}{\Delta E} - i\right)$, where $\text{rect}(\dots)$ is a unit square pulse ($\text{rect}(x) = 1$ for $|x| \leq \frac{1}{2}$, and $\text{rect}(x) = 0$ otherwise). The sum over energy bins in (6.3) can be re-written as $\text{rect}\left(\frac{z_1 q_1 - z_0 q_0}{x \Delta E / c}\right)$. This constrains contributing values of x to the integral in (6.3) to those satisfying $x > \frac{c|z_1 q_1 - z_0 q_0|}{2\Delta E}$. The detector subtends the range $x \in [x_{min}, x_{max}]$ with $x > 0$ and

total length $D = x_{max} - x_{min}$. The PSF is

$$PSF(z_1, q_1; z_0, q_0) = \frac{c^2}{z_0 z_1} \int_{x_{min}}^{x_{max}} \frac{dx}{x^2} T\left(\frac{x}{m(z_1)}\right) T\left(\frac{x}{m(z_0)}\right) \text{rect}\left(\frac{z_1 q_1 - z_0 q_0}{x \Delta E / c}\right) \quad (6.4)$$

This function is plotted for no aperture ($T(x) = 1$) and a sinusoid aperture ($T(x) = \frac{1+\sin(2\pi ux)}{2}$) in Figure 6.2. These figures illustrate the ambiguities in (z, q) and the necessity for the coded aperture. Both PSFs are extended along the curve $zq = \text{const}$, however the sinusoid code produces an absolute maximum at $z_1 = z_0$, providing sensitivity to the z coordinate. The range resolution for a sinusoid code was previously derived in Chapter 2 to be $\Delta z \approx z^2 / (Dud)$, where u is the spatial frequency of the coded aperture [33].

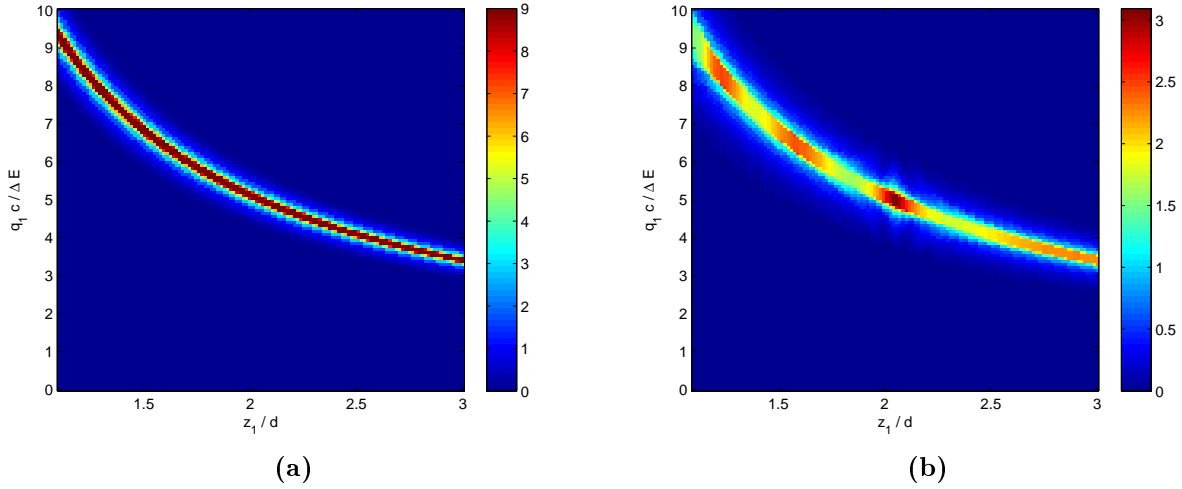


Figure 6.2: Plots of the PSF for $(z_0, q_0) = (2.05d, 1.5\Delta E/c)$ and varying (z_1, q_1) . The transmittance functions are (a) $T(x) = 1$, and (b) $T(x) = \frac{1+\sin(2\pi ux)}{2}$. The point (z_0, q_0) lies at the center of each image. The PSFs are extended along the curve $zq = \text{const}$, however the sinusoid code in (b) produces an absolute maximum at $z_1 = z_0$, providing distinguishability between points at different ranges. Values used were $ud = 50$ and $x_{max} = d$.

Because the energy response sets a lower bound on the x coordinate via the $\text{rect}(\dots)$ function, the PSF completely vanishes when $\frac{c|z_1 q_1 - z_0 q_0|}{2\Delta E} \geq x_{max}$. At constant $z = z_0 = z_1$, the width of the PSF in q is

$$\Delta q_{max} = \frac{4x_{max}\Delta E}{cz} \quad (6.5)$$

The expression (6.5) is an upper bound for the momentum transfer resolution at constant z . Ignoring the transmittance function T in (6.4) for a moment, the $1/x^2$ dependence means that the PSF decays quickly for $\frac{c|z_1q_1-z_0q_0|}{2\Delta E} > x_{min}$, and it plateaus for $\frac{c|z_1q_1-z_0q_0|}{2\Delta E} \leq x_{min}$. The width of the plateau region is

$$\Delta q_{min} = \frac{4x_{min}\Delta E}{cz}$$

which is a lower bound for the momentum transfer resolution, since momentum transfer values within this range produce maximally correlated measurements. In practice, x_{min} will be limited by two factors: first, the ability to separate the scatter signal from the primary beam, and second, the maximum energy of the primary beam. Focusing on the latter, consider an energy spectrum with the range $E \in [E_{min}, E_{max}]$. For a given (z, q) , the scatter signal lies in the range $x \in zqc \left[\frac{1}{E_{max}}, \frac{1}{E_{min}} \right]$. Assuming the minimum x lands on the detector, the momentum transfer resolution for a beam with finite energy range is

$$\Delta q_{min} = 4q \frac{\Delta E}{E_{max}} \tag{6.6}$$

This expression shows that the relative uncertainty in momentum transfer is closely related to the energy resolution of the detector and maximum detectable energy of the x-ray source.

6.3 Simulations

The PSF and resolution from the previous section assumed a perfectly flat x-ray spectrum and a perfectly planar coded aperture. In this section a more sophisticated model including a realistic x-ray spectrum and a 3D coded aperture is studied using numerical simulations. The linear detector array lies at $z = 0$ and covers the transverse coordinates $x = 0$ to $x = d$, where $d = 128$ mm. The array consists of 512 pixels with pitch 0.25 mm. The aperture plane is centered at $z = d$ and the object subtends the range $z = d$ to $z = 2d$. The object is pixelated with 128 samples in z and 128 samples in momentum transfer from $q = 0$ to

16 keV/c. The x-ray source is placed at $z = 4d$ and produces an infinitely thin pencil beam along the z axis.

The forward model described by equations (6.1) and (6.2) was discretely sampled for the simulations, with two modifications. First, a realistic x-ray spectrum was included, consisting of a Bremsstrahlung component and characteristic lines from a tungsten anode. The spectrum is plotted in Figure 6.3 and was computed using the graphical version of SpekCalc 1.1 [78–80], with default settings except an energy range of 20 keV to 148 keV in 1 keV intervals. The spectral density was included as an additional factor $N(E)$ outside the integral in equation (6.1). In the following, this function $N(E)$ is referred to as simply the “tungsten spectrum”.

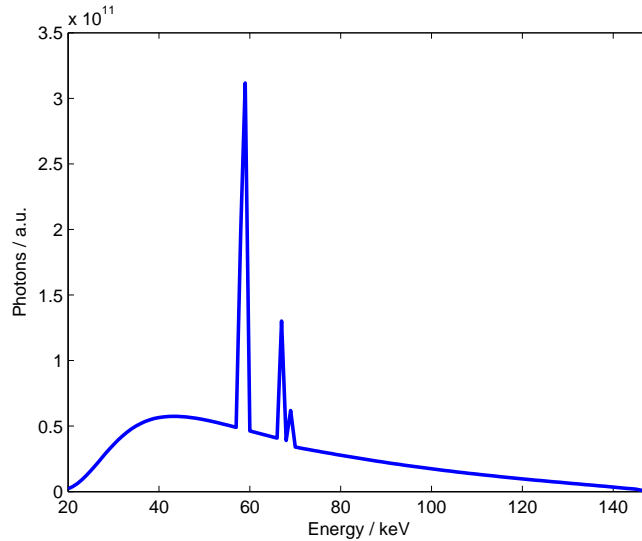


Figure 6.3: SpekCalc model for the incident spectral number density $N(E)$ from a tungsten anode at 148 kVp.

The second modification to the forward model was a more sophisticated description of the coded aperture. The aperture was modeled as a periodic array of lead blocks of width 0.5 mm in x and z with a duty cycle of 50%. Scattered rays were computed for each pair of object and detector pixels. The intersections of these rays with the lead blocks were computed using the ray tracing algorithm described in Reference [81]. This resulted in partial attenuation of certain rays as they grazed the lead features. For each ray, the

attenuation was evaluated from 20 keV to 148 keV in intervals of 0.1 keV using the NIST XCOM database entry for lead [38]. These calculations effectively replaced $T\left(\frac{x}{m(z)}\right)$ with a more complicated transmittance $T(x, z, E)$ in (6.1).

To study the effect of energy resolution, the interval $E \in [20, 148]$ keV was divided into a number n of equally spaced energy bins. In the following sections, system metrics are analyzed as they depend on n and the structure of the coded aperture. For illustration, Figure 6.4 plots the impulse response for the point $(z, q) = (192 \text{ mm}, 8 \text{ keV}/c)$ with $n = 4$ energy bins. The measurements are a transformed version of the incident energy spectrum, modulated by the periodic aperture.

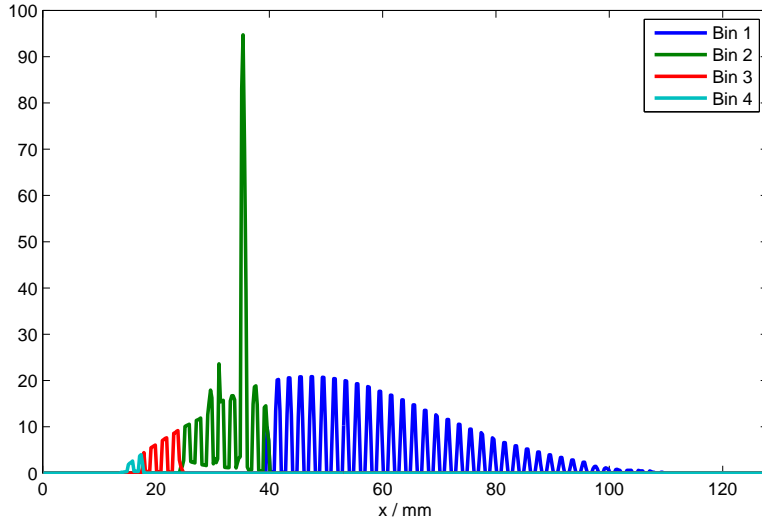


Figure 6.4: Impulse response for the object point $(z, q) = (192 \text{ mm}, 8 \text{ keV}/c)$ with $n = 4$ energy bins.

The structure of the incident energy spectrum becomes important when the detector’s energy resolution is poor. Consider the case of $n = 1$ energy bin, with $\Delta E = 128 \text{ keV}$. The PSFs for this case are shown in Figure 6.5, comparing a flat spectrum with the tungsten spectrum. For fixed z , the structure of the PSF along q is related to the scale-correlation of the incident spectrum. In Figure 6.5a, a flat spectrum was used and the PSF shows weak dependence on q , and therefore provides poor resolution in momentum transfer. In Figure 6.5b, the tungsten spectrum was used which introduces a strong dependence on q . This

was the motivation for applying spectral filtering to narrow the incident energy distribution in Chapter 3. Note, however, that in Figure 6.5b there are now multiple maxima along z , hinting that the improved q sensitivity with the tungsten spectrum comes at some cost.

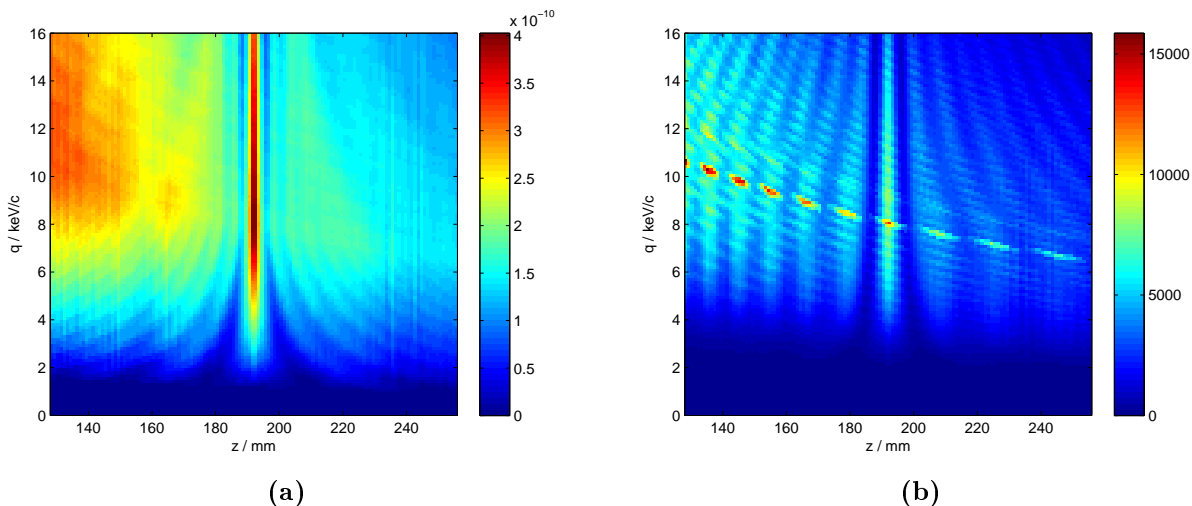


Figure 6.5: Plots of the PSF for $(z, q) = (192 \text{ mm}, 8 \text{ keV}/c)$ and a single energy bin ($n = 1$). The energy spectrum in (a) was flat from $E = 20 \text{ keV}$ to 148 keV and in (b) the tungsten spectrum was used (Figure 6.3).

6.4 SVD analysis

In the spirit of Chapter 2, this section includes SVD results for the pencil beam system using energy sensitive detectors. In particular, the dependence of the singular value distribution on the detector energy resolution and coded aperture design is presented. In discretizing the forward model defined by equations (6.1) and (6.2), discretization proceeded as in the previous section but with minimum q value increased from 0 to 2 keV/ c to avoid numerical singularities. The resulting forward matrix \mathbf{H} was calculated and its SVD was computed in Matlab according to $\mathbf{H} = \mathbf{U}\mathbf{S}\mathbf{V}^\dagger$ (the SVD is described in Section 1.6 of Chapter 1). Figure 6.6 shows the computed singular value spectra for $n = 1, 2, 4, 8, 16, 32,$ and 64 energy bins, corresponding to $\Delta E = 128, 64, 32, 16, 8, 4,$ and 2 keV , respectively. The plot uses a logarithmic scale on the vertical axis for clarity.

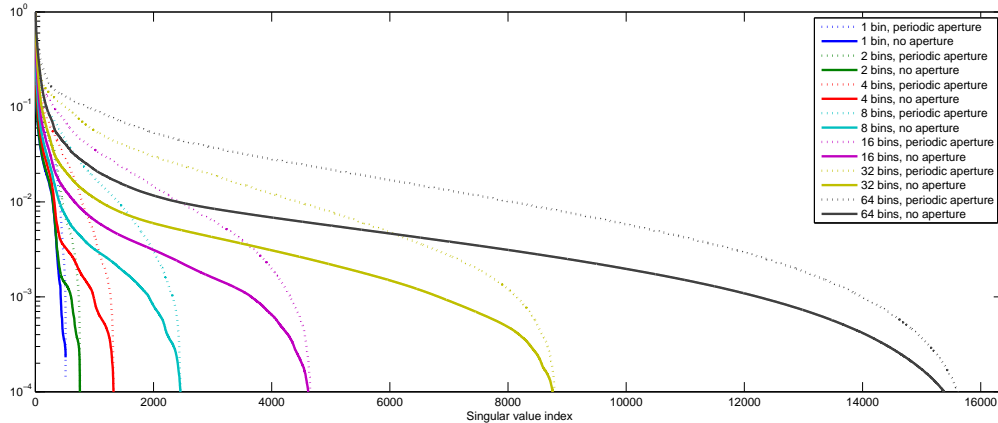


Figure 6.6: Singular value spectra for $n = 1, 2, 4, 8, 16, 32,$ and 64 energy bins, corresponding to $\Delta E = 128, 64, 32, 16, 8, 4,$ and 2 keV, respectively. For each detection scheme, the SVD was computed for the periodic aperture (dotted lines) and the case when no aperture is present (solid lines).

The solid lines represent the case when no coded aperture is used, and the dotted lines are for the case of the periodic aperture described in the last section. Each spectrum was normalized so that the largest singular value is 1, however this did not qualitatively change the results. Two important trends are evident from the SVD spectra in Figure 6.6. First, by increasing the number of energy bins, more singular values lie above a given cutoff (10^{-4} was chosen for this plot). This is expected since the PSF narrows with respect to momentum transfer q as the energy resolution improves. More energy bins means more measurable modes. The second important trend is that the singular values increase when the periodic coded aperture is introduced. This is closely related to the aperture inducing a strong dependence of the PSF on range z .

The singular value analyst must not only consider spectra as in Figure 6.6, but also the structure of the right (object space) singular vectors. The vectors with the largest singular values will be the object structures measured with the highest fidelity in the presence of noise. For illustration, in the Figures 6.7-6.11, singular vectors are shown for $n = 1$ and $n = 16$ bins ($\Delta E = 128$ keV and 8 keV, respectively). In each figure, nine vectors are shown which are equally spaced in index over the range of singular values larger than chosen cutoff,

and “s.v.” indicates each vector’s corresponding singular value. The plot for each vector uses a color scale based on those shown in Figure 6.5, but with different minimum and maximum color values for clarity. The cutoff was chosen to be 0.01, which represents a certain noise level above which the singular vectors will be called “measurable”.

Figure 6.7 shows the vectors for $n = 1$ energy bin with no aperture (“open”). Consistent with the previous PSF calculations, these vectors are elongated along curves of constant zq and will cause blurring in these directions.

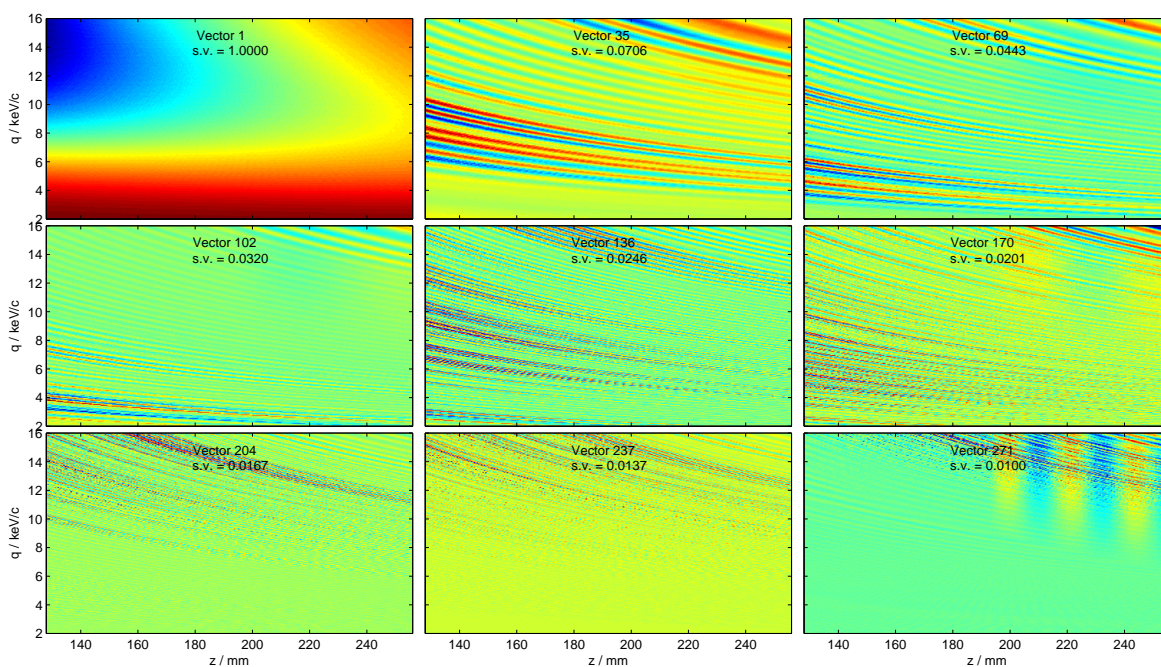


Figure 6.7: Singular vectors for $\Delta E = 128$ keV without a coded aperture.

By including the periodic coded aperture, the singular vectors become those shown in Figure 6.8. These vectors show a strong dependence on z , as expected from calculation of the PSF, and so we expect better imaging performance with the coded aperture than for the “open” case. The coded aperture works to add more measurement modes, as evidenced by having 419 vectors above the cutoff versus 273 for the open aperture. Said another way, the advantage of the coded aperture for this linear, energy-integrating detector is 1.53 times as many “measurable” modes.

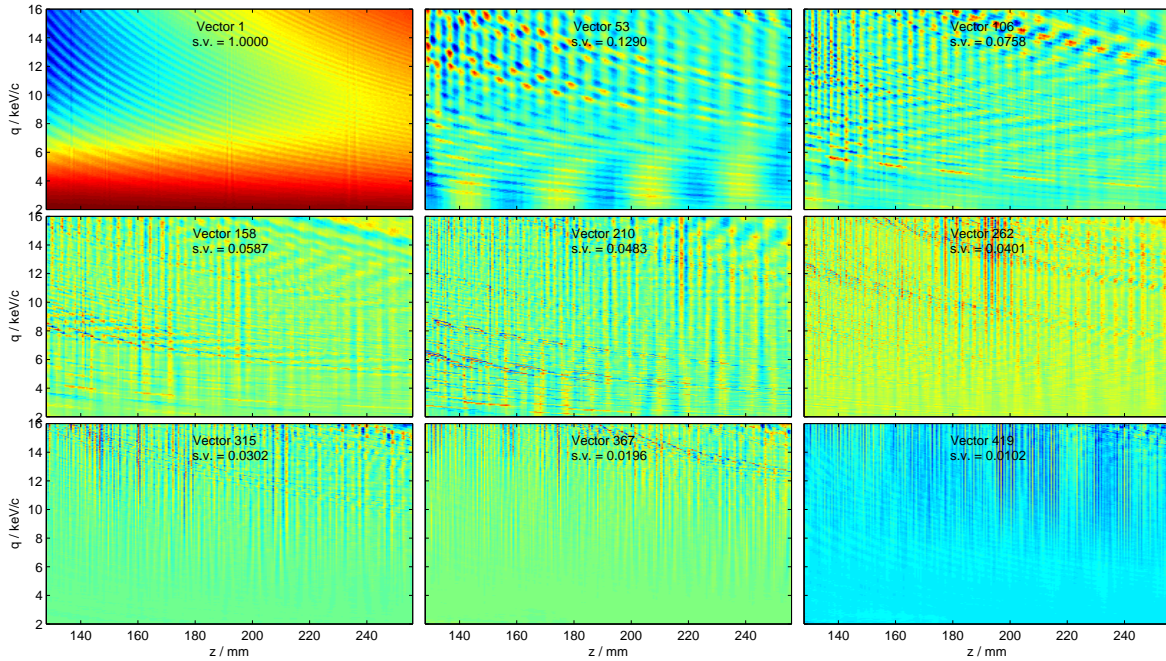


Figure 6.8: Singular vectors for $\Delta E = 128$ keV without a periodic coded aperture.

Turning now to the energy sensitive measurements with $n = 16$ energy bins ($\Delta E = 8$ keV), Figure 6.9 shows the singular vectors when no aperture is present. These vectors do not show much improvement over the case of $n = 1$ energy bin (Figure 6.7); they are still blurred along curves $zq = \text{const}$. While introducing energy resolution from $n = 1$ bin to $n = 16$ bins increased the number of measurements by a factor of 16, the number of singular vectors above the cutoff only doubled for the open aperture.

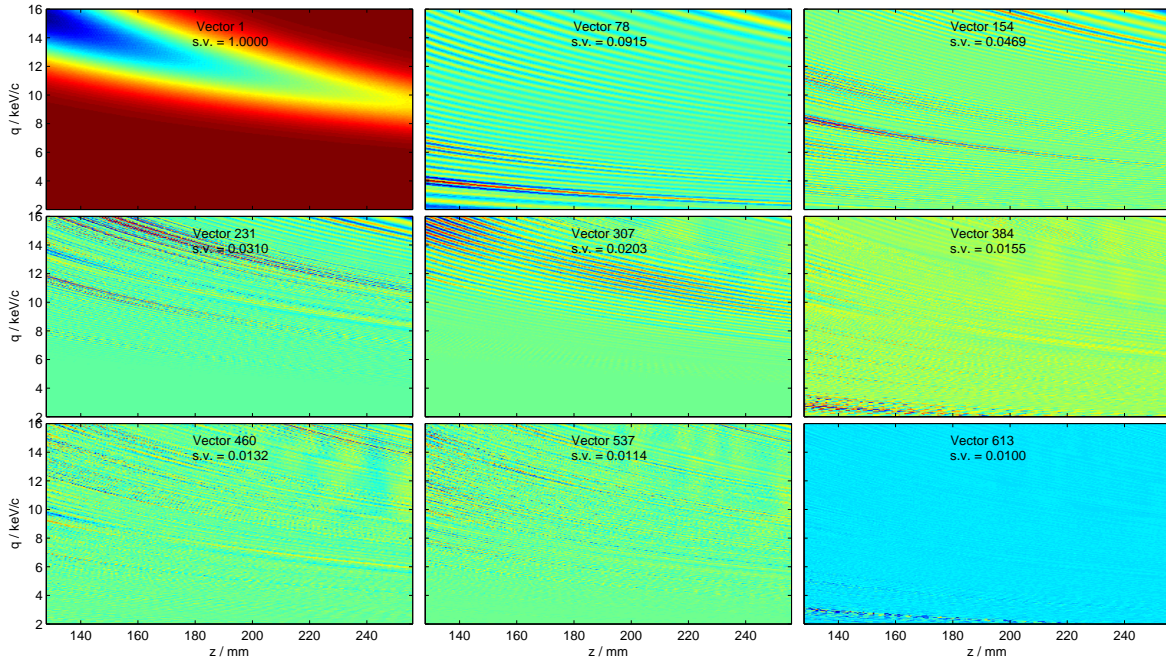


Figure 6.9: Singular vectors for $\Delta E = 8$ keV without a coded aperture.

When the periodic coded aperture is introduced to the system with $n = 16$ energy bins, the singular vectors are those shown in Figure 6.10. These vectors have strong dependence on both z and q , and importantly the number of singular values above the cutoff increased by a factor of 5.8 over the energy integrating detector with $n = 1$. Compared with the uncoded (“open”) system in the energy sensitive case $n = 16$, the coded aperture system enjoys a surprising four-fold increase in the number of measurable modes at the specified cutoff level of 0.01. Based on Figure 6.6, the open system needs $n = 64$ energy bins to achieve this number of measurable modes. These results suggest that combining the energy resolution of the detector and the resolving power of the coded aperture will be critical to high fidelity reconstruction of arbitrary scattering densities $F(z, q)$.

It is interesting to notice that while the structure of the singular vectors cannot be directly manipulated by choosing the aperture code (since the forward model depends on all system parameters), the singular vectors shown in Figures 6.8 and 6.10 for the periodic aperture bear a strong presence of periodic structure. For comparison, the singular vectors are shown

in Figure 6.11 for $n = 16$ energy bins used with a random binary aperture, where instead of arranged in a periodic structure, the lead features of the aperture were positioned randomly on the same grid. These vectors appear more random and may be better suited for objects not emphasizing periodic structure.

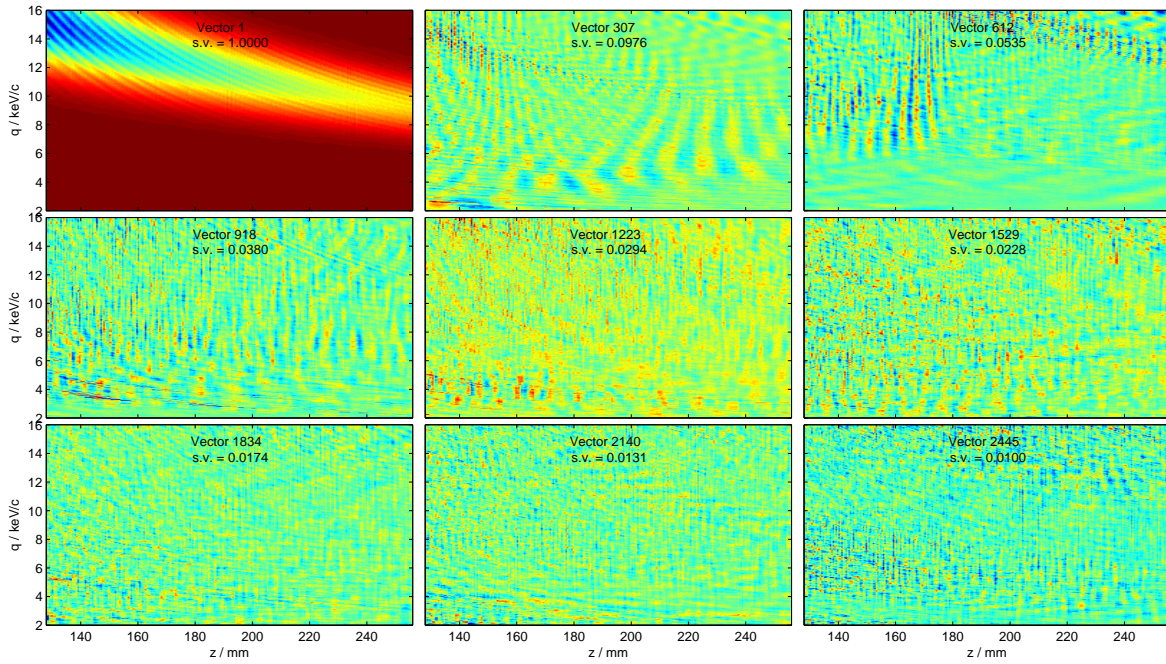


Figure 6.10: Singular vectors for $\Delta E = 8$ keV with a periodic coded aperture.

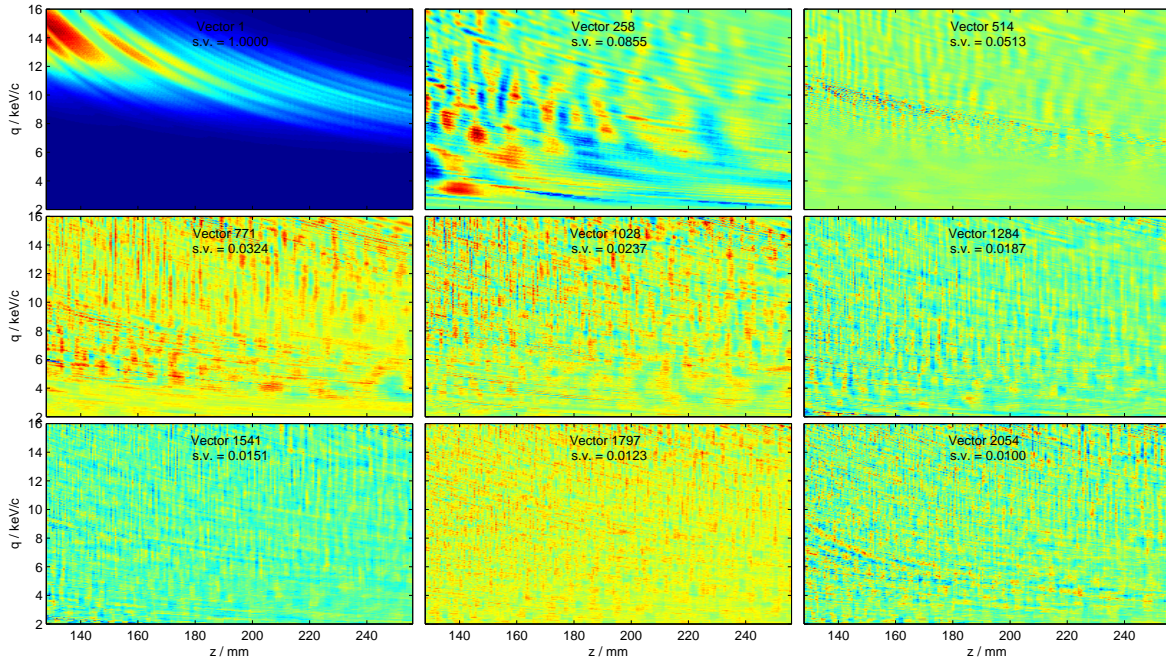


Figure 6.11: Singular vectors for $\Delta E = 8$ keV with a random binary coded aperture.

6.5 Reconstructions

To test the wisdom of the previous sections, measurements were simulated for the various energy sensitive detection schemes and MLE reconstructions were performed. Figure 6.12 shows the simulated object $F(z, q)$, which is based on a photograph from the Apache Trail in AZ, US. This is a non-physical object, since the coordinates are range z and momentum transfer q . Nevertheless, this example is meant to show the ability of the pencil beam system to reconstruct any arbitrary scattering density $F(z, q)$. Since the forward model (6.1) ignores proportionality constants, the intensity scale in Figure 6.12 is somewhat arbitrary. The forward matrix \mathbf{H} for each trial was computed and used to simulate measurements via $\mathbf{g} = \mathbf{H}\mathbf{f}$. These data were input to the Poisson MLE algorithm described by equation (1.9) in Chapter 1. To study the performance of the system in the low-noise (high flux) limit, noise was not introduced to \mathbf{g} prior to reconstruction. The iterations were terminated when the relative change in the log-likelihood (equation (1.7) in Chapter 1) dropped below 1%.

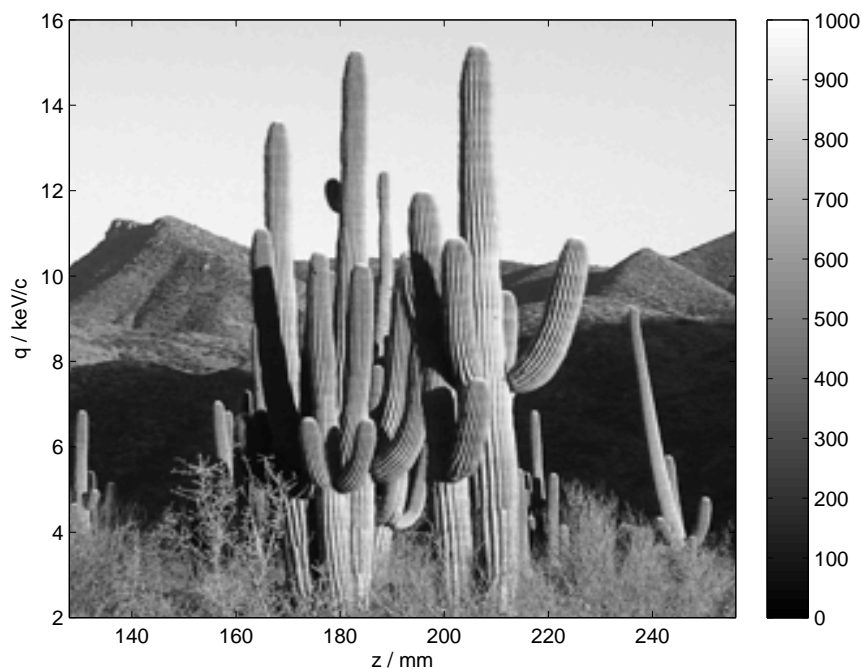


Figure 6.12: The 2D object used to simulate data for the reconstructions, where the grayscale value represents the value of the scattering density $F(z, q)$.

The performance of four coded apertures were compared for varying energy resolution: (1) the periodic code with 256 elements as previously described, (2) a binary random code where each of the 256 elements had a 50% probability of containing lead, (3) a grayscale random code where each of the elements had a concentration of lead randomly chosen between 0 and 1, and (4) no coded aperture. For illustration, the noiseless measurements for the random grayscale aperture are shown in Figure 6.13, where the color scale indicates the mean number of photons in each measurement. As expected from the incident spectrum (Figure 6.3), the measurements show peaks from the characteristic lines at 59, 67, and 69 keV, and the Bremsstrahlung background at a range of energies. The broad distribution of the measurements over space (x) and energy (E) shows that they are a hybrid of energy and angle dispersive. Looking at the measurements in Figure 6.13, it may be surprising that the original image is encoded therein.

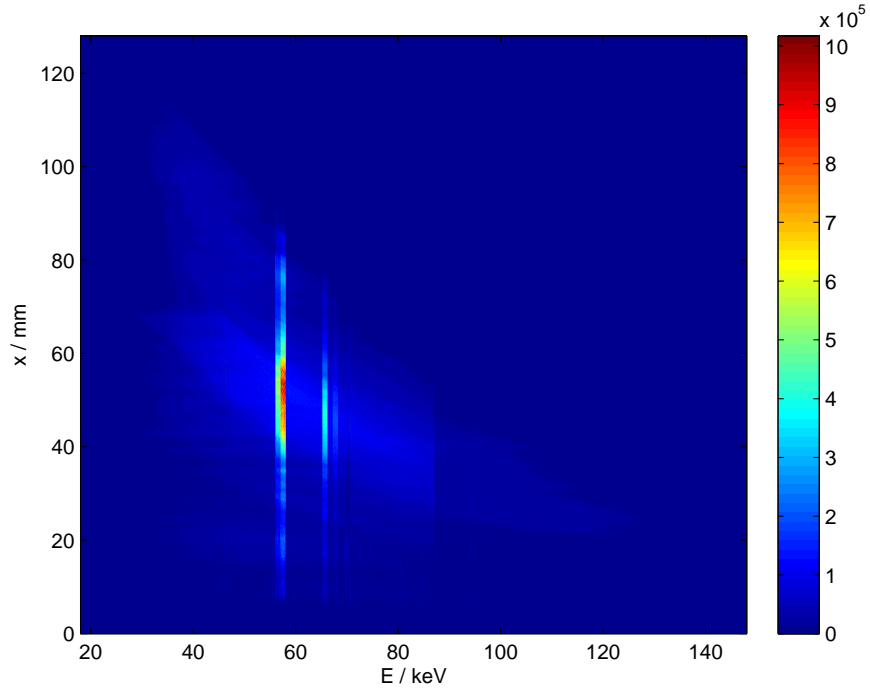


Figure 6.13: Simulated noiseless measurements \mathbf{g} for the case of $n = 1024$ bins ($\Delta E = 0.125$ keV) with a periodic coded aperture. The color scale indicates the number of photons in each measurement.

Reconstructions for the different apertures and selected energy resolutions are shown in Figure 6.14. The energy resolution in each case is found from $\Delta E = 128 \text{ keV}/n$, where n is the number of energy bins. The reconstructed image is not recognizable for any aperture using the energy integrating detector ($n = 1$ energy bin), but consistent with the SVD discussion of the previous section the cases with coded apertures shows more resemblance to the original object. With $n = 64$ energy bins the image starts to appear, except in the case with no coded aperture. The reconstructions improve with increasing energy resolution, as expected. These results show the benefit of using any of these apertures with energy sensitive measurements.

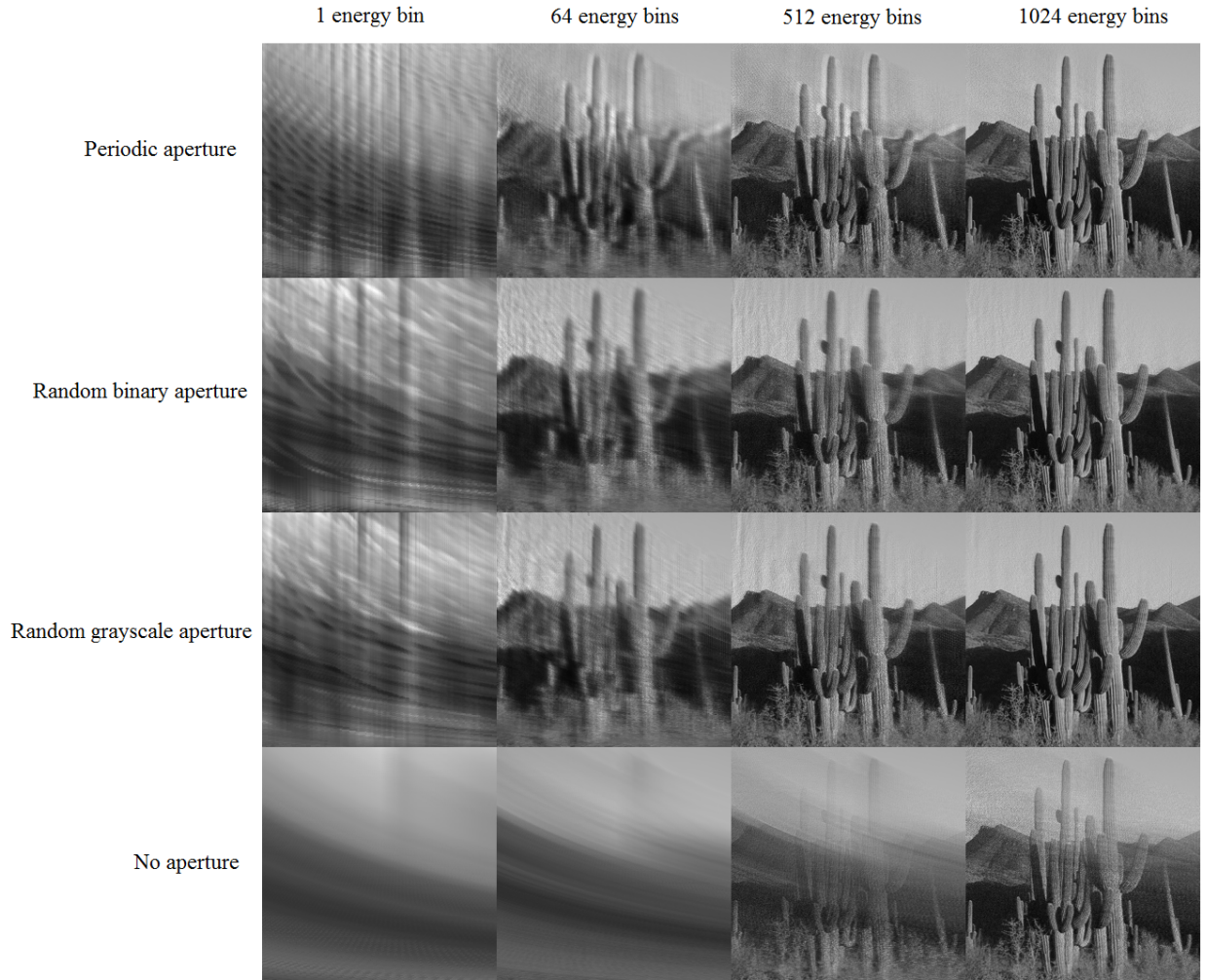


Figure 6.14: Reconstructed \mathbf{f} from the simulated measurements with varying energy resolution and coded apertures. Compare to the original object in Figure 6.12.

To compare the different reconstructions quantitatively, the root mean squared error (RMSE) was computed for each image and is plotted as a function of energy resolution in Figure 6.15. Each aperture is given a curve with a different color. The RMSE values were divided by the mean value of the original object (Figure 6.12) to give meaning to the vertical scale.

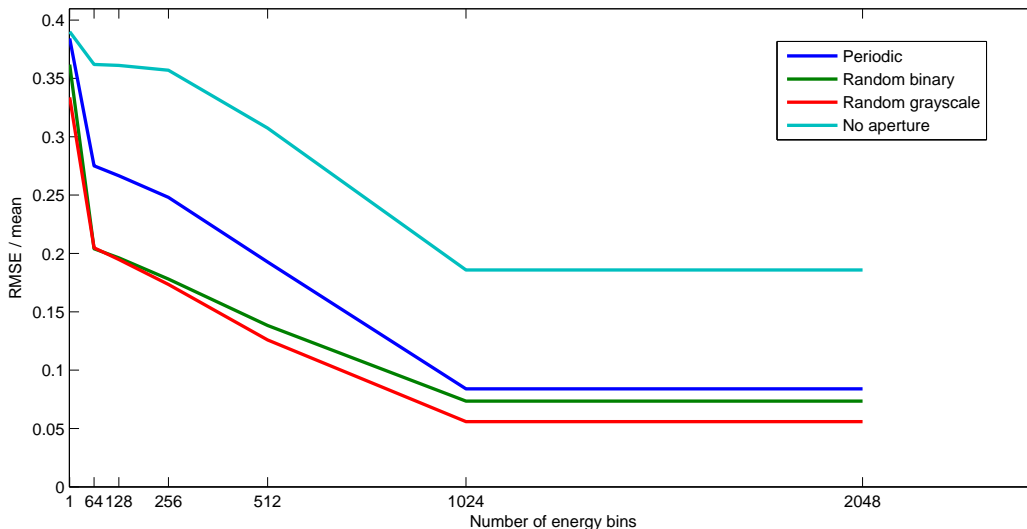


Figure 6.15: RMSE values for each reconstruction, plotted as a function of the number of energy bins and the choice of coded aperture. These RMSE values were divided by the mean value of the original object.

The reconstruction error decreases with an increase in the number of energy bins, as expected. The grayscale random code performed the best (it had the lowest RMSE), followed closely by the random binary code. The periodic code, while optimized for range resolution under isotropic scattering, could not quite compete with the random codes in this anisotropic model. Consistent with the PSF and SVD analysis above, the case with no aperture performs the worst. All the RMSE curves flattened out after 1024 energy bins, likely due to the limited precision of the model used for the incident spectrum.

Unlike the SVD analysis, the RMSE is an object-dependent metric. Further study would examine the reconstruction error for a broader class of objects, and compare 2D energy sensitive arrays with the analysis in Chapter 2. Energy sensitivity provides additional dimensionality to the measurements which will be critical for scaling CAXSI to 4D reconstruction of $F(x, y, z, q)$.

CHAPTER 7: SUMMARY AND OUTLOOK

The primary contributions of this work are new methods for tomography by reuniting coded apertures with x-rays through scatter imaging. These techniques are collectively named “coded aperture x-ray scatter imaging” (CAXSI). Enabling technologies for CAXSI are coded apertures designed for each specific imaging modality, and computational imaging techniques for recovering the desired images.

Non-destructive testing via x-ray tomography is critical to medicine, security, and quality inspection. X-ray attenuation imaging enjoys a long history of success in these and related fields. Scatter imaging, while less mature than attenuation imaging, has already enjoyed several decades of success. Scatter imaging seeks to measure the three dominant x-ray interactions with matter (photoelectric absorption, incoherent scattering, and coherent scattering) separately to provide improvements to tomography in the form of reduced dose, new modalities, and chemical specificity. Coded aperture imaging is another mature field with roots in x-ray astronomy, which has since been used with great success in spectroscopy and spectral imaging.

Chapter 1 included background on the history of coded apertures and x-ray scatter imaging, and a description of the advantages of CAXSI compared with alternative techniques. The physical principles of scattering were discussed, beginning with scattering from a point-like target and examining the structure of the resulting incoherent and coherent scatter signals. Emphasis was placed on coherent scattering since this is the primary mechanism for chemical identification, and simplifications and assumptions to the physical models were presented which were used in the following chapters. The extension of the point-like scattering experiment to volumetric imaging was discussed, with the measurement

process viewed as a linear transformation from the unknown distribution of the target object to the measurement domain. The dimensionality of the measurements compared with that of the reconstructed object was discussed for the various imaging modalities that followed, plus those in the literature. The concept of discretization of the continuous forward model was presented, establishing a common mathematical framework for the theory and experimental results. A noise model based on Poisson statistics was introduced which is applicable to photon-limited measurements and a corresponding reconstruction algorithm was derived based on Maximum Likelihood Estimation (MLE), which formed the basis of the reconstruction algorithms used throughout this work. Chapter 1 concluded with a description of the singular value decomposition (SVD) and motivated its utility in analyzing measurement structure and comparing different coded aperture designs.

Chapter 2 took a broad look at CAXSI systems from a theoretical standpoint and proposed a number of new coded aperture designs. The pencil beam system employing a periodic coded aperture was analyzed in detail, including its analytical SVD and resolution metrics under isotropic scattering conditions. Study of the anisotropic case led to new ideas about rotational orthogonality of codes, and motivated a number of novel coded apertures which were compared through numerical evaluation of their singular values. Fan beam scatter tomography was also analyzed for isotropic scattering, motivating yet another coded aperture design. The scalability of pencil beam and fan beam CAXSI were compared with Radon imaging and SVT, and found to be more favorable in terms of the magnitude of the singular values. This suggests that CAXSI system may achieve superior SNR and/or reduced patient dose when used in medical applications.

The first experimental demonstration of CAXSI was presented in Chapter 3. The experimental system included pencil beam illumination and enabled reconstruction of the scattering density as a function of range and momentum transfer. This was the first use of a periodic coded aperture to provide the range resolution necessary for such an endeavor. The momentum transfer spectra from two different crystalline samples at different locations

were reconstructed simultaneously from a single exposure (a “snapshot”) of a 2D detector array with no *a priori* position information. These results demonstrated the potential for tomography along 1D sections of a target and simultaneously measuring diffraction properties at each location. The pencil beam approach could be raster-scanned to acquire tomographic reconstructions through a volume or scanned over select regions of an object to obtain information about its material composition at each point of interest.

The success of the pencil beam CAXSI experiment motivated its extension to a fan beam system in Chapter 4. Transverse structure was introduced to the periodic coded aperture according to a modified uniformly redundant array (MURA). This coded aperture was the first of its kind for imaging 2D object sections oriented perpendicular to a detector plane. The imaging resolution resulting from such an aperture was presented, and an experimental setup was constructed which enabled reconstruction of a 2D slice of an object from a snapshot measurement. By acquiring a sequence of images, a dynamic object was reconstructed as the first demonstration of video-rate tomography. This technique can be used for measurement of a static 3D object if the fan beam is scanned in the direction of its normal. In addition to reconstructing density images, the reconstruction algorithm also recovered the angular scattering distribution for each object, which depends on, and may provide insight into, its material composition.

Moving beyond 1D and 2D systems, Chapter 5 proposed coded apertures and Fourier-based direct reconstruction algorithms for 3D imaging under isotropic scattering or emission. This approach was motivated in part by literature on incoherent holography using a Fresnel zone plate. A distinction was drawn between holography, which reconstructs the optical field, and tomography, which reconstructs the radiating object. Multiple exposures are required for tomography, and reconstruction techniques were presented for time series measurements from a 2D detector array. Aside from changing the code itself over the time series, which is difficult in practice, the distance between the aperture and detector may be varied, or the object may be linearly translated to achieve complete sampling of the object. Coded apertures enabling

such reconstructions were presented which belong to a new family termed “frequency scale codes” (FSC). The 1D sinusoid coded aperture proposed in Chapter 2 and used in the experimental setup of Chapter 3 is understood to be the simplest FSC. Reconstruction using a FSC enables sampling of individual Fourier coefficients, motivating a discussion of potential applications to compressive tomography and adaptive sensing.

Chapter 6 introduced the concept of energy sensitive detection for coherent scatter imaging. These detectors provide a wealth of information about coherent scatter events due to the energy dependence of Bragg’s law. This chapter considered linear arrays of energy sensitive detectors for coherent scatter imaging with a pencil beam. The degree of energy resolution was studied as it affects the imaging resolution in range and momentum transfer. Point spread functions were analyzed in terms of their dependence on the incident spectrum, coded aperture, and energy resolution of the detector. SVD analysis provided insight into the benefits of improved energy resolution and incorporation of a coded aperture. Reconstructions were performed from simulated measurements which verify the effects of improved energy resolution and the benefits of using a coded aperture.

The results presented here provide direction for future work in tomographic scatter imaging. Detailed resolution and signal to noise analyses will be necessary for specific applications of the various CAXSI modalities. The forward models presented here capture the basic physics of each system, however more sophisticated models will include corrections for attenuation and multiple scattering effects as well. Multiplexed coherent scatter tomography of 3D objects will require further study, with energy sensitive detection being a key enabling technology. The coded aperture techniques presented in this work may also be useful for ray-based optical systems operating at wavelengths far removed from x-rays.

APPENDIX A: ENERGY TRANSFORMATION OF THE COHERENT SCATTER DIFFERENTIAL CROSS SECTION

The coherent scatter forward models introduced in Section 1.2.1 of Chapter 1 and used in Chapters 3 and 6 ignore the energy dependent coherent scatter cross section $\sigma_C(E)$. This can be partially justified by using a narrowband spectrum, or in the first order scattering approximation by multiplying $N(E)$ by the probability for coherent scattering. In the following, a more accurate model is presented which retains the normalization factor $A(E)$ and the Thompson factor $1 + \cos^2\theta$ in the expression for the differential scattering cross section $\frac{d\sigma_C}{d\Omega}$ (equation (1.4) in Chapter 1). This section uses the notation defined there, except that in the following, the ‘‘C’’ subscripts are dropped so that σ and $\frac{d\sigma}{d\Omega}$ refer to coherent scatter cross sections.

Assume the x-ray diffraction measurement $g(\theta)$ was acquired by an energy-dispersive diffractometer such as the X’Pert PRO (PANalytical B.V., Almelo, The Netherlands). The beam is approximated as monochromatic at energy \bar{E} and the sample is assumed to be point-like. An irradiance detector scans the scatter angle θ to acquire the irradiance measurements $g(\theta)$. Given this function and a model for $\sigma(E)$ for this sample from standard tables [38], we would like to calculate the differential cross section $\frac{d\sigma}{d\Omega}(E, \theta)$ at arbitrary energy E and angle θ and use it in more accurate forward models. As a consequence of the normalization, a linear forward model in $\frac{d\sigma}{d\Omega}(E, \theta)$ will become nonlinear in the scattering density $F(q)$,

The measured irradiance $g(\theta)$ is proportional to $\frac{d\sigma}{d\Omega}(\bar{E}, \theta)$, the differential cross section at energy \bar{E} and angle θ . The normalization enforces that the known total cross section $\sigma(E) = \int d\Omega \frac{d\sigma}{d\Omega}(E, \theta)$, where $d\Omega = \sin\theta d\theta d\phi$ is a solid angle element at angle θ and ϕ is the azimuthal angle, of which the scattering is assumed independent. For simplicity, assume the measurements are normalized so that $\int d\Omega g(\bar{E}, \theta) = 1$. The differential cross section $\frac{d\sigma}{d\Omega}(\bar{E}, \theta)$ at fixed \bar{E} is simply

$$\frac{d\sigma}{d\Omega}(\bar{E}, \theta) = \sigma(\bar{E}) g(\theta) \tag{7.1}$$

Rewriting the left side of this expression in terms of the coherent scattering density $F(q)$ (equation 1.4 in Chapter 1), and solving for this function, we find the scattering density

$$F(q) = \frac{g(\theta = 2 \sin^{-1} [\frac{qc}{2E}])}{[1 + \cos^2(2 \sin^{-1} [\frac{qc}{2E}])]} \quad (7.2)$$

where q is only specified up to a value of $\frac{2\bar{E}}{c} \sin \frac{\bar{\theta}_{max}}{2}$, and $\bar{\theta}_{max}$ is the maximum scatter angle measured. The expression (7.2) ignores the factor $\sigma(\bar{E})/A(\bar{E})$ since we only need to specify $F(q)$ to within a multiplicative constant to compute $\frac{d\sigma}{d\Omega}(E, \theta)$. Repeating equation (1.4) in Chapter 1:

$$\frac{d\sigma}{d\Omega}(E, \theta) = A(E) (1 + \cos^2 \theta) F\left(q = \frac{2E}{c} \sin \frac{\theta}{2}\right) \quad (7.3)$$

and enforcing the normalization $\sigma(E) = \int d\Omega \frac{d\sigma}{d\Omega}(E, \theta)$, we find the normalization factor

$$A(E) = \frac{\sigma(E)}{\int d\Omega (1 + \cos^2 \theta) F\left(q = \frac{2E}{c} \sin \frac{\theta}{2}\right)} \quad (7.4)$$

The result is the differential cross section

$$\frac{d\sigma}{d\Omega}(E, \theta) = \frac{\sigma(E) (1 + \cos^2 \theta) F\left(q = \frac{2E}{c} \sin \frac{\theta}{2}\right)}{\int d\Omega' (1 + \cos^2 \theta') F\left(q = \frac{2E}{c} \sin \frac{\theta'}{2}\right)} \quad (7.5)$$

where Ω' and associated θ' are integration variables, and $F(q)$ is computed from (7.2). Note that the differential cross section (7.5) is now nonlinear in the scattering density $F(q)$, producing a more complex but accurate scattering model. However, the linear scattering models of Chapters 3 and 6 are justified when the denominator in (7.5) does not vary significantly over the measured energy range.

APPENDIX B: SINGULAR VALUE DECOMPOSITION FOR FAN BEAM CAXSI

In this section we derive the singular value decomposition for fan beam CAXSI under isotropic scattering, as described in Chapter 2. Starting with the forward model in equation (2.7) from Chapter 2, we introduce the projective coordinates:

$$\begin{aligned}\alpha &= y' \frac{d}{z'} \\ \beta &= 1 - \frac{d}{z'}\end{aligned}$$

If we define a new object function $F(\alpha, \beta) = \frac{d}{(1-\beta)^3} F\left(x' = 0, \frac{\alpha}{1-\beta}, \frac{d}{1-\beta}\right)$, the forward model becomes

$$G(x, y) = \int_0^1 \int_{-\infty}^{\infty} F(\alpha, \beta) T[x\beta, \beta y + \alpha] \, d\alpha \, d\beta.$$

The adjoint is defined by

$$F_A(\alpha', \beta') = \int_{-Y/2}^{Y/2} \int_{-X/2}^{X/2} G(x, y) T[x\beta', \beta' y + \alpha']^* \, dx \, dy.$$

We rearrange this expression in terms of the normal operator:

$$F_A(\alpha', \beta') = \int_0^1 \int_{-\infty}^{\infty} F(\alpha, \beta) K(\alpha, \beta, \alpha', \beta') \, d\alpha \, d\beta$$

with kernel function

$$\begin{aligned}K(\alpha, \beta, \alpha', \beta') &= \int_{-X/2}^{X/2} \int_{-Y/2}^{Y/2} T[x\beta, \beta y + \alpha] \\ &\quad \times T[x\beta', \beta' y + \alpha']^* \, dx \, dy\end{aligned}\tag{7.6}$$

Now consider a separable aperture code with the form $T(x, y) = [1 + A(x)B(y)]/2$ and $-1 \leq A(x)B(y) \leq 1$. Inserting this into equation (7.6):

$$K_S(\alpha, \beta, \alpha', \beta') = \int_{-X/2}^{X/2} \int_{-Y/2}^{Y/2} \frac{1 + A(x\beta)B[\beta y + \alpha]}{2} \times \frac{1 + A(x\beta')^*B[\beta' y + \alpha']^*}{2} dy dx.$$

We consider codes with 50% average transmission so that $\int_{-X/2}^{X/2} \int_{-Y/2}^{Y/2} A(x\beta)B[\beta y + \alpha] dy dx \approx 0$. Then we can neglect this contribution and consider only

$$K_S(\alpha, \beta, \alpha', \beta') = \frac{XY}{4} + \frac{1}{4} \int_{-X/2}^{X/2} A(x\beta)A(x\beta')^* dx \times \int_{-Y/2}^{Y/2} B[\beta y + \alpha]B[\beta' y + \alpha']^* dy \quad (7.7)$$

With our scale code $A(x) = \cos(2\pi ux)$, the integral over X is

$$\begin{aligned} & \int_{-X/2}^{X/2} \cos(2\pi ux\beta) \cos(2\pi ux\beta') dx \\ &= \frac{1}{2} \int_{-X/2}^{X/2} \cos[2\pi ux(\beta - \beta')] + \cos[2\pi ux(\beta + \beta')] dx \\ &= \frac{1}{2\pi u(\beta - \beta')} \sin[\pi uX(\beta - \beta')] + \frac{1}{2\pi u(\beta + \beta')} \sin[\pi uX(\beta + \beta')] \\ &\approx \frac{X}{2} \text{sinc}[N_x(\beta - \beta')], \end{aligned}$$

with $N_x = uX$. This neglects the rapidly oscillating term $\beta + \beta'$. The eigenfunctions for the sinc kernel are the prolate spheroidal wavefunctions [82], however we take a different approach here. For simplicity we take $N_x \gg 1$ so that the integral is only nonzero when

$\beta \approx \beta'$. Equation (7.7) is approximated by

$$\begin{aligned}
K_S(\alpha, \beta, \alpha', \beta') &= \frac{XY}{4} + \frac{X}{8} \text{sinc}[N_x(\beta - \beta')] \\
&\times \int_{-Y/2}^{Y/2} B\left[\frac{\beta + \beta'}{2}y + \alpha\right] B\left[\frac{\beta + \beta'}{2}y + \alpha'\right]^* dy
\end{aligned} \tag{7.8}$$

with $\frac{\beta + \beta'}{2} \approx \beta \approx \beta'$ at the peak of the sinc function. If $B(y)$ is periodic with period P so that $B(y) = \sum_{n=-\infty}^{\infty} c_n \exp\left(\frac{2\pi i n y}{P}\right)$ (as would be represented by a convolutional code), then

$$\begin{aligned}
K_S(\alpha, \beta, \alpha', \beta') &= \frac{XY}{4} + \frac{X}{8} \text{sinc}[N_x(\beta - \beta')] \\
&\times \int_{-Y/2}^{Y/2} \left[\sum_n c_n \exp\left(\frac{2\pi i n}{P} \left[\frac{\beta + \beta'}{2}y + \alpha\right]\right) \right] \\
&\times \left[\sum_{n'} c_{n'}^* \exp\left(\frac{-2\pi i n'}{P} \left[\frac{\beta + \beta'}{2}y + \alpha'\right]\right) \right] dy.
\end{aligned}$$

We approximate the integral with a full period over the periodic function, which is $\frac{2P}{\beta + \beta'}$, neglecting any edge effects:

$$\begin{aligned}
K_S(\alpha, \beta, \alpha', \beta') &= \frac{XY}{4} + \frac{X}{8} \text{sinc}[N_x(\beta - \beta')] \frac{Y(\beta + \beta')}{2P} \\
&\times \int_{-P/(\beta + \beta')}^{P/(\beta + \beta')} \left[\sum_n c_n \exp\left(\frac{2\pi i n}{P} \left[\frac{\beta + \beta'}{2}y + \alpha\right]\right) \right] \\
&\times \left[\sum_{n'} c_{n'}^* \exp\left(\frac{-2\pi i n'}{P} \left[\frac{\beta + \beta'}{2}y + \alpha'\right]\right) \right] dy.
\end{aligned}$$

All of the terms for which $n \neq n'$ are zero, so the integral becomes

$$K_S(\alpha, \beta, \alpha', \beta') = \frac{XY}{4} + \frac{X}{8} \text{sinc}[N_x(\beta - \beta')] \frac{Y(\beta + \beta')}{2P}$$

$$\times \int_{-P/(\beta+\beta')}^{P/(\beta+\beta')} \sum_n |c_n|^2 \exp\left(\frac{2\pi i n}{P} [\alpha - \alpha']\right) dy.$$

Evaluating the integral,

$$\begin{aligned} K_S(\alpha, \beta, \alpha', \beta') &= \frac{XY}{4} + \frac{XY}{8} \text{sinc}[N_x(\beta - \beta')] \\ &\times \sum_{n=-\infty}^{\infty} |c_n|^2 \exp\left(\frac{2\pi i n}{P} [\alpha - \alpha']\right). \end{aligned}$$

The sum is just the Fourier series of the auto-correlation of $B(y)$, represented by $B_A(y)$:

$$K_S(\alpha, \beta, \alpha', \beta') = \frac{XY}{4} \left(1 + \frac{1}{2} \text{sinc}[N_x(\beta - \beta')] B_A(\alpha - \alpha') \right) \quad (7.9)$$

Equation (7.9) describes the point spread function (PSF) at projective coordinates (α, β) due to an impulse at (α', β') . The singular value decomposition can be found by solving the eigenvalue equation

$$\lambda_{mn}^2 F(\alpha', \beta') = \int_0^1 \int_{-\infty}^{\infty} F_{mn}(\alpha, \beta) K(\alpha, \beta, \alpha', \beta') d\alpha d\beta, \quad (7.10)$$

with the eigenvectors being the singular vectors of the kernel and the eigenvalues being the squares of the singular values λ_{mn} . For simplicity, we assume the object is periodic such that $F(\alpha, \beta) = F(\alpha + P, \beta + 1)$. An ansatz for the form of the singular vectors is

$$F_{mn}(\alpha, \beta) = e^{-2\pi i \left(\frac{\alpha m}{P} + \beta n \right)}$$

Inserting this into the eigenvalue equation (7.10),

$$\lambda_{mn}^2 e^{-2\pi i \left(\frac{\alpha' m}{P} + \beta' n \right)} = \frac{1}{P} \int_{-P/2}^{P/2} d\alpha \int_0^1 d\beta e^{-2\pi i \left(\frac{\alpha m}{P} + \beta n \right)} K(\alpha, \beta, \alpha', \beta').$$

On the right hand side, the integrals over the first term in $K(\alpha, \beta, \alpha', \beta')$ evaluate to

$$\frac{XY}{4P} \int_{-P/2}^{P/2} d\alpha e^{-\frac{2\pi i \alpha m}{P}} \int_0^1 d\beta e^{-2\pi i \beta n} = \frac{XY}{4} \delta_{n0} \delta_{m0}$$

The second term in K produces

$$\frac{XY}{8P} \int_{-P/2}^{P/2} d\alpha e^{-\frac{2\pi i \alpha m}{P}} B_A(\alpha - \alpha') \int_0^1 d\beta e^{-2\pi i \beta n} \text{sinc}[N_x(\beta - \beta')].$$

The first integral evaluates to $(XY/8) \exp(-2\pi i m \alpha'/P) |c_m|^2$. For the second integral, since $N_x \gg 1$ the sinc function only contributes when $\beta \approx \beta'$ and we can extend the limits to $\pm\infty$. The result is the Fourier transform of the sinc, or $\exp(-2\pi \beta' n) \text{rect}(n/N_x)/N_x$. We find singular values

$$\lambda_{mn} = \frac{\sqrt{XY}}{2} \sqrt{\delta_{m0} \delta_{n0} + \frac{|c_m|^2}{2N_x} \text{rect}\left(\frac{n}{N_x}\right)}. \quad (7.11)$$

To evaluate c_m , note that the function $B(y)$ is the convolution of the code sequence $a(y) = \sum_{n=0}^{N_y-1} a_n \delta(y - nP/N_y)$ and the pulse train $b(y) = \sum_{m=-\infty}^{\infty} \text{rect}[N_y(y/P - m)]$, where N_y is the code length. From the convolution theorem, the continuous Fourier transform of $B(y)$ is $\tilde{B}(\nu') = \tilde{a}(\nu') \tilde{b}(\nu')$, where ν' is a spatial frequency and

$$\begin{aligned} \tilde{a}(\nu') &= \int_{-\infty}^{\infty} dy e^{-2\pi i y \nu'} a(y) \\ &= \sum_{n=0}^{N_y-1} a_n e^{-2\pi i n \nu' P/N_y} \\ \tilde{b}(\nu') &= \int_{-\infty}^{\infty} dy e^{-2\pi i y \nu'} b(y) \\ &= \frac{1}{N_y} \text{sinc}\left(\frac{\nu' P}{N_y}\right) \sum_{m=-\infty}^{\infty} \delta\left(\nu' - \frac{m}{P}\right) \end{aligned}$$

The coefficients c_m can be extracted via

$$c_m = \lim_{\epsilon \rightarrow 0} \int_{m/P-\epsilon}^{m/P+\epsilon} d\nu' \tilde{B}(\nu')$$

$$\begin{aligned}
&= \frac{1}{N_y} \operatorname{sinc} \left(\frac{m}{N_y} \right) \sum_{n=0}^{N_y-1} a_n e^{-2\pi i n m / N_y} \\
&= \frac{1}{N_y} \operatorname{sinc} \left(\frac{m}{N_y} \right) \tilde{a}_m,
\end{aligned}$$

where $\{\tilde{a}_m\}$ is the discrete Fourier transform (DFT) of $\{a_n\}$. From Parseval's theorem, the root-mean-squared (RMS) value of \tilde{a}_m is

$$\begin{aligned}
\sqrt{\frac{1}{N_y} \sum_{m=0}^{N_y-1} |\tilde{a}_m|^2} &= \sqrt{\sum_{m=0}^{N_y-1} |a_n|^2} \\
&= \sqrt{N_y}
\end{aligned}$$

where the last line follows from $a_n = \pm 1$. Therefore we have $|c_m| \approx \operatorname{sinc}(m/N_y) / \sqrt{N_y}$. Substituting this value for c_m in equation (7.11), the singular values for $m \neq 0$ or $n \neq 0$ are

$$\lambda_{mn} = \frac{1}{2} \sqrt{\frac{XY}{N_x N_y}} \operatorname{rect} \left(\frac{n}{N_x} \right) \operatorname{sinc} \left(\frac{m}{N_y} \right)$$

This spectrum has maximum value $\lambda_{00} = \sqrt{XY}/2$ and roughly $N_x N_y$ singular values that are smaller by a factor of $\sqrt{N_x N_y}$. When estimating N^2 object coefficients with $N_x = N_y = N$, the singular values have magnitude proportional to $1/N$.

APPENDIX C: DETERMINATION OF SOURCE POSITION

In this section we present the technique used to locate the x-ray anode for the experiment in Chapter 4. We placed point phantoms at positions \mathbf{p}^a , where the index a labels the particular phantom. The phantom points used were the corners of the coded aperture when placed at varying ranges from the detector plane. X-ray projections of these points were made to give the image positions \mathbf{q}^a on the detector. We would like to find the position \mathbf{s} of the x-ray anode (hereafter, the “source”) from these projections.

Each point phantom and its image together produce a line. The source ideally lies at the intersection of these lines, but due to measurement errors the lines may not all cross. A simple choice is to minimize the sum of the squared distances from \mathbf{s} to each line. The line defined by point \mathbf{p} and \mathbf{q} is parameterized by

$$\mathbf{r}(\lambda) = \mathbf{q} + \lambda(\mathbf{p} - \mathbf{q}) \quad (7.12)$$

The squared distance between \mathbf{s} and each point on this line is

$$\begin{aligned} L^2(\lambda) &= |\mathbf{s} - \mathbf{r}(\lambda)|^2 \\ &= \sum_i (s_i - r_i(\lambda))^2 \\ &= \sum_i [s_i - q_i - \lambda(p_i - q_i)]^2 \\ &= \sum_i [(s_i - q_i)^2 + \lambda^2 (p_i - q_i)^2 - 2\lambda (s_i - q_i)(p_i - q_i)] \end{aligned}$$

Where the sum runs over all spatial dimensions. The minimum distance occurs when

$$\begin{aligned} \frac{dL^2(\lambda)}{d\lambda} &= 0 \\ &= 2 \sum_i (\lambda (p_i - q_i) - (s_i - q_i)(p_i - q_i)) \end{aligned}$$

and therefore when

$$\lambda = \frac{(\mathbf{s} - \mathbf{q}) \cdot (\mathbf{p} - \mathbf{q})}{|\mathbf{p} - \mathbf{q}|^2}$$

Inserting this into (7.12) gives the minimum distance

$$\begin{aligned} L^2 &= \sum_i \left[(s_i - q_i)^2 + \left(\frac{(\mathbf{s} - \mathbf{q}) \cdot (\mathbf{p} - \mathbf{q})}{|\mathbf{p} - \mathbf{q}|^2} \right)^2 (p_i - q_i)^2 - 2 \left(\frac{(\mathbf{s} - \mathbf{q}) \cdot (\mathbf{p} - \mathbf{q})}{|\mathbf{p} - \mathbf{q}|^2} \right) (s_i - q_i) (p_i - q_i) \right] \\ &= |\mathbf{s} - \mathbf{q}|^2 - \left(\frac{(\mathbf{s} - \mathbf{q}) \cdot (\mathbf{p} - \mathbf{q})}{|\mathbf{p} - \mathbf{q}|^2} \right)^2 \end{aligned}$$

To find \mathbf{s} , minimization can be performed on the sum of minimum distances to each line:

$$\begin{aligned} J &= \sum_a L_a^2 \\ &= \sum_a (|\mathbf{s} - \mathbf{q}^a|^2 - [(\mathbf{s} - \mathbf{q}^a) \cdot \mathbf{u}^a]^2) \end{aligned}$$

where $\mathbf{u}^a = \frac{\mathbf{p}^a - \mathbf{q}^a}{|\mathbf{p}^a - \mathbf{q}^a|}$. The derivatives of J with respect to the components s_i are

$$\frac{\partial J}{\partial s_i} = \sum_a [2(s_i - q_i^a) - 2u_i^a (\mathbf{s} - \mathbf{q}^a) \cdot \mathbf{u}^a]$$

Minimization occurs when

$$\begin{aligned} \frac{\partial J}{\partial s_i} &= 0 & (7.13) \\ &= \sum_a [2(s_i - q_i^a) - 2u_i^a (\mathbf{s} - \mathbf{q}^a) \cdot \mathbf{u}^a] \\ &= \sum_a (s_i - q_i^a) - \sum_a u_i^a \sum_j (s_j - q_j^a) u_j^a \\ &= \sum_a (s_i - q_i^a) - \sum_a u_i^a \sum_j u_j^a (s_j - q_j^a) \end{aligned}$$

which can be expressed as

$$\begin{aligned}
\sum_a \sum_j (\delta_{ij} - u_i^a u_j^a) (s_j - q_j^a) &= 0 \\
\sum_a \sum_j (\delta_{ij} - u_i^a u_j^a) s_j &= \sum_a \sum_j (\delta_{ij} - u_i^a u_j^a) q_j^a \\
\sum_j \sum_a (\delta_{ij} - u_i^a u_j^a) s_j &= \sum_a \left(q_i^a - u_i^a \sum_j u_j^a q_j^a \right) \\
\sum_a (\mathbf{1} - \mathbf{u}^a \otimes \mathbf{u}^a) \mathbf{s} &= \sum_a (\mathbf{1} - \mathbf{u}^a \otimes \mathbf{u}^a) \mathbf{q}^a \\
\left[\sum_a \mathbf{M}^a \right] \mathbf{s} &= \sum_a \mathbf{M}^a \mathbf{q}^a
\end{aligned} \tag{7.14}$$

where $\mathbf{M}^a = \mathbf{1} - \mathbf{u}^a \otimes \mathbf{u}^a$ is the operator projecting a vector onto the space orthogonal to \mathbf{u}^a . The solution for the source position \mathbf{s} is

$$\mathbf{s} = \left[\sum_a \mathbf{M}^a \right]^{-1} \sum_a \mathbf{M}^a \mathbf{q}^a$$

where the inverse can be solved by standard linear algebra techniques.

REFERENCES

- [1] A. C. Kak and M. Slaney, *Principles of Computerized Tomographic Imaging*. IEEE Press, 1988.
- [2] C. A. Carlsson, “Imaging modalities in x-ray computerized tomography and in selected volume tomography,” *Physics in medicine and biology*, vol. 44, no. 3, p. R23, 1999.
- [3] D. J. Brady, N. P. Pitsianis, and X. Sun, “Reference structure tomography,” *J. Opt. Soc. Am. A*, vol. 21, pp. 1140–1147, Jul 2004.
- [4] D. J. Brady, *Optical imaging and spectroscopy*. Wiley-OSA, 2009.
- [5] S. Orlov, “Theory of 3-dimensional reconstruction. 1. conditions for a full set of projections,” *Kristallografiya*, vol. 20, no. 3, pp. 511–515, 1975.
- [6] H. Tuy, “An inversion formula for cone-beam reconstruction,” *SIAM Journal on Applied Mathematics*, vol. 43, no. 3, pp. 546–552, 1983.
- [7] J. Zhang, G. Yang, Y. Cheng, B. Gao, Q. Qiu, Y. Z. Lee, J. P. Lu, and O. Zhou, “Stationary scanning x-ray source based on carbon nanotube field emitters,” *Applied Physics Letters*, vol. 86, no. 18, 2005.
- [8] F. T. Farmer and M. P. Collins, “A new approach to the determination of anatomical cross-sections of the body by compton scattering of gamma-rays,” *Physics in medicine and biology*, vol. 16, no. 4, p. 577, 1971.
- [9] F. T. Farmer and M. P. Collins, “A further appraisal of the compton scattering method for determining anatomical cross-sections of the body,” *Physics in medicine and biology*, vol. 19, no. 6, p. 808, 1974.
- [10] G. Harding, “X-ray scatter tomography for explosives detection,” *Radiation Physics and Chemistry*, vol. 71, no. 3, pp. 869–881, 2004.
- [11] J. Callerame, “X-ray backscatter imaging: Photography through barriers,” *Powder diffraction*, vol. 21, no. 02, pp. 132–135, 2006.
- [12] E. Van Uytven, S. Pistorius, and R. Gordon, “An iterative three-dimensional electron density imaging algorithm using uncollimated compton scattered x rays from a polyenergetic primary pencil beam,” *Medical physics*, vol. 34, p. 256, 2007.
- [13] G. Harding and E. Harding, “Compton scatter imaging: A tool for historical exploration,” *Applied Radiation and Isotopes*, vol. 68, no. 6, pp. 993–1005, 2010.
- [14] V. Grubsky, V. Romanov, N. Patton, and T. Jansson, “Compton imaging tomography technique for nde of large nonuniform structures,” in *SPIE Optical Engineering and Applications*, pp. 81440G–81440G, International Society for Optics and Photonics, 2011.

- [15] T. T. Truong and M. K. Nguyen, “Radon transforms on generalized cormack’s curves and a new compton scatter tomography modality,” *Inverse Problems*, vol. 27, no. 12, p. 125001, 2011.
- [16] C. Kittel, *Introduction to Solid State Physics*. Wiley, 7th ed., 1995.
- [17] B. Buras, J. S. Olsen, L. Gerward, G. Will, and E. Hinze, “X-ray energy-dispersive diffractometry using synchrotron radiation,” *Journal of Applied Crystallography*, vol. 10, no. 6, pp. 431–438, 1977.
- [18] B. D. Cullity, *Elements of X-ray diffraction*. Addison-Wesley, 1978.
- [19] P. G. Lale, “The examination of internal tissues, using gamma-ray scatter with a possible extension to megavoltage radiography,” *Physics in medicine and biology*, vol. 4, no. 2, p. 159, 1959.
- [20] P. Lale, “The examination of internal tissues by high-energy scattered x radiation,” *Radiology*, vol. 90, no. 3, pp. 510–517, 1968.
- [21] J. A. Stokes, K. R. Alvar, R. L. Corey, D. G. Costello, J. John, S. Kocimski, N. A. Lurie, D. D. Thayer, A. P. Trippe, and J. C. Young, “Some new applications of collimated photon scattering for nondestructive examination,” *Nuclear Instruments and Methods in Physics Research*, vol. 193, no. 1, pp. 261–267, 1982.
- [22] G. Harding and J. Kosanetzky, “Scattered x-ray beam nondestructive testing,” *Nuclear Instruments and Methods in Physics Research Section A: Accelerators, Spectrometers, Detectors and Associated Equipment*, vol. 280, no. 2, pp. 517–528, 1989.
- [23] R. W. Madden, J. Mahdavi, R. C. Smith, and R. Subramanian, “An explosives detection system for airline security using coherent x-ray scattering technology,” in *Optical Engineering+ Applications*, p. 707915, International Society for Optics and Photonics, 2008.
- [24] O. Lazzari, S. Jacques, T. Sochi, and P. Barnes, “Reconstructive colour x-ray diffraction imaging—a novel teddi imaging method,” *Analyst*, vol. 134, no. 9, pp. 1802–1807, 2009.
- [25] G. Harding, D. Kosciesza, S. Olesinski, and H. Strecker, “Experimental comparison of next-generation xdi topologies,” in *Proc. SPIE*, vol. 7806, pp. 78060I–1–78060I–9, 2010.
- [26] G. Harding and J. Kosanetzky, “Elastic scatter computed tomography,” *Physics in Medicine and Biology*, vol. 30, no. 2, p. 183, 1985.
- [27] D. L. Batchelar and I. A. Cunningham, “Material-specific analysis using coherent-scatter imaging,” *Medical physics*, vol. 29, p. 1651, 2002.
- [28] J. P. Schlomka, A. Harding, U. Van Stevendaal, M. Grass, and G. L. Harding, “Coherent scatter computed tomography: a novel medical imaging technique,” in *Medical Imaging*

- 2003, pp. 256–265, International Society for Optics and Photonics, 2003.
- [29] M. T. M. Davidson, D. L. Batchelar, S. Velupillai, J. D. Denstedt, and I. A. Cunningham, “Laboratory coherent-scatter analysis of intact urinary stones with crystalline composition: a tomographic approach,” *Physics in medicine and biology*, vol. 50, no. 16, p. 3907, 2005.
 - [30] J. Delfs and J. P. Schlomka, “Energy-dispersive coherent scatter computed tomography,” *Applied physics letters*, vol. 88, no. 24, p. 243506, 2006.
 - [31] K. P. MacCabe, K. Krishnamurthy, A. Chawla, D. L. Marks, E. Samei, and D. J. Brady, “Pencil beam coded aperture x-ray scatter imaging,” *Optics Express*, vol. 20, no. 15, pp. 16310–16320, 2012.
 - [32] K. P. MacCabe, A. D. Holmgren, M. P. Tornai, and D. J. Brady, “Snapshot 2d tomography via coded aperture x-ray scatter imaging,” *Applied Optics*, vol. 52, pp. 4582–4589, Jul 2013.
 - [33] D. J. Brady, D. L. Marks, K. P. MacCabe, and J. A. O’Sullivan, “Coded apertures for x-ray scatter imaging,” *Applied Optics*, vol. 52, pp. 7745–7754, Nov 2013.
 - [34] J. A. Greenberg, K. Krishnamurthy, M. Lakshmanan, K. MacCabe, S. Wolter, A. Kapadia, and D. Brady, “Coding and sampling for compressive x-ray diffraction tomography,” in *SPIE Optical Engineering + Applications*, p. 885813, International Society for Optics and Photonics, 2013.
 - [35] J. A. Greenberg, K. Krishnamurthy, and D. Brady, “Snapshot molecular imaging using coded energy-sensitive detection,” *Optics Express*, vol. 21, no. 21, pp. 25480–25491, 2013.
 - [36] U. Van Stevendaal, J. P. Schlomka, A. Harding, and M. Grass, “A reconstruction algorithm for coherent scatter computed tomography based on filtered back-projection,” *Medical Physics*, vol. 30, p. 2465, 2003.
 - [37] J. Hubbell, “Review and history of photon cross section calculations,” *Physics in Medicine and Biology*, vol. 51, no. 13, p. R245, 2006.
 - [38] M. J. Berger, J. H. Hubbell, S. M. Seltzer, J. Chang, J. S. Coursey, R. Sukumar, D. S. Zucker, and K. Olsen, “Xcom: Photon cross sections database,” 1990, 1998.
 - [39] D. Marks. personal communication, 2011.
 - [40] J. D. Jackson, *Classical electrodynamics*. Wiley-VCH, 3rd ed., 1998.
 - [41] M. T. E. Golay, “Multi-slit spectrometry,” *Journal of the Optical Society of America*, vol. 39, no. 6, p. 437, 1949.

- [42] M. Harwit and N. J. Sloane, *Hadamard transform optics*, vol. 1. 1979.
- [43] A. Veeraraghavan, R. Raskar, A. Agrawal, A. Mohan, and J. Tumblin, “Dappled photography: Mask enhanced cameras for heterodyned light fields and coded aperture refocusing,” *ACM Transactions on Graphics*, vol. 26, no. 3, p. 69, 2007.
- [44] P. Potuluri, M. Xu, and D. Brady, “Imaging with random 3d reference structures,” *Optics Express*, vol. 11, no. 18, pp. 2134–2141, 2003.
- [45] P. Potuluri, U. Gopinathan, J. Adleman, and D. Brady, “Lensless sensor system using a reference structure,” *Optics Express*, vol. 11, no. 8, pp. 965–974, 2003.
- [46] M. E. Gehm, R. John, D. J. Brady, R. M. Willett, T. J. Schulz, *et al.*, “Single-shot compressive spectral imaging with a dual-disperser architecture,” *Optics Express*, vol. 15, no. 21, pp. 14013–14027, 2007.
- [47] A. Wagadarikar, R. John, R. Willett, and D. J. Brady, “Single disperser design for coded aperture snapshot spectral imaging,” *Applied Optics*, vol. 47, no. 10, pp. B44–B51, 2008.
- [48] K. Choi and D. J. Brady, “Coded aperture computed tomography,” in *SPIE Optical Engineering+ Applications*, p. 74680B, International Society for Optics and Photonics, 2009.
- [49] A. Mrozack, D. L. Marks, and D. J. Brady, “Coded aperture spectroscopy with denoising through sparsity,” *Optics Express*, vol. 20, no. 3, pp. 2297–2309, 2012.
- [50] L. Mertz and N. O. Young, “Fresnel transformation of images (fresnel coding and decoding of images),” in *Optical Instruments and Techniques* (K. J. Habell, ed.), p. 305, 1962.
- [51] H. H. Barrett and F. A. Horrigan, “Fresnel zone plate imaging of gamma rays; theory,” *Applied Optics*, vol. 12, pp. 2686–2702, Nov 1973.
- [52] J. G. Ables, “Fourier transform photography: a new method for x-ray astronomy,” in *Proceedings of the Astronomical Society of Australia*, vol. 1, p. 172, 1968.
- [53] R. H. Dicke, “Scatter-hole cameras for x-rays and gamma rays,” *The Astrophysical Journal*, vol. 153, p. L101, 1968.
- [54] M. J. E. Golay, “Point arrays having compact, nonredundant autocorrelations,” *Journal of the Optical Society of America*, vol. 61, pp. 272–273, Feb 1971.
- [55] E. E. Fenimore and T. M. Cannon, “Coded aperture imaging with uniformly redundant arrays,” *Applied Optics*, vol. 17, pp. 337–347, Feb 1978.
- [56] S. R. Gottesman and E. E. Fenimore, “New family of binary arrays for coded aperture imaging,” *Applied Optics*, vol. 28, pp. 4344–4352, Oct 1989.

- [57] E. Candes, J. Romberg, and T. Tao, “Robust uncertainty principles: exact signal reconstruction from highly incomplete frequency information,” *Information Theory, IEEE Transactions on*, vol. 52, pp. 489–509, Feb 2006.
- [58] D. Donoho, “Compressed sensing,” *Information Theory, IEEE Transactions on*, vol. 52, pp. 1289–1306, April 2006.
- [59] W. H. Richardson, “Bayesian-based iterative method of image restoration,” *Journal of the Optical Society of America*, vol. 62, no. 1, pp. 55–59, 1972.
- [60] L. Lucy, “An iterative technique for the rectification of observed distributions,” *The astronomical journal*, vol. 79, p. 745, 1974.
- [61] J. A. O’Sullivan and J. Benac, “Alternating minimization algorithms for transmission tomography,” *Medical Imaging, IEEE Transactions on*, vol. 26, no. 3, pp. 283–297, 2007.
- [62] B. R. Frieden, “Band-unlimited reconstruction of optical objects and spectra,” *Journal of the Optical Society of America*, vol. 57, no. 8, pp. 1013–1019, 1967.
- [63] S. W. Golomb and G. Gong, *Signal design for good correlation: for wireless communication, cryptography, and radar*. Cambridge University Press, 2005.
- [64] M. Bertero and P. Boccacci, *Introduction to inverse problems in imaging*. CRC press, 1998.
- [65] R. Cernik, K. Khor, and C. Hansson, “X-ray colour imaging,” *Journal of The Royal Society Interface*, vol. 5, no. 21, pp. 477–481, 2008.
- [66] G. Harding and B. Schreiber, “Coherent x-ray scatter imaging and its applications in biomedical science and industry,” *Radiation physics and chemistry*, vol. 56, no. 1, pp. 229–245, 1999.
- [67] C. Crespy, P. Duvauchelle, V. Kaftandjian, F. Soulez, and P. Ponard, “Energy dispersive x-ray diffraction to identify explosive substances: Spectra analysis procedure optimization,” *Nuclear Instruments and Methods in Physics Research Section A: Accelerators, Spectrometers, Detectors and Associated Equipment*, vol. 623, no. 3, pp. 1050–1060, 2010.
- [68] G. Harding, M. Newton, and J. Kosanetzky, “Energy-dispersive x-ray diffraction tomography,” *Physics in Medicine and Biology*, vol. 35, no. 1, p. 33, 1990.
- [69] C. Hall, P. Barnes, J. Cockcroft, S. Colston, D. Hausermann, S. Jacques, A. Jupe, and M. Kunz, “Synchrotron energy-dispersive x-ray diffraction tomography,” *Nuclear Instruments and Methods in Physics Research Section B: Beam Interactions with Materials and Atoms*, vol. 140, no. 1-2, pp. 253–257, 1998.
- [70] A. Chawla and E. Samei, “Geometrical repeatability and motion blur analysis of a

- new multi-projection x-ray imaging system,” in *Nuclear Science Symposium Conference Record, 2006. IEEE*, vol. 5, pp. 3170–3173, Oct 2006.
- [71] A. Chawla, S. Boyce, L. Washington, H. McAdams, and E. Samei, “Design and development of a new multi-projection x-ray system for chest imaging,” *Nuclear Science, IEEE Transactions on*, vol. 56, pp. 36–45, Feb 2009.
- [72] S. Beath and I. Cunningham, “Pseudomonoeenergetic x-ray diffraction measurements using balanced filters for coherent-scatter computed tomography,” *Medical Physics*, vol. 36, p. 1839, 2009.
- [73] C. Dodge and M. Flynn, “Su-cc-vala-05: Advanced integral method for the simulation of diagnostic x-ray spectra,” *Medical Physics*, vol. 33, no. 6, p. 1983, 2006.
- [74] E. D. Kolaczyk and R. D. Nowak, “Multiscale likelihood analysis and complexity penalized estimation,” *Annals of Statistics*, pp. 500–527, 2004.
- [75] K. Lange and R. Carson, “Em reconstruction algorithms for emission and transmission tomography,” *J. Comput. Assist. Tomogr*, vol. 8, no. 2, pp. 306–316, 1984.
- [76] D. J. Crotty, R. L. McKinley, and M. P. Tornai, “Experimental spectral measurements of heavy k-edge filtered beams for x-ray computed mamotomography,” *Physics in Medicine and Biology*, vol. 52, no. 3, pp. 603–616, 2007.
- [77] Y. Kaganovsky, D. Li, A. D. Holmgren, H. Jeon, K. P. MacCabe, J. A. Politte, D G O’Sullivan, L. Carin, and B. D. J, “Compressed sampling strategies for tomography,” *Submitted to Journal of the Optical Society of America*, 2014.
- [78] G. G. Poludniowski and P. M. Evans, “Calculation of x-ray spectra emerging from an x-ray tube. part i. electron penetration characteristics in x-ray targets,” *Medical Physics*, vol. 34, no. 6, pp. 2164–2174, 2007.
- [79] G. G. Poludniowski, “Calculation of x-ray spectra emerging from an x-ray tube. part ii. x-ray production and filtration in x-ray targets,” *Medical Physics*, vol. 34, no. 6, pp. 2175–2186, 2007.
- [80] G. Poludniowski, G. Landry, F. DeBlois, P. M. Evans, and F. Verhaegen, “Spekcalc : a program to calculate photon spectra from tungsten anode x-ray tubes,” *Physics in Medicine and Biology*, vol. 54, no. 19, p. N433, 2009.
- [81] J. Amanatides, A. Woo, *et al.*, “A fast voxel traversal algorithm for ray tracing,” in *Proceedings of Eurographics*, vol. 87, pp. 3–10, 1987.
- [82] D. Slepian, “Prolate spheroidal wave functions, fourier analysis, and uncertainty-i,” *Bell System Technical Journal*, vol. 40, pp. 43–64, 1961.